

DTIC FILE COPY

4

AFGL-TR-88-0058

P136

AD-A196 495

MICROWAVE MOISTURE SOUNDER FEASIBILITY STUDY
PHASE II: RETRIEVAL OPTIMIZATION

R. G. ISAACS
G. DEBLONDE
Y.-Q. JIN
R. D. WORSHAM
C. GRASSOTTI
A. M. VOGELMANN
B. L. LINDNER

Atmospheric and Environmental Research Inc. (AER)
840 Memorial Drive
Cambridge, Massachusetts 02139

Final Report
12 August 1985-14 February 1988

14 March 1988

APPROVED FOR PUBLIC RELEASE;
DISTRIBUTION UNLIMITED

Air Force Geophysics Laboratory
Air Force Systems Command
United States Air Force
Hanscom AFB, Massachusetts 01731

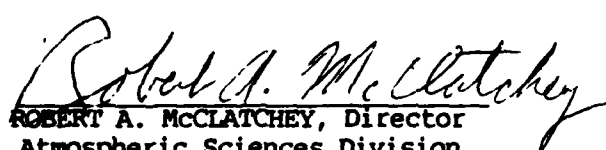
DTIC
ELECTE
S JUL 27 1988 D
H

"This technical report has been reviewed and is approved for publication"


VINCENT J. FALCONE, JR.
Contract Manager


KENNETH R. HARDY, Chief
Satellite Meteorology Branch

FOR THE COMMANDER


ROBERT A. McCLATCHEY, Director
Atmospheric Sciences Division

This report has been reviewed by the ESD Public Affairs Office (PA) and is releasable to the National Technical Information Service (NTIS).

Qualified requestors may obtain additional copies from the Defense Technical Information Center. All others should apply to the National Technical Information Service.

If your address has changed, or if you wish to be removed from the mailing list, or if the addressee is no longer employed by your organization, please notify AFGL/DAA, Hanscom AFB, MA 01731. This will assist us in maintaining a current mailing list.

Do not return copies of this report unless contractual obligations or notices on a specific document requires that it be returned.

Unclassified

SECURITY CLASSIFICATION OF THIS PAGE

REPORT DOCUMENTATION PAGE

| | | | |
|--|---|---|---------------------------------|
| 1a REPORT SECURITY CLASSIFICATION Unclassified | | 1b RESTRICTIVE MARKINGS | |
| 2a SECURITY CLASSIFICATION AUTHORITY | | 3 DISTRIBUTION/AVAILABILITY OF REPORT Approved for public release; Distribution unlimited | |
| 2b DECLASSIFICATION/DOWNGRADING SCHEDULE | | | |
| 4 PERFORMING ORGANIZATION REPORT NUMBER(S) Final | | 5 MONITORING ORGANIZATION REPORT NUMBER(S) AFGL-TR-88-0058 | |
| 6a NAME OF PERFORMING ORGANIZATION Atmospheric and Environmental Research, Inc. | 6b OFFICE SYMBOL (If applicable) | 7a NAME OF MONITORING ORGANIZATION Air Force Geophysics Laboratory | |
| 6c ADDRESS (City, State, and ZIP Code) 14 Memorial Drive Bedford, MA 01730 | | 7b ADDRESS (City, State, and ZIP Code) Hanscom AFB, MA 01731 | |
| 8a NAME OF FUNDING/SPONSORING ORGANIZATION Air Force Geophysical Laboratory | 8b OFFICE SYMBOL (If applicable) AFGL/LYS | 9 PROCUREMENT INSTRUMENT IDENTIFICATION NUMBER F19628-84-C-0134 | |
| 8c ADDRESS (City, State, and ZIP Code) Hanscom AFB, MA 01731-5000 | | 10. SOURCE OF FUNDING NUMBERS | |
| | | PROGRAM ELEMENT NO 62101F | PROJECT NO. 6670 |
| | | TASK NO 17 | WORK UNIT ACCESSION NO AK |
| 11 TITLE (Include Security Classification) Microwave Moisture Sounder Feasibility Study Phase II: Retrieval Optimization | | | |
| 12 PERSONAL AUTHOR(S) R. G. Isaacs, G. Deblonde, Y. Q. Jin, R. D. Worsham, C. Grassetti, A. M. Vogelmann, B. L. Lindner | | | |
| 13a. TYPE OF REPORT Final Report | 13b. TIME COVERED FROM 8/12/85 TO 2/14/88 | 14 DATE OF REPORT (Year, Month, Day) 1988 March 14 | 15 PAGE COUNT 130 |
| 16. SUPPLEMENTARY NOTATION | | | |
| 17 COSATI CODES | | 18 SUBJECT TERMS (Continue on reverse if necessary and identify by block number) | |
| FIELD | GROUP | Retrieval Temperature Multiple Scattering Water Vapor DMSP | |
| | | | |
| | | | |
| 19 ABSTRACT (Continue on reverse if necessary and identify by block number) <p>This report documents the results of our two-year Phase II effort to investigate the application of data from the proposed DMSP microwave moisture sounder (SSM/T-2) to the inference of water vapor profiles, temperature profiles, cloud, precipitation, and the properties of the underlying surface. The goal of this research is to provide a unified retrieval scheme capable of processing microwave and millimeter wave sensor (i.e., sounder and imager) data which extends the adopted operational algorithm based on a purely statistically based retrieval of temperature profiles from the SSM/T-1, moisture profiles from the SSM/T-2, and surface and atmospheric parameters such as precipitation and integrated cloud liquid water from the SSM/I. The approach uses two concepts to increase retrieval accuracy. First, physical considerations based on the application of the radiative transfer equation are used to quality control the statistically derived first guess retrievals. Second, data sources from colocated microwave mission sensors (i.e., the SSM/T-1, SSM/T-2, and SSM/I) are combined when necessary to more completely</p> | | | |
| 20. DISTRIBUTION/AVAILABILITY OF ABSTRACT <input type="checkbox"/> UNCLASSIFIED/UNLIMITED <input type="checkbox"/> SAME AS RPT <input type="checkbox"/> DTIC USERS | | 21 ABSTRACT SECURITY CLASSIFICATION Unclassified | |
| 22a NAME OF RESPONSIBLE INDIVIDUAL Vincent Falcone | | 22b TELEPHONE (Include Area Code) (617) 377-4029 | 22c OFFICE SYMBOL AFGL/LYS |

Cont of Block 19:

characterize the spectral dependence of the observed brightness temperatures on the meteorological properties of the surface and atmosphere. By combining data from all available sensors, the desired meteorological parameters can be more accurately determined. Based on our evaluation of cloud effects on millimeter wave brightness temperatures and water vapor retrievals (Isaacs and Deblonde, 1987), we have suggested use of the visible and infrared Operational Linescan System (OLS) to provide information on cloud presence. The unified retrieval scheme has been summarized in the paper by Isaacs (1988).



| | |
|--------------------|--|
| Accession For | |
| NTIS GRA&I | <input checked="checked" type="checkbox"/> |
| DTIC TAB | <input type="checkbox"/> |
| Unannounced | <input type="checkbox"/> |
| Justification | |
| By | |
| Distribution/ | |
| Availability Codes | |
| Avail and/or | |
| Dist | Special |
| A-1 | |

TABLE OF CONTENTS

| | Page |
|--|------|
| 1. Introduction..... | 1 |
| 1.1 Background | 1 |
| 1.2 Study Objectives | 4 |
| 1.3 Overview of Report | 5 |
| 2. Task 1 - Clear Sky, Multiple Instrument Retrieval Algorithm Development | 6 |
| 2.1 Overview | 6 |
| 2.2 Statistical Retrieval Results | 10 |
| 2.3 Theoretical Basis of Physical Retrieval Approach | 12 |
| 2.4 Results for Retrieval of Temperature and Integrated Water Vapor Using SSM/T-1 and SSM/T-2 | 22 |
| 2.4.1 Statistical Estimate as First Guess | 23 |
| 2.4.1.1 Selective Channels for the SSM/T-1 | 23 |
| 2.4.1.2 All Channels for SSM/T-1 | 24 |
| 2.4.2 Mean Values of First Set as First Guess | 32 |
| 2.4.3 Results Summary | 35 |
| 2.5 The Effect of Clouds on Millimeter Wave Moisture Retrievals | 37 |
| 2.5.1 Cloudy Moisture Sounder Channel Weighting Functions ... | 38 |
| 2.5.2 Brightness Temperature Simulations | 40 |
| 2.5.3 Water Vapor Profile Retrievals in the Presence of Clouds | 45 |
| 2.6 A Unified Retrieval Methodology for the DMSP Meteorology Sensors | 52 |
| 2.6.1 Proposal Scheme | 52 |
| 2.6.2 Processing of OLS Imagery Data for Cloud Property Retrieval | 54 |
| 3. Task 2 - Simulation Model Enhancements | 55 |
| 3.1 Multiple Scattering | 55 |
| 3.2 Mie Scattering | 57 |
| 3.2.1 Precipitation Scattering Property Parameterization | 58 |
| 3.2.2 Exact Mie Scattering Algorithm | 61 |
| 3.3 Thermal Radiative Transfer for Polarized Inhomogeneous Nonisothermal Atmospheric Precipitation and Statistical Retrieval of Related Parameters | 66 |
| 3.3.1 Introduction | 66 |
| 3.3.2 Thermal Radiative Transfer Theory | 69 |
| 3.3.3 Statistical Retrieval of Geophysical Parameters | 72 |
| 3.4 Surface Modeling | 75 |
| 3.4.1 Surface Modeling Approaches | 76 |
| 3.4.2 Application of Wave Theory Models for Discrete Scatterers | 78 |
| 3.4.3 Application of Radiative Transfer Theory Models for Continuous Random Media | 80 |

TABLE OF CONTENTS
(cont.)

| | <u>Page</u> |
|---|-------------|
| 3.4 Surface Models (continued) | |
| 3.4.4 Comparison with SMMR Data | 87 |
| 3.4.4.1 Data Sample | 87 |
| 3.4.4.2 Results of Data Comparison | 88 |
| 3.4.5 Summary and Conclusions | 89 |
| 4. SSM/I Footprint Characterization Using Other DMSP Sensors | 98 |
| 4.1 Background | 98 |
| 4.2 Imagery Analysis of Microwave, Visible, and Infrared Data | 100 |
| 4.3 Modeling Nonuniform Fields-of-View | 105 |
| 5. Conclusions and Recommendations | 107 |
| 5.1 Summary and Conclusions | 107 |
| 5.2 Discussion of Future Work | 110 |
| 6. Acknowledgements | 111 |
| 7. References | 111 |
| Appendix A - Papers Presented Based on Work Completed During This Effort | A-1 |
| Appendix B - Publications Resulting from Work Completed During This Effort | B-1 |

LIST OF FIGURES

| <u>Figure</u> | | <u>Page</u> |
|---------------|--|-------------|
| 2-1 | Temperature (a) and water vapor profile (b). RMS errors using statistical retrieval for midlatitude winter atmospheres. | 13 |
| 2-2 | Temperature (a) and water vapor profile (b). RMS errors Using statistical retrieval for tropical atmospheres. | 13 |
| 2-3 | Unified retrieval algorithm for microwave mission sensor data. | 16 |
| 2-4 | Physical retrieval results for the tropical cases. | 36 |
| 2-5 | Physical retrieval results for midlatitude cases. | 37 |
| 2-6. | SSM/T-2 weighting functions for U.S. standard profile: (a) clear, (b) cloudy. | 41 |
| 2-7 | SSM/T-2 weighting functions for tropical profile: (a) clear, (b) cloudy. | 41 |
| 2-8 | SSM/T-2 weighting functions for midlatitude summer profile:(a) clear, (b) cloudy. | 42 |
| 2-9 | SSM/T-2 weighting functions for midlatitude winter profile: (a) clear, (b) cloudy. | 42 |
| 2-10 | SSM/T-2 weighting functions for subarctic summer profile: (a) clear, (b) cloudy. | 43 |
| 2-11 | SSM/T-2 weighting functions for subarctic winter profile: (a) clear, (b) cloudy. | 43 |
| 2-12 | Brightness temperature (K) versus integrated liquid water content (g/cm^{-2}) over: (a) ocean and (b) land for status cloud. | 47 |
| 2-13 | Brightness temperature (K) versus integrated liquid water content (g/cm^{-2}) over: (a) ocean and (b) land for cumulus cloud. | 47 |
| 2-14 | Brightness temperature (K) versus integrated liquid water content (g/cm^{-2}) over: (a) ocean and (b) land for altostratus cloud. | 48 |
| 2-15 | Brightness temperature (K) versus integrated liquid water content (g/cm^{-2}) over: (a) ocean and (b) land for stratocumulus cloud. | 48 |

LIST OF FIGURES (continued)

| <u>Figure</u> | | <u>Page</u> |
|---------------|--|-------------|
| 2-16 | Brightness temperature (K) versus integrated liquid water content (g/cm^{-2}) over: (a) ocean and (b) land for nimbostratus cloud. | 49 |
| 2-17 | Water vapor retrieval RMS fractional errors for tropical, oceanic soundings with clear atmospheres (solid), cloudy atmospheres (dashed), and climatology (short dashes). | 51 |
| 2-18 | Water vapor retrieval RMS fractional errors for land soundings with clear atmospheres (solid), cloudy atmospheres (dashed), and climatology (short dashes). | 51 |
| 2-19 | Schematic of unified DMSP retrieval scheme. | 52 |
| 2-20 | Spatial coherence results for partially cloudy microwave field-of-view using: (a) visible and (b) infrared GOES imager data. | 55 |
| 3-1 | Comparison of extinction coefficient (BEXT) and single scattering albedo (OMEGA0) calculated by the subroutine (lines) and exact Mie theory calculations (symbols) throughout the millimeter wave region from 89.5 to 183 GHz at two values of the rainfall rate (2 and 5 mmhr^{-1}). | 62 |
| 3-2 | Comparison of the first eight Legendre polynomial coefficients (N) of a Marshall-Palmer size distribution of rain drops with a rainfall rate of 5 mmhr^{-1} calculated by the subroutine (lines) and exact Mie theory calculations from 89.5 to 183 GHz. | 62 |
| 3-3 | Comparison between exact (lines) and approximate (symbols) brightness temperature calculations as a function of viewing angle (THETA) for a 3 km rain layer with rainfall rate of 15 mmhr^{-1} at (a) 19.35 GHz and (b) 37.0 GHz. | 63 |
| 3-4 | The geometry of the theoretical modeling. | 73 |
| 3-5 | Brightness temperature vs. rain rates. | 74 |
| 3-6 | Retrieval of rain rates. | 74 |
| 3-7 | Retrieval of emissivities. | 75 |
| 3-8 | Frequency dependence of ocean surface emissivity for calm ($u < 7\text{ms}^{-1}$) and rough ($u \geq 7\text{ms}^{-1}$) ocean at a look angle of 54° | 90 |
| 3-9 | Look angle dependence of ocean surface emissivity for calm ($u < 7\text{ms}^{-1}$) and rough ($u \geq 7\text{ms}^{-1}$) ocean at a frequency of 18.0 GHz ($T_s = 273\text{K}$). | 91 |

LIST OF FIGURES (continued)

| <u>Figure</u> | | <u>Page</u> |
|---------------|---|-------------|
| 3-10 | Frequency dependence of dry and wet snowpack emissivity at a look angle of 54° ($T_s = 273.K$). | 91 |
| 3-11 | Look angle dependence of dry and wet snowpack emissivity at a frequency of 18.0 GHz ($T_s = 273.K$). | 92 |
| 3-12 | Frequency dependence of first year and multiyear sea ice emissivity at a look angle of 54° ($T_s = 273.K$). | 92 |
| 3-13 | Look angle dependence of first year and multiyear sea ice emissivity at a frequency of 18.0 GHz ($T_s = 273.K$). | 93 |
| 3-14 | Frequency dependence of dry and wet soil emissivity at a look angle of 54° | 93 |
| 3-15 | Look angle dependence of dry and wet soil emissivity at a frequency of 18.0 GHz. | 94 |
| 3-16 | Frequency dependence of surface emissivity at a look angle of 54° in the presence of vegetation with various moisture contents and layer thicknesses. | 94 |
| 3-17 | Look angle dependence of surface emissivity at a frequency of 18.0 GHz in the presence of vegetation with various moisture contents and layer thicknesses. | 95 |
| 3-18 | Brightness temperature as a function of angle for fully grown corn at a frequency of 1.4 GHz. | 95 |
| 3-19 | Brightness temperature as a function of angle for cut corn at a frequency of 1.4 GHz. | 96 |
| 3-20 | Brightness temperature as a function of angle for dry corn at a frequency of 5 GHz. | 96 |
| 3-21 | Comparison of SMMR brightness temperature data with RADTRAN model simulations for case 1 (ocean) and case 3 (heavy vegetation). | 97 |
| 3-22 | Comparison of SMMR brightness temperature data with RADTRAN model simulation for case 2 (moderate vegetation)..... | 97 |
| 4-1 | (a) High resolution Landsat visible data corresponding to the area of a single microwave FOV; (b) same area transformed to correspond to DMSP spatial and spectral resolution | 102 |
| 4-2 | Spatial Coherence Approach for Characterizing Field-of-View Uniformity: (a) uniform FOV, (b) FOV with a few distinct regions. | 104 |

LIST OF TABLES

| <u>Table</u> | | <u>Page</u> |
|--------------|--|-------------|
| 1-1 | Microwave Moisture Sounder Feasibility Study: Phase I Accomplishments and Proposed Phase II Objectives | 3 |
| 2-1 | Defense Meteorological Satellite Program (DMSP) Sensors | 11 |
| 2-2 | Fraction of Unexplained Variance for Statistical Retrievals: Midlatitude Summer Atmosphere | 14 |
| 2-3 | Fraction of Unexplained Variance for Statistical Retrievals: Tropical Summer Atmospheres | 15 |
| 2-4 | Ratios of Mean Integrated Water Vapor | 24 |
| 2-5 | Simultaneous Retrieval Results Using Statistical First Guess and Selective Channels | 25 |
| 2-6 | Simultaneous Retrieval Results for Tropical Data Set: (a) Noise, (b) No Noise | 26 |
| 2-7 | Simultaneous Retrieval Results for Midlatitude Data Set: (a) Noise, (b) No Noise | 27 |
| 2-8 | Results for New Convergence Criteria, Tropical Atmospheres: (a) Noise, (b) No Noise | 29 |
| 2-9 | Results for New Convergence Criteria, Midlatitude Atmospheres: (a) Noise, (b) No Noise | 31 |
| 2-10 | Retrieval Results Using Mean as a First Guess (Single Convergence Criteria Only) | 33 |
| 2-11 | Retrieval Results Using Selective Criteria for Convergence: (a) Noise, (b) No Noise | 34 |
| 2-12 | Cloud Type, Liquid Water Contents, and Vertical Extents Used in Cloudy Brightness Temperature Simulations | 39 |
| 3-1 | Comparison of Eigenvalues From Liou's Root Search Method for the Discrete Ordinate Method of those from the EISPACK Routines | 57 |
| 3-2 | File Structure Relating RAD1 and RAD2 Programs | 64 |
| 3-3 | RAD1IN Input File and Format | 65 |
| 3-4 | RAD2IN Input File and Format | 66 |

LIST OF TABLES (continued)

| <u>Table</u> | | <u>Page</u> |
|--------------|--|-------------|
| 3-5 | Sample Output Files from the RAD2 Code for a Marshall-Palmer Rain Distribution at 5 mm/h for 89.5 (top) and 183 (bottom) GHz | 67 |
| 3-6 | Surface Model Types and Modeling Approaches | 77 |

1. INTRODUCTION

1.1 Background

This report documents the results of our two-year Phase II effort to investigate the application of data from the proposed DMSP microwave moisture sounder (SSM/T-2) to the inference of water vapor profiles, temperature profiles, cloud, precipitation, and the properties of the underlying surface. Although originally conceived as an enhancement to the SSM/T temperature sounder to provide the capability to obtain water vapor profiles alone utilizing the water vapor resonance feature in the vicinity of 183 GHz, the SSM/T-2 sensor channel set is also sensitive to surface emission and clouds and precipitation within the field-of-view. This is due to the inclusion of "window" channels at 91.66 and 150.0 GHz in addition to channels near 183 GHz when the water vapor abundance is small enough to permit the sensor to see into middle and lower troposphere.

The goal of this research is to provide a unified retrieval scheme capable of processing microwave and millimeter wave sensor (i.e., sounder and imager) data which extends the adopted operational algorithm based on a purely statistically based retrieval of temperature profiles from the SSM/T-1, moisture profiles from the SSM/T-2, and surface and atmospheric parameters such as precipitation and integrated cloud liquid water from the SSM/I. The approach uses two concepts to increase retrieval accuracy. First, physical considerations based on the application of the radiative transfer equation are used to quality control the statistically derived first guess retrievals. Here the key question is, how consistent are the statistically retrieved profiles of temperature and moisture with the observed brightness temperatures? Second, data sources from colocated microwave mission sensors (i.e., the SSM/T-1, SSM/T-2, and SSM/I) are combined when necessary to more completely characterize the spectral dependence of the observed brightness temperatures on the meteorological properties of the surface and atmosphere. By combining data from all available sensors, the desired meteorological parameters can be more accurately determined. Based on our evaluation of cloud effects on millimeter wave brightness temperatures and water vapor retrievals (Isaacs and Deblonde, 1987), we have suggested use of the visible and infrared Operational Linescan System (OLS) to provide information on cloud presence. The unified retrieval scheme has been summarized in the paper by Isaacs (1988).

In the initial Phase I effort of this program (Isaacs et al, 1985a), simulation models were developed to treat the instrumental response of a sounder operating in the vicinity of 183 GHz to representative variations of cloud and precipitation realistically encountered in the atmosphere. The Phase I technical objectives are summarized in Table 1-1. The simulation model developed used the gaseous absorption algorithm and model atmospheres from RADTRAN (Falcone et al., 1982) as well as the cloud models from the AFGL AEROSOL subroutine (Falcone et al., 1979). In the presence of precipitation, a multiple scattering calculation is required. The discrete ordinate method (DOM) (Liou, 1973) was chosen to evaluate the equation of radiative transfer. The version of the DOM chosen for implementation (Liou et al., 1980) had never been successfully run at AFGL and required ancillary millimeter wave multiple scattering data for the precipitation drop size distribution which was not internally available. The code was successfully debugged and run on the AFGL Cyber and a parameterization was developed for evaluating the required scattering properties as a function of frequency, temperature, drop size distribution, rain rate, and phase (i.e., ice or water) without the necessity for on-line Mie theory calculations. The model is described in the Phase I interim report (Isaacs et al., 1985a).

As the result of limited instrument and sensitivity tests performed with this simulation model on candidate systems, the potential degradation of moisture retrievals due to the presence of clouds and precipitation was demonstrated. Retrievals were performed using a statistical approach based on the "D" matrix formalism (Gaut et al, 1975) which is conceptually quite similar to the adopted operational retrieval scheme. Additionally, the dependence of water vapor profile retrieval accuracy on the nature of the underlying surface was evaluated. For example, retrievals over the ocean (assuming calm seas) were more accurate than those over land.

In order to improve moisture retrievals in the presence of clouds and additionally exploit the demonstrated sensitivity of the SSM/T-2 instrument to obtain cloud and precipitation properties when present, it was suggested that a retrieval scheme should be sought which explicitly treats these factors. Furthermore it was suggested that the optimal retrieval approach should be implemented utilizing all available DMSP sensor data. Brightness temperature

Table 1-1. Microwave Moisture Sounder Feasibility Study: Phase I Accomplishments and Proposed Phase II Objectives

| PHASE I (ACCOMPLISHMENTS) | | PHASE II (TO BE ACCOMPLISHED) | |
|---|--|---|--|
| TECHNICAL OBJECTIVE | FEASIBILITY DEMONSTRATED | PROBLEM IDENTIFIED | TECHNICAL OBJECTIVE |
| <ul style="list-style-type: none"> Develop simulation models applicable to the design specification of a 183 GHz microwave moisture sounder | <ul style="list-style-type: none"> Algorithm for gaseous absorption converted and tested | <ul style="list-style-type: none"> Existing (DOM) algorithm time consuming, inefficient and inaccurate | <ul style="list-style-type: none"> Implement matrix eigensystem solution methods in order to improve accuracy and efficiency of multiple scattering submodel |
| | <ul style="list-style-type: none"> Converted and successfully debugged discrete ordinate method (DOM) for multiple scattering by precipitation | | |
| | <ul style="list-style-type: none"> Evaluated cloud/rain optical properties of desired frequencies | <ul style="list-style-type: none"> Existing DOM requires ancillary scattering parameters | <ul style="list-style-type: none"> Provide necessary programs to calculate exact optical parameters required by the multiple scattering code via Mie theory for arbitrary distributions of liquid or glaciated hydrometeors and interface routines to obtain efficient parameterizations from those results |
| | <ul style="list-style-type: none"> Developed scattering property parameterization for DOM | | |
| | <ul style="list-style-type: none"> Converted DOM for pseudo-polarized calculation | <ul style="list-style-type: none"> Existing DOM does not treat polarized case | <ul style="list-style-type: none"> Implement complete polarized multiple scattering model (i.e. vectorized radiative transfer equation) |
| | <ul style="list-style-type: none"> Converted DOM for arbitrary look angle | | <ul style="list-style-type: none"> Implement terrain and snow scattering model of surface emission |
| <ul style="list-style-type: none"> Test and validate simulation models | <ul style="list-style-type: none"> Delivered above to AFCL Ongoing | | <ul style="list-style-type: none"> Continue simulation model testing and validation |
| <ul style="list-style-type: none"> Perform limited sensitivity tests to ascertain the effects of surface emissivity, cloud, precipitation, and other realistic variations of meteorology on sensor performance | <ul style="list-style-type: none"> Evaluated channel weighting functions and brightness temperature sensitivity over land/ocean to: <ul style="list-style-type: none"> - water vapor variations - cloud presence - rain presence - water vapor variation over low cloud over ocean | <ul style="list-style-type: none"> Brightness temperatures sensitive to emissivity, cloud, and precipitation Cloud presence in lower atmosphere over ocean decreases sensitivity to variations in water vapor above cloud | <ul style="list-style-type: none"> Investigate the alternative application of proposed SSM/T-2 microwave moisture sounder channels for retrieval of cloud and precipitation properties: (a) as part of the SSM/T package, (b) together with SSM/I data, and (c) collectively with OLS imager data and that of infrared sounders |
| <ul style="list-style-type: none"> Determine the potential adverse impact of cloud liquid water and precipitation on moisture retrievals | <ul style="list-style-type: none"> Implemented EOF/covariance matrix retrieval code Performed moisture retrievals for various channels, instrumental noise levels, land/ocean, cloud/no cloud, precipitation conditions for tropical atmospheres | <ul style="list-style-type: none"> Cloud degrades microwave moisture retrieval Rain precludes moisture retrieval | <ul style="list-style-type: none"> Develop a moisture retrieval approach applicable to the SSM/T-2 which explicitly treats cloud and precipitation based on combination of available microwave and infrared sensors |

data from the ensemble of microwave mission sensors colocated aboard the DMSP spacecraft (i.e., the SSM/T-1, SSM/T-2, and SSM/I) and as necessary, visible and/or infrared radiance data from the Operational Linescan System (OLS) should be integrated to provide a generalized geophysical parameter retrieval. This multispectral approach would enable available information on surface properties from the microwave imager to be integrated into the retrievals of temperature and moisture profiles. Additionally, information on the temperature dependence of the water vapor profiles and water vapor dependence of the temperature profiles would be included explicitly.

This approach to the retrieval problem, i.e., as a multispectral/multi-parameter system, expresses an emergent philosophy within the state-of-the-art remote sensing community (cf. Susskind et al., 1984, 1985; Smith et al., 1985).

1.2 Study Objectives

The technical objectives of the Phase II effort are given in Table 1-1. The primary objective of this research effort was to develop a modified approach to the retrieval of water vapor profiles and cloud and precipitation properties, employing an enhanced version of the millimeter wave moisture sounder simulation model developed under the Phase I effort. As described above, this approach will integrate data from the microwave mission sensors and apply physical retrieval considerations to enhance the accuracy of water vapor and temperature profile retrievals and, additionally, provide information on the state of the underlying surface. Four subtasks were identified to accomplish the retrieval development objective. These include: (a) implementation of a physical retrieval method for the 183 GHz moisture channels, (b) development of a cloud filtering algorithm for use in the physical retrieval, (c) incorporation of microwave imager data and other relevant data (such as that from the OLS), and (d) testing, tuning, and verification of the retrieval algorithm.

About nine months into the performance period covered by this report, the contract supporting this study was modified to increase the level of effort devoted to the incorporation of other data within the retrieval development (item c above). Specifically, it was desired to investigate the effects of

the variability of the microwave properties of the earth's surface and atmosphere within the relatively large footprint of the SSM/I. In analyzing the SSM/I field-of-view, the small pixel size of the visible and infrared imagery was to be employed to provide guidelines on when the SSM/I microwave imager was viewing nonuniform conditions and what the contributions of these nonuniform surfaces is to the microwave observations. The study was to include the identification of rain areas and include modelling various types of surfaces and estimating their emissivities. The analysis performed was to be supported by using Scanning Multichannel Microwave Radiometer (SMMR) data along with available visible and infrared imagery.

In order to successfully accomplish the primary objective described above, certain simulation model enhancement objectives were also identified:

- To improve the accuracy and efficiency of the multiple scattering submodel based on the DOM to treat precipitation, it was desired to replace the iterative root searching eigenvalue solution provided by Liou et al. (1980) with a matrix eigensystem approach.
- Computer models were also desired to calculate the exact optical parameters required by the multiple scattering code via Mie theory for arbitrary size distributions of glaciated or liquid hydrometeors.
- The existing DOM treated only nadir viewing sensors and did not treat polarization. A complete polarized multiple scattering model based on the vectorized radiative transfer equation was desired.
- The simulation model required surface emissivities as an input parameter. It was desired to develop physical models of surface emission for a variety of terrain surfaces including snow and sea ice.

This has been a fruitful research program with much interaction with AFGL and other interested parties. Much of the work described here has been presented at conferences (Appendix A) or published (Appendix B).

1.3 Overview of Report

This report is divided into four major sections. In Section 2 to follow, the development of a physically based retrieval approach using a statistical first guess is described. This algorithm is capable of treating brightness temperature data from a variety of instruments and retrieves simultaneously to

obtain temperature profile, water vapor profile, and surface properties. As yet, the algorithm treats clear skies only. Our work on the effect of clouds on millimeter wave retrievals is also described here including results of calculations showing the sensitivity of SSM/T-2 channel brightness temperatures to cloud integrated water amounts. Finally, we outline procedures to use OLS imager data in a unified retrieval with the microwave mission sensors. A flowchart of the procedure is provided which is a simple extension of the clear sky algorithm described which employs image processing of the OLS data.

In Section 3, the simulation model enhancements are described. These topics include the implementation of the eigensystem solution for the DOM multiple scattering code, modification of Mie scattering codes for use at AFGL which will provide scattering properties for arbitrary size distributions of hydrometeors, development of a vectorized radiative transfer model to treat the anisotropic multiple scattering of microwaves by precipitation in nonisothermal atmospheres, and the development of a modularized set of microwave surface models for use in the simulation studies.

Section 4 discusses the work to date on the characterization of the uniformity of SSM/I fields-of-view based on the analysis of high resolution visible and infrared imagery data.

2. TASK 1 - CLEAR SKY, MULTIPLE INSTRUMENT RETRIEVAL ALGORITHM DEVELOPMENT

2.1 Overview

The significance of improved capabilities to specify the global moisture field (including water vapor, cloud, and precipitation) potentially afforded by an optimally designed microwave moisture sounder cannot be underestimated. Implications for numerical weather prediction are particularly promising (Kaplan et al, 1983; Isaacs et al., 1986). Radiatively, water in its many forms is the most active constituent of the troposphere. Clouds and water vapor profoundly affect the infrared temperature retrieval problem (Chahine, 1974, 1982) and the parameterization of radiative heating (WMO, 1978). A variety of studies have shown that updating the moisture field can improve short range precipitation forecasts (Perkey, 1980; Maddox et al., 1981) and

that latent heat release associated with condensation can have large short term influence on storm development (Anthes et al., 1983). Knowledge of the moisture field is also of great importance for meeting the operational requirements for better cloud forecasts and predicting optical and millimeter-wave propagation.

An observing system to retrieve moisture consists of both the sensor hardware to obtain the data and the software algorithms to retrieve the desired profiles. Operational moisture sounders aboard polar orbiters have been infrared instruments such as the HIRS-2 component of the TIROS-N Operational Vertical Sounder (TOVS) (Smith et al., 1979) and the Defense Military Satellite Program (DMSP) SSH/2 (Barnes Engineering, 1978). These instruments have exploited the infrared rotation-vibration bands near $6.7 \mu\text{m}$ (three channels) and the pure rotational bands near $20 \mu\text{m}$ (seven channels), respectively. In general, the success in obtaining operationally useful water vapor profiles from these instruments has been limited. Goals for the TOVS retrievals using a statistical inversion method are limited to precipitable water values in three broad vertical layers at accuracies of 30% (NOAA, 1981). Investigators using retrievals based on physical approaches have fared somewhat better. For example, Reuter and Susskind (1986) show that an iterative approach can improve over the first guess based on a forecast field, particularly in the upper levels (i.e., 300-500 mb).

Microwave water vapor remote sensing in the past has focused on the use of the weak rotational line at 22.235 GHz for obtaining precipitable water. This line does not have sufficient opacity to obtain a water vapor profile. A much stronger feature available for profiling is the ($3_{13} - 2_{20}$) millimeter wave rotational feature at 183.31 GHz (Schaerer and Wilheit, 1979). A set of channels has been proposed for the 1990's NOAA-NEXT series called the Advanced Microwave Sounding Unit B package (AMSU-B) (Schultz, 1982). A similar sensor called the SSM/T-2 will enhance the SSM/T microwave temperature sounder aboard DMSP. A number of studies have investigated the simulated retrieval of moisture profiles using a hypothetical 183 GHz sensor (Schaerer and Wilheit, 1979; Rosenkranz et al, 1982; Wang et al., 1983; Kakar, 1983; Kakar and Lambrigsten, 1984). For the most part these studies have focused on retrievals in clear sky conditions. Recently, the effects of clouds on statistical retrievals of water vapor at 183 GHz have been evaluated (Isaacs et al 1985a,b). These

studies noted that the presence of cloud can seriously degrade the accuracy of the retrieved profiles. Furthermore, it was noted that surface emissivity plays a critical role, i.e., retrievals over emissive land areas are not as accurate as those obtained over the less emissive oceans.

The proposed method to retrieve water vapor from the DMSP SSM/T-2 will consist of a statistical approach based on the "D" matrix methodology to obtain water vapor abundances and relative humidity at each of the mandatory levels (A. Stogryn, personal communication). The proposed "D" matrix will be globally applicable and will treat both clear and cloudy fields-of-view. A two stage retrieval is suggested, one applying to low and moderate water vapor amounts, and another to large water vapor amounts. The primary justification for the approach is computational efficiency (i.e., the "D" matrix retrieval uses little computer time and the current operational unavailability of data to support a cloud/no cloud discrimination step within the retrieval). The approach will use both SSM/T-1 and SSM/T-2 data, but no other supporting data.

For a variety of reasons, the proposed operational approach described above could be improved. The two main criticisms are its reliance on statistical data and the neglect of other potentially available data sources. Statistical methods provide excellent retrievals of conditions near that of the mean, but biased retrievals of extreme conditions. Mean conditions are generally of less meteorological interest and certainly of less operational interest than those which are away from the mean. Furthermore, physical retrievals have been shown to outperform statistical retrievals of temperature (Halem and Susskind, 1985; Susskind and Reuter, 1985). The "D" matrix approach is an inherently linear treatment, while nonlinearities can be directly treated by physical approaches. To zeroth order, the temperature retrieval problem is linear. The water vapor problem is inherently nonlinear, and therefore, physical methods should be even more useful.

It would also seem that the use of a global, clear/cloudy "D" matrix would degrade the accuracy of the water vapor retrievals when clouds are not present. When clouds are present, this approach will not improve the retrievals. Therefore, results are suboptimal at all times. Physical approaches should be able to treat clouds explicitly as part of the inversion process. The same applies to the treatment of surface emissivity. Eventually, cloud fields from the DMSP OLS (using an appropriately spatially averaged subset of

visible and infrared imagery) and/or over the oceans cloud liquid water data from the SSM/I microwave imager should be available to aid in cloud/no cloud discrimination.

Finally, it is not clear how to quality control statistical retrievals in real time. With a global "D" matrix all water vapor retrievals must be considered to have the same accuracy. With the physical retrievals, the residuals which are evaluated as part of the retrieval process (i.e., the differences between the calculated brightness temperatures and the observed brightness temperatures) can be used to flag potentially bad retrievals (and good ones) for the user. For example, when residuals are small and confidence in the retrievals is high the retrieved profiles can be given a higher priority in data assimilation schemes such as those interfacing between input fields and numerical weather prediction models.

Based on the considerations outlined above, this study has investigated an alternative retrieval approach for the SSM/T-2 and SSM/T-1 which both employs physical considerations and allows for the incorporation of other data sources such as that from the SSM/I. The approach builds on the proposed statistical retrieval scheme by using "D" matrix retrievals as first guess profiles (Section 2.2). However, brightness temperatures are then evaluated to examine the consistency of the first guesses with the observations. When the residuals are small, the process terminates. However, when residuals are larger than a preset tolerance, the procedure goes on to adjust the first guess profiles using the procedure described in Section 2.3. Results for clear sky situations are presented in Section 2.4. Our simulations suggest that cloud (and precipitation) will have an effect on millimeter wave brightness temperatures (Section 2.5). A simple way of using the code in partly cloudy cases would be to calculate equivalent clear column brightness temperatures from the observed data set using visible or infrared data to identify the cloud coverage fraction. This could be used as a first guess to work the cloud problem as an integral part of the retrieval process. This approach has been formulated and an overall unified retrieval incorporating all data sources is proposed in Section 2.6.

2.2 Statistical Retrieval Results

As a first step we have investigated application of statistical retrievals. In our earlier work we showed application of this approach (see Section 2.5.3 for a description) to the retrieval of water vapor profiles using simulated SSM/T-2 data alone (Isaacs and Deblonde, 1985b). Here we apply the technique to a unified retrieval using all the microwave mission sensors.

This section illustrates the application of the statistical retrieval approach to assessment of the accuracy of temperature profile (T), integrated water vapor profile (U), surface temperature (SURF T), and emissivity (EMISS) retrieval using data simulated for the DMSP millimeter/microwave sensor suite. In this example individual sensor characteristics such as noise and number and location of channels are kept fixed and the specific choice of instruments included in the retrieval is varied. The sensor payload of the Defense Meteorological Satellite Program (DMSP) spacecraft of the 1990's will consist of a visible/infrared imager (the operational linescan system or OLS), a microwave temperature sounder (SSM/T-1), a millimeter wave water vapor sounder (SSM/T-2), and a microwave imager (SSM/I). The current OLS imager provides high spatial resolution, global cloud imagery. Notably, all the other sensors are millimeter/microwave instruments. Of these microwave mission sensors, the SSM/T-1 and SSM/I are currently operational (Falcone and Isaacs, 1987). The SSM/T-2 is scheduled for launch in the early 1990s. Instrumental characteristics for these sensors including the noise equivalent brightness temperatures used in the data simulations are given in Table 2-1. The use of one of these instruments, combinations of two of them, or the use of data from all three were examined as possible approaches to obtain the most accurate results. Data was simulated for these sensors based on the RADTRAN (Falcone et al., 1982) computer algorithm and using ensembles of midlatitude and tropical atmospheres from a radiosonde data set consisting of a total of 400 soundings. Emissivity values were calculated from an ocean surface reflectance model assuming calm seas. The resultant values were varied

Table 2-1. Defense Meteorological Satellite Program (DMSP) Sensors

| Instrument | Frequency or Wavelength | Polarization (H or V) | FOV (km) | Response | NEΔT (k) |
|------------|-------------------------------|--------------------------|-------------|----------------------|-------------|
| SSM/T | 50.5 GHz | H | 200 | surface | 0.6 |
| | 53.2 | H | 200 | T at 2 km | 0.4 |
| | 54.35 | H | 200 | T at 6 km | 0.4 |
| | 54.9 | H | 200 | T at 10 km | 0.4 |
| | 58.825 | V | 200 | T at 16 km | 0.4 |
| | 59.4 | V | 200 | T at 22 km | 0.4 |
| | 58.4 | V | 200 | T at 30 km | 0.5 |
| SSM/I | 19.35 | H and V | 50 | surface | 0.6 |
| | 22.235 | V | 50 | water vapor | 0.6 |
| | 37.0 | H and V | 25 | clouds, rain | 0.8 |
| | 85.5 | H and V | 12.5 | clouds, snow | 1.1 |
| SSM/T-2 | 90.0 | V | 100 | surface, water vapor | 0.6 |
| | 150.0 | V | 60 | surface, water vapor | 0.6 |
| | 183.31±1 | V | 50 | water vapor | 0.8 |
| | 183.31±3 | V | 50 | water vapor | 0.6 |
| | 183.31±7 | V | 50 | water vapor | 0.6 |
| OLS | 0.4-1.1μm | | 0.6 | surface/clouds | - |
| | 10.5-12.5μm | | 2.4 | surface/clouds | - |

assuming a Gaussian distribution with the calculated value as mean and an assumed standard deviation. While surface emissivity per se is not a required geophysical parameter, it is emissivity which provides information on surface winds and sea ice over the ocean, and vegetation, soil moisture, and snow cover over the land. The surface temperature was taken as the same as the 1000 mb atmospheric temperature. The simulations assumed cloud free conditions over the ocean.

The retrieval results for various instrument combinations are shown in Tables 2-2 and 2-3, for midlatitude and tropical cases, respectively. Tabulated are fraction of unexplained variance (FUV) values for each instrument combination. Perfect retrievals have an FUV of 0.0 while those which perform no better than climatology have FUVs of 1.0. (FUVs greater than 1.0 mean that climatology is better than the retrieval.) The FUV for each parameter is

related to the absolute accuracy of that parameter in engineering units. These are directly comparable to the DMSP data acquisition requirements

These results suggest methods to combine existing sensor data in order to improve the baseline DMSP capabilities to infer desired parameters. For example, Table 2-2 shows that the combination of T and T-2 data (cf column, 1&2), provide a more accurate integrated water vapor profile than the use of T-2 data alone (column SSM/T2). Especially note the potential improvement in temperature profile retrieval near the surface (T 1000) obtained when combining SSM/T data with that from the SSM/T-2 (column 1&2) or SSM/I (1&1). The importance of the SSM/I data combined with the SSM/T data for surface parameter retrievals is also reflected in the surface temperature and emissivity results. These midlatitude results can be compared to those for the tropics (Table 2-3). Here, for example, it can be seen that the advantage to incorporating SSM/I data along with SSM/T data for temperature profile retrieval near the surface (T 1000) demonstrated for midlatitudes is lost in the tropics. This is largely due to the smaller variance of tropical temperature profiles near the surface compared to midlatitude counterparts. (Compare columns P S. D., i.e. parameter standard deviation, for T 1000 in Tables 2-2 and 2-3.) Note that in the tropics the combination of SSM/T and SSM/I data still provide the most accurate retrievals of surface emissivity. For clarity we have plotted the retrieval results for temperature and integrated water vapor profiles as RMS errors in degrees Kelvin and g/cm^2 , respectively, as a function of pressure. These are illustrated in Figures 2-1a, b and 2-2a, b for midlatitude winter and tropical atmospheres, respectively.

2.3 Theoretical Basis of Physical Retrieval Approach

Current operational analysis procedures for the OLS, SSM/T-1, and SSM/I treat each sensor data stream independent of the others. OLS imagery is processed into global cloud property fields using an automated nephanalysis algorithm (Fye, 1978). The retrieval scheme for temperature sounding by the SSM/T-1 is based on regression of SSM/T-1 brightness temperature data against desired mandatory level temperatures (Rigone and Stogryn, 1977) and an analogous statistical approach will be used in the determination of meteorological parameters such as cloud liquid water content and precipitation (among others)

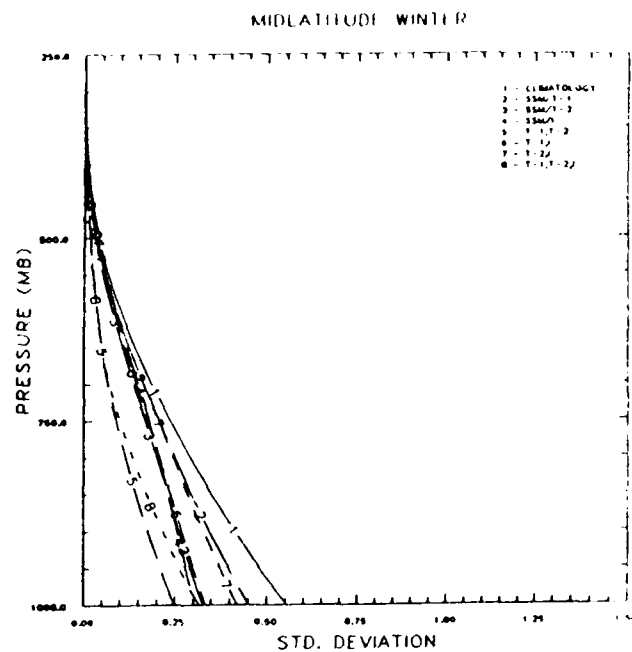
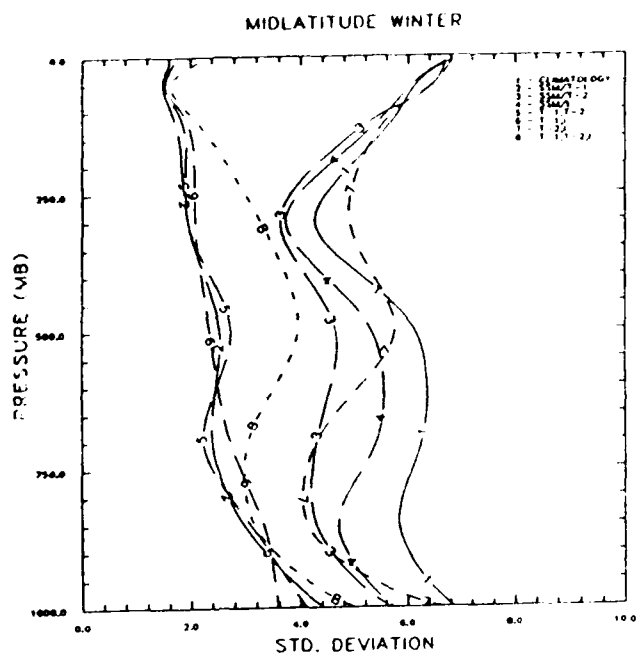


Figure 2-1 Temperature (a) and water vapor profile (b). RMS errors using statistical retrieval for midlatitude winter atmospheres.

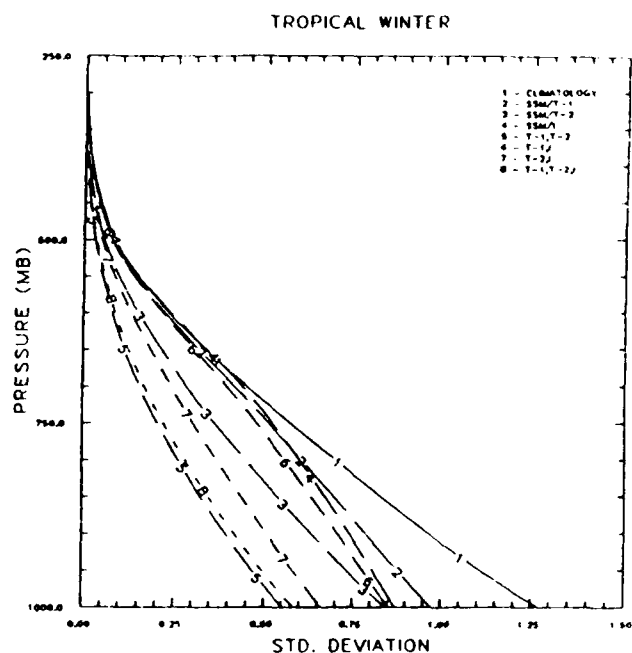
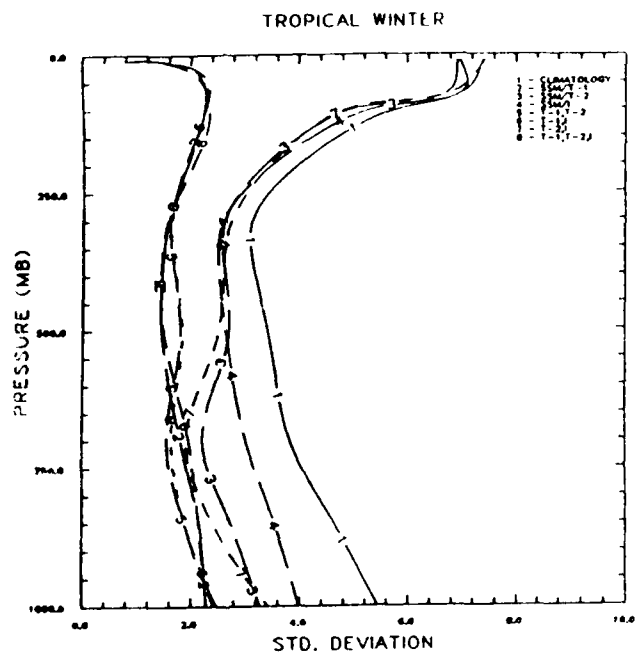


Figure 2-2 Temperature (a) and water vapor profile (b). RMS errors using statistical retrieval for tropical atmospheres.

Table 2-2. Fraction of Unexplained Variance for Statistical Retrievals:
Midlatitude Summer Atmospheres

| PARAM. | SSM/T1 | SSM/T2 | SSM/I | 1 & 2 | 1 & I | 2 & 1 | 1,2 & I | P S.D. | P MEAN |
|--------|--------|--------|--------|--------|--------|--------|---------|--------|----------|
| T 10 | 0.0571 | 1.0451 | 1.0487 | 0.0576 | 0.0628 | 1.0825 | 0.0992 | 6.7678 | 218.9875 |
| T 50 | 0.0588 | 1.1534 | 1.0212 | 0.0608 | 0.0632 | 1.1472 | 0.0718 | 6.1646 | 212.3423 |
| T 100 | 0.0810 | 0.9592 | 0.9662 | 0.0931 | 0.1017 | 1.0057 | 0.1149 | 5.8427 | 212.8881 |
| T 300 | 0.2151 | 0.7252 | 0.7649 | 0.2125 | 0.2491 | 1.3269 | 0.6011 | 4.2547 | 224.5277 |
| T 500 | 0.1763 | 0.5801 | 0.7562 | 0.2054 | 0.1503 | 0.8866 | 0.4175 | 6.1279 | 249.7131 |
| T 700 | 0.1475 | 0.4791 | 0.7577 | 0.1280 | 0.1932 | 0.4808 | 0.2393 | 6.2591 | 265.9886 |
| T 850 | 0.2597 | 0.5396 | 0.6479 | 0.2818 | 0.3243 | 0.4993 | 0.2925 | 5.8369 | 273.1358 |
| T 1000 | 0.4154 | 0.6958 | 0.7190 | 0.3583 | 0.2734 | 0.9720 | 0.5340 | 6.8623 | 277.7990 |
| U 300 | 0.7515 | 0.5441 | 0.7247 | 0.1065 | 0.6382 | 0.6703 | 0.0993 | 0.0026 | 0.0068 |
| U 500 | 0.7656 | 0.5694 | 0.7163 | 0.1478 | 0.6339 | 0.6601 | 0.1329 | 0.0400 | 0.0662 |
| U 700 | 0.7743 | 0.5545 | 0.6579 | 0.1319 | 0.6053 | 0.7806 | 0.1489 | 0.1859 | 0.2948 |
| U 1000 | 0.6667 | 0.3476 | 0.3022 | 0.1998 | 0.3655 | 0.5747 | 0.3294 | 0.5551 | 1.2548 |
| SURF T | 0.4154 | 0.6958 | 0.7190 | 0.3583 | 0.2734 | 0.9720 | 0.5340 | 6.8623 | 277.7990 |
| EMISS | 0.0269 | 0.0319 | 0.0237 | 0.0192 | 0.0109 | 0.0368 | 0.0225 | 0.1232 | 0.8041 |

from the SSM/I data (Lo, 1983). These approaches share a common heritage in the "D" matrix technique described by Gaut et al. (1975). Data from the SSM/T-1 and SSM/T-2 will be integrated together in a statistical retrieval of water vapor profiles (cf. Isaacs, 1987).

For a variety of reasons, the operational approach described above could be improved. The main criticisms are: (1) the lack of a multispectral perspective, (2) reliance on statistical retrieval approaches, which produce retrieval fields with reduced variance properties, fail to treat inherent problem nonlinearities, and provide little opportunity to monitor retrieval quality, and (3) neglect of some physical aspects of the retrieval problem, such as the effect of cloud on millimeter wave brightness temperatures. To address these issues, an alternative retrieval scheme has been developed under this effort. The approach outlined below is by no means statistically optimal. However, it does attempt to address the difficulties cited above and, in

particular, integrates available data sources in a unified, multispectral retrieval constrained by radiative transfer principles.

Table 2-3. Fraction of Unexplained Variance for Statistical Retrievals:
Tropical Summer Atmospheres

| PARAM. | SSM/T1 | SSM/T2 | SSM/I | 1 & 2 | 1 & I | 2 & I | 1,2 & I | P S.D. | P MEAN |
|--------|--------|--------|--------|--------|--------|--------|---------|--------|----------|
| T 10 | 0.0155 | 1.1274 | 0.9887 | 0.0193 | 0.0157 | 1.1363 | 0.0184 | 6.9724 | 226.3941 |
| T 50 | 0.1072 | 1.0430 | 0.9434 | 0.1184 | 0.1034 | 1.0122 | 0.1134 | 7.1249 | 204.7910 |
| T 100 | 0.1492 | 0.7357 | 0.8642 | 0.1528 | 0.1624 | 0.7120 | 0.1511 | 5.8208 | 195.5323 |
| T 300 | 0.2291 | 0.6402 | 0.6248 | 0.2414 | 0.2255 | 0.7083 | 0.2475 | 3.1300 | 240.5698 |
| T 500 | 0.1866 | 0.6352 | 0.6538 | 0.2803 | 0.1966 | 0.5569 | 0.2913 | 3.4249 | 265.9098 |
| T 700 | 0.2236 | 0.3367 | 0.6573 | 0.1651 | 0.2635 | 0.2508 | 0.1850 | 3.8224 | 280.7237 |
| T 850 | 0.2222 | 0.3520 | 0.5909 | 0.1712 | 0.2191 | 0.2705 | 0.1719 | 4.6325 | 288.0277 |
| T 1000 | 0.1784 | 0.3640 | 0.5450 | 0.2107 | 0.1787 | 0.4027 | 0.1991 | 5.4435 | 296.2430 |
| U 300 | 0.8514 | 0.3737 | 0.9687 | 0.0929 | 0.8678 | 0.2939 | 0.1102 | 0.0042 | 0.0116 |
| U 500 | 0.8684 | 0.4197 | 0.9950 | 0.1286 | 0.8185 | 0.3360 | 0.1546 | 0.0848 | 0.1515 |
| U 700 | 0.8632 | 0.3982 | 0.9431 | 0.1168 | 0.7694 | 0.2876 | 0.1389 | 0.4503 | 0.7835 |
| U 1000 | 0.5887 | 0.4425 | 0.4700 | 0.1896 | 0.4502 | 0.2734 | 0.2108 | 1.2724 | 3.7535 |
| SURF T | 0.1784 | 0.3640 | 0.5450 | 0.2107 | 0.1787 | 0.4027 | 0.1991 | 5.4435 | 296.2430 |
| EMISS | 0.0200 | 0.0419 | 0.0089 | 0.0125 | 0.0056 | 0.0094 | 0.0078 | 0.1232 | 0.8041 |

The approach is based on the simultaneous retrieval method of Smith et al. (1985) and is illustrated schematically in Figure 2-3. The first guess geophysical parameters are obtained using a multiple linear regression method (D-matrix approach using the technique described by Gaut et al., (1975)). Two data sets of geophysical parameters as well as brightness temperatures are needed to compute the first guess. One set is used to compute the D-matrix and the other to compute the first guess. The brightness temperatures are evaluated using a modified version of the RADTRAN code. This program computes brightness temperatures for microwave frequencies. The versions used at AFGL are called RAD9 and RADLIB. To do the physical retrieval (i.e., to correct the first guess), use is made of the radiative transfer equation (RTE). The RTE is varied with respect to integrated water vapor profile U, temperature profile T, surface temperature T_s , and surface emissivity ϵ_s . ΔU is expanded

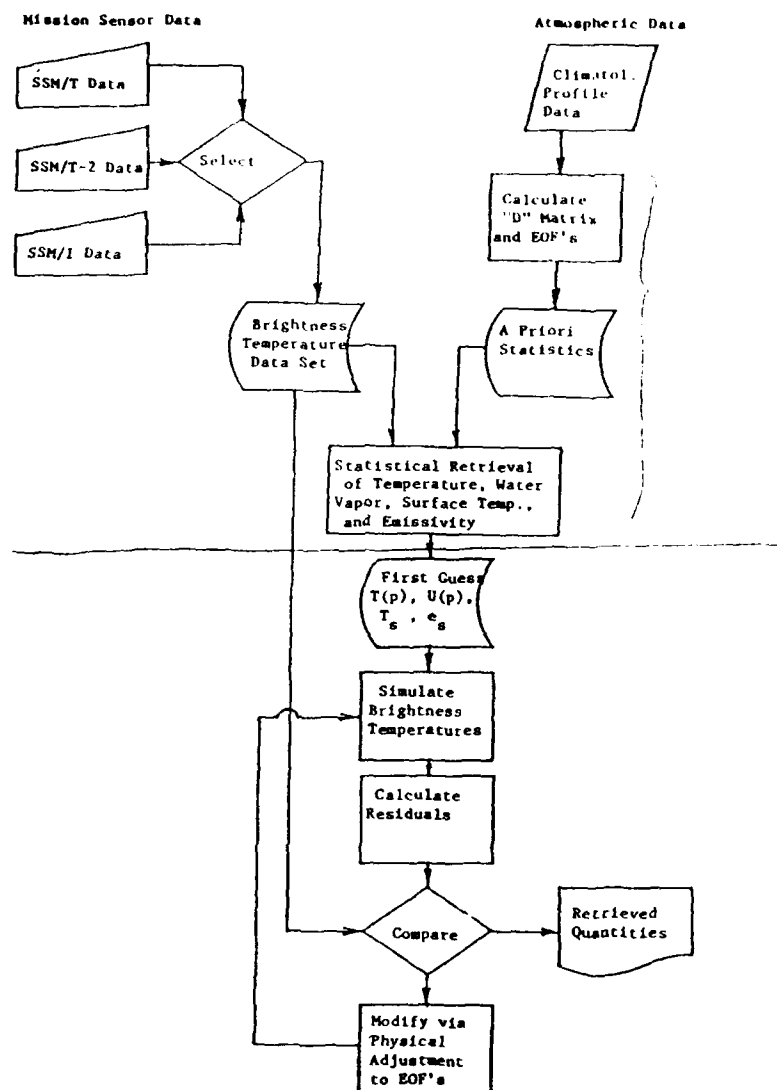


Figure 2-3. Unified retrieval algorithm for microwave mission sensor data.

in terms of the eigenvectors of the standardized (by mean) covariance matrix of U of the first data set. Similarly, ΔT is expanded in terms of the eigenvectors of the standardized (by the mean) matrix of covariance of T . The unknowns then are the coefficients of the expansions as well as a scalar for T_s and ϵ_s . After solving for these coefficients, it is then possible to correct the integrated water vapor and temperature profiles, as well as the surface temperature and the surface emissivity.

The radiative transfer equation for microwave frequencies is:

$$T_{b\nu} = [\epsilon_s T_s + (1 - \epsilon_s) \int_0^{p_s} T(p) d\tau'_\nu] \tau_\nu(p_s) + \int_{p_s}^0 T(p) d\tau_\nu \quad (2.1)$$

where

$$\tau_\nu(p) = \exp \left[- \int_0^p k(\nu, p') dp' / \mu \right] \quad (2.2)$$

and

$$\tau'_\nu(p) = \exp \left[- \int_p^{p_s} k(\nu, p') dp' / \mu \right]. \quad (2.3)$$

Here, μ is the cosine of the path zenith angle, τ_ν and τ'_ν are the upward and downward transmission functions, respectively, and p_s is the surface pressure. Specular surface reflection is assumed.

Differentiating equation (1) with respect to the desired variables U , T , T_s and ϵ_s and dropping the frequency indices, one obtains:

$$\Delta^n = \frac{\partial T_b}{\partial \epsilon_s} \delta \epsilon_s + \frac{\partial T_b}{\partial T_s} \delta T_s + \frac{\partial T_b}{\partial T} \delta T + \frac{\partial T_b}{\partial U} \delta U \quad (2.4)$$

where:

$$\frac{\partial T_b}{\partial \epsilon_s} = [T_s - \int_0^{p_s} T(p) d\tau'] \tau_{p_s} \quad (2.5)$$

$$\frac{\partial T_b}{\partial T_s} = \epsilon_s \tau_{p_s} \quad (2.6)$$

$$\delta T \frac{\partial T_b}{\partial T} = \tau_{p_s} (1 - \epsilon_s) \left\{ \int_0^{p_s} \delta T d\tau' \right\} + \int_{p_s}^0 \delta T d\tau. \quad (2.7)$$

$$\begin{aligned} \delta U \frac{\partial T_b}{\partial U} = & (\epsilon_s - 1) \left[T_s - \int_0^{p_s} T(p) dr' + r_s T(0) \right] \frac{\partial r_s}{\partial U} \delta U \\ & + \int_0^{p_s} \left[\frac{\partial r}{\partial U} + r_s (\epsilon_s - 1) \frac{\partial r'}{\partial U} \right] \delta U dT \end{aligned} \quad (2.8)$$

Parts of δU ($\partial T_b / \partial U$) have been obtained using integration by parts. Note that $(\partial r(p_s) / \partial T)$ and the variation with respect to surface pressure have been ignored.

The quantities δU and δT are expanded in series of the eigenvectors of the covariance matrices (EOFs) of U and T , with N_u and N_t terms, respectively.

$$\delta U(p) = \sum_{j=1}^{N_u} A_j \phi_j(p); \quad \delta T(p) = \sum_{j=N_u+1}^{N_u+N_t} A_j \phi_j(p) \quad (2.9-2.12)$$

$$\delta T_s = A_{N_u+N_t+1}; \quad \delta \epsilon_s = A_{N_u+N_t+2}$$

Upon substitution of (2.9 - 2.12) into (2.4) a linear equation in the coefficients A_j is obtained:

$$\Delta^n = \sum_{j=1}^{N_u+N_t+2} A_j \phi_j \quad (2.13)$$

where the ϕ_j 's are functions of the terms in equations (2.5-2.8). The desired difference terms, δ , in the relaxation equation:

$$p^n = p^{n-1} + \delta \quad (2.14)$$

are available by solving (2.13) for the A_j 's.

The ridge stabilized, least squares solution is given by:

$$A = (\Phi^T \Phi + \sigma H)^{-1} \Phi^T \Delta^n \quad (2.15)$$

where σ is the ridge parameter and the diagonal elements of the H matrix are the inverse of the fractional variance due to each EOF.

The quantities δU and δT are expanded in terms of the eigenvectors of the covariance matrix of U and T, respectively. The covariance matrix is given by:

$$\langle UU^T \rangle = [(U_{i,j} - \bar{U}_i) / \bar{U}_{i,j} - \bar{U}_i] / \bar{U}_i]^T \quad (2.16)$$

where T is equal to the transpose and $\bar{U}_i = \frac{1}{N} \sum_j U_{i,j}$, i is an index running over the number of pressure levels, and the j index is summed over the number of radiosondes, N. The covariance matrix for temperature is the same, replacing U by T. Eigenvectors and eigenvalues are obtained by diagonalizing the above covariance matrix. These are stored in the computer code as:

$$RUU_{i,j}, i = 1, NPEI \\ j = 1, NU \quad (2.17)$$

$$RTT_{i,j}, i = 1, NPEI \\ j = 1, NT$$

The eigenvalues are stored in LAMBDU(j), j = 1, NU and LAMBDT(j), j = 1, NT. The eigenvalues need to be known in the problem so as to be able to compute how many eigenvectors have to be kept in the computations. There are NPEI eigenvectors for both U and T, but only the first few (i.e., with largest eigenvalues) are kept.

The perturbations for each quantity δU , δT , $\delta \epsilon_s$, δT_s (see eqs. (2.5) - (2.8)) are then expanded in the appropriate eigenvectors:

$$\text{Let } \delta U_i = \sum_j RUU_{i,j} * A_j; j = 1, NU \\ i = 1, NPEI-64 \text{ levels} \quad (2.18)$$

$$\delta T_i = \sum_j RTT_{i,j} * A_j; j = 1 + NU, NU + NT \\ i = 1, NPEI \quad (2.19)$$

$$\delta T_{si} = A_{NU+NT+1} \quad (2.20)$$

$$\delta \epsilon_s = A_{NU+NT+2} \quad (2.21)$$

where NU = number of eigenvectors used to compute δU , NT = number of eigenvectors used to compute δT . Note that in this problem, it has been assumed that:

$$\delta T_s = \sum_j RTT_{64,j} * A_j = A_{NU+NT+1} \quad (2.22)$$

Therefore, there is really one less unknown. Note that one can also run the program if δT_s is in general different from δT (surface). Putting equation (2.1) in finite difference form and therefore using equations (2.18-2.21), one obtains:

$$\Delta_\ell^n = \delta TB_\ell^U + \delta TB_\ell^T + \delta TB_\ell^S + \delta TB_\ell^{\epsilon_s} \quad (2.23)$$

$\ell = 1, NFREQ.$

where

$$\begin{aligned} \Delta_\ell^n &= \delta TB_\ell^U \text{ if } \Delta T, \Delta T_s, \Delta \epsilon_s = 0 \\ \Delta_\ell^n &= \delta TB_\ell^T \text{ if } \Delta U, \Delta T, \Delta \epsilon_s = 0 \\ \Delta_\ell^n &= \delta TB_\ell^S \text{ if } \Delta U, \Delta T, \Delta \epsilon_s = 0 \\ \Delta_\ell^n &= \delta TB_\ell^{\epsilon_s} \text{ if } \Delta U, \Delta T, \Delta T_s = 0 \end{aligned}$$

Equation (2.23) can be solved for different combinations of geophysical parameters. For example, if ϵ_s is kept fixed, then $\Delta TB_\ell^{\epsilon_s} = 0$ and is not computed. $\ell = 1, NFREQ$ is the number of frequencies used to do the retrievals, one can choose between the 3 instruments SSM/T-1, SSM/T-2 and SSM/I.

The desired quantities U, T, T_s , and ϵ_s are obtained by solving for the A_j coefficients (see Eqs. (2.18-2.21) where $j = 1, NU + NT + 2$. From equations (2.5) through (2.8), we have:

$$(a) \delta T_{B_\ell}^{\epsilon_s} = (\beta_{i,\ell})^T A_i \quad \begin{aligned} &\text{for } i = NU+NT+2 \\ &\ell = 1, NFREQ \\ &NLEV = \text{surface level} \end{aligned} \quad (2.24)$$

$$\beta_{i,\ell} = r(NLEV, \ell)(T_s - T_\ell)$$

where:

$$T_{1,l} = \sum_k T_k (\tau_{k+1,l} - \tau_{k,l}); \quad k=1, \text{ NLEV}-1 \\ \ell=1, \text{ NFREQ}$$

$$(b) \delta T_{B_l}^T = (\beta_{i,l})^T A_i \quad \text{for } i=NU+NT+1 \quad (2.25) \\ \ell=1, \text{ NFREQ}$$

$$\beta_{i,l} = \tau(\text{NLEV}, \ell) \epsilon_s$$

$$(c) \delta T_{B_l}^T = (\beta_{i,l})^T A_i \quad \text{for } i=NU+1, \text{ NU}+NT \quad (2.26) \\ \ell=1, \text{ NFREQ} \\ k=1, \text{ NLEV}-1$$

$$\beta_{i,l} = \sum_k (RTT_{k,i})^T \left\{ \tau(\text{NLEV}, \ell) (1 - \epsilon_s) \cdot \right. \\ \left. [\tau'(k+1, \ell) - \tau'(k, \ell)] + [\tau(k, \ell) - \tau(k+1, \ell)] \right\}$$

$$(d) \delta T_{B_l}^U = (\beta_{i,l})^T A_i \quad \text{for } i=1, \text{ NU} \quad (2.27) \\ \ell=1, \text{ NFREQ} \\ k=1, \text{ NLEV}-1$$

$$\beta_{i,l} = RUU_{\text{NLEV}, i} \left(\frac{\partial \tau}{\partial U} \right)_{\text{NLEV}-1, \ell} (\tau_{S-1}) \\ \left\{ \tau(\text{NLEV}, \ell) T_1 + T_S - T_{1,l} \right\} \\ + \sum_k (RUU_{k,i})^T (T_{k+1} - T_k) \left\{ \left(\frac{\partial \tau}{\partial U} \right)_{k, \ell} + \tau(\text{NLEV}, \ell) \right. \\ \left. (\epsilon_s - 1) \left(\frac{\partial \tau'}{\partial U} \right)_{k, \ell} \right\}$$

where $T_1 = T_{k=1}$

$$T_{1,l} = \int_0^P T d\tau'$$

$$\left(\frac{\partial \tau'}{\partial U} \right)_{h,i} = (\tau'_{k,\ell} - \tau'_{k-1,\ell}) / (U_k - U_{k+1})$$

$$\left(\frac{\partial r}{\partial U}\right)_{k,l} = (r_{k,l} - r_{k+1,l}) / (U_k - U_{k+1})$$

$$\text{define } \text{PHI}_{\ell,i} = [\beta_{i,\ell}]^T$$

$$\text{Least squares solution of } \delta \text{TB}_{\ell} = \sum_i \text{PHI}_{\ell,i}^* A_i; \quad i = 1, \text{NU} + \text{NT} + 2 \\ \ell = 1, \text{NFREQ}$$

$$A_i = [\text{PHI}_{\ell,i} [\text{PHI}_{\ell,i}]^T + \sigma H_{i,i}]^{-1} [\text{PHI}_{\ell,i}]^T \delta \text{TB}_{\ell}; \quad i = 1, \text{NU} + \text{NT} \\ \ell = 1, \text{NFREQ} \quad (2.28)$$

$$\text{where } H_{i,i} = 1 / \left\{ \lambda_i / \left(\sum_{i=1}^M \lambda_i \right) \right\}; \quad i = 1, \text{NU} + \text{NT} \quad (2.29)$$

$$\text{and } H_{\text{NU} + \text{NT} + 1, \text{NU} + \text{NT} + 1} = 1.0; \quad H_{\text{NU} + \text{NT} + 2, \text{NU} + \text{NT} + 2} = 1.0 \quad (2.30)$$

2.4 Results for Retrieval of Temperature and Integrated Water Vapor Using SSM/T-1 and SSM/T-2

In this section, we describe results for the simultaneous retrieval of water vapor and temperature profiles using the SSM/T-1 microwave temperature sounder and SSM/T-2 millimeter wave moisture sounder instruments. The channel frequencies and noise equivalent brightness temperatures used in our simulations are provided in Table 2-1. The noise values were assumed Gaussian with a zero mean, i.e., no instrumental bias was considered. The adopted noise values in Table 2-1 represented design goals and probably underestimate actual sensor noise including scene noise. Therefore, the retrieval results presented should be viewed as best case retrievals.

The atmospheric profiles of temperature and water vapor used in the brightness temperature simulations are from a radiosonde data set collected by Phillips et al., 1988. Subsets of the original data set were created consisting of 200 radiosondes each corresponding to tropical winter profiles over the ocean (TWO) and midlatitude winter profiles over the ocean (MWO), respectively. One half of each set (denoted set 1) was used to develop first guess and EOF statistics, while the other half (i.e., set 2) was used to perform retrievals.

Below we describe the results for the simultaneous retrieval approach. The first guess was derived either from statistics or using the ensemble

mean. The corrections to the first guess were obtained using the eigenvector method with 1 iteration only (in general).

2.4.1 Statistical Estimates as First Guess

Multiple linear regression (i.e., the D-matrix approach) was used to obtain first guess estimates of the desired geophysical parameters. To obtain these estimates, all the channels of the SSM/T-1 and SSM/T-2 are used. To correct the first guesses, two options were considered. The first used a selective number of channels for SSM/T-1 and a scalar to compute the corrections rather than eigenvectors. The second method used all the channels of the SSM/T-1 and the eigenvectors to compute the corrections.

2.4.1.1 Selective Channels for the SSM/T-1

Retrievals for temperature and integrated water vapor have been done using all channels for SSM/T-1. The corrections obtained to the statistical first guesses give better results than the first guess for surface variables only (i.e., the layer 1-1000 mb for water vapor and the air temperature at 1000 mb as well as the ground temperature).

Therefore, the eigenvector method for the temperature profile retrieval has been changed to a scalar by only correcting the surface temperature. For the integrated water vapor corrections, the eigenvectors of the covariance matrix for water vapor are still used. For these computations and the ones following, two new rejection criteria for integrated water vapor have been added. These are number 2 and 3 in the list following.

Criteria for rejection of updating the first guess of an integrated water vapor profile:

Reject updated profile if:

1. The corrected water vapor profile has negative values of integrated water vapor (at one of the 64 levels).
2. The integrated water vapor for the layers 1-300mb, 1-500, 1-700 and 1-1000mb is nonmonotonic.

3. The water vapor for the layer 1-700mb is larger than 0.4 times the water vapor for the layer 1-1000mb. Table 2-4 contains the ratios of the mean of integrated water vapor for all the layers -- $U(1-700\text{mb})/U(1-1000\text{mb})$ is around 20% for both data sets.

If a particular integrated water vapor profile satisfies one of these criteria, then the newly computed values of integrated water vapor are set back to the first guess.

Table 2-4. Ratios of Mean Integrated Water Vapor

| | TWO1 | TWO2 | MWO1 | MWO2 |
|-----------|-------|-------|-------|-------|
| U(1)/U(4) | 0.3% | 0.3% | 0.54% | 0.54% |
| U(2)/U(4) | 4.0% | 4.0% | 5.0% | 5.3% |
| U(3)/U(4) | 20.1% | 20.9% | 22.3% | 23.5% |

U(1)=U(1-300MB), U(2)=U(1-500MB), U(3)=U(1-700MB), U(4)=U(1-1000MB)

The results for the selective channel method are shown in Table 2-5. The layer 1-500mb shows a small improvement and the total integrated water vapor shows almost no improvement. The layer 500-700mb shows no improvement at all. The surface temperature shows a slight improvement for the midlatitude winter set. (Note that all temperature levels except for the surface have been kept fixed.)

2.4.1.2 All Channels for SSM/T-1

The first method used to do retrievals of integrated water vapor and temperature used eigenvectors for both temperature and water vapor. However, the number of eigenvectors used for temperature was high (i.e., 6 to 7). The results obtained were disappointing and therefore the method of using a scalar only for the temperature correction was tried. It turns out that using eigenvectors for both temperature and integrated water vapor gives better results, provided a lower number of eigenvectors is used for the temperature. The results improve only for the surface temperature (ground temperature) and the total integrated water vapor. Tables 2-6 and 2-7 show results for dif-

ferent values of sigma, H and number of eigenvectors for tropical and mid-latitude cases, respectively. Both noise and no noise cases are shown.

Table 2-5. Simultaneous Retrieval Results Using Statistical First Guess and Selective Channels.

| | | | | | | |
|------------------|----------------|--------|--------|-----------------------|--------|--------|
| Data set: | TW02 | | | MW02 | | |
| H2O: # of eig's | 4 | | | 3 | | |
| T: # of eig's | 0 | | | 0 | | |
| SSM/T-1 channels | 50.5, 53.2 GHz | | | 50.5, 53.2, 54.35 GHz | | |
| sigma | 1e-05 | | | 1e-05 | | |
| U (gr/sq cm) | RMSOE(*) | RMSFE | RMSCLI | RMSOE | RMSFE | RMSCLI |
| 1-300mb | .00129 | .00129 | .00423 | .00085 | .00085 | .00261 |
| 1-500mb | .0304 | .0267 | .0848 | .0154 | .0132 | .0400 |
| 1-700mb | .154 | .240 | .450 | .0675 | .0824 | .186 |
| 1-1000mb | .554 | .543 | 1.27 | .248 | .230 | .555 |
| T (K) | | | | | | |
| 10 mb | .97 | | 6.97 | 1.62 | | 6.77 |
| 50 mb | 2.45 | | 7.13 | 1.52 | | 6.16 |
| 100 mb | 2.28 | | 5.82 | 1.78 | | 5.84 |
| 300 mb | 1.63 | | 3.31 | 1.96 | | 4.25 |
| 500 mb | 1.81 | | 3.43 | 2.78 | | 6.13 |
| 700 mb | 1.55 | | 3.82 | 2.24 | | 6.26 |
| 850 mb | 1.92 | | 4.63 | 3.10 | | 5.84 |
| 1000mb | 2.50 | 2.82 | 5.44 | 4.11 | 3.31 | 6.86 |

(*) Tolerance - tolerance criterion to stop computations.
RMSOE - rms error between first guess and exact solution.
RMSFE - rms error between final and exact solution.
RMSCLI - rms error of climatology alone.

Table 2-6. Simultaneous Retrieval Results for Tropical Data Set: (a) Noise,
(b) No Noise.

(a) Instrument Noise Added

| | | | | |
|---|-------------|------|----|----|
| H | # of eig's: | 4 | 4 | 4 |
| T | # of eig's: | 4 | 3 | 4 |
| | sigma | 1e-5 | .1 | .1 |

| | | | | |
|-------------|--------|-----------|--------|--------|
| H | | λ | I | I |
| U(gr/sq cm) | RMSOE | RMSFE | RMSFE | RMSFE |
| 1-300mb | .00129 | .00129 | .00129 | .00129 |
| 1-500mb | .0304 | .0302 | .0303 | .0310 |
| 1-700mb | .154 | .216 | .308 | .259 |
| 1-1000mb | .554 | .531 | .439 | .493 |

T (K)

| | | | | |
|--------|------|------|------|------|
| 10 mb | .97 | 1.34 | 1.52 | 1.46 |
| 50 mb | 2.45 | 2.45 | 2.55 | 2.51 |
| 100 mb | 2.28 | 3.21 | 2.30 | 3.76 |
| 300 mb | 1.63 | 2.29 | 1.92 | 1.98 |
| 500 mb | 1.81 | 1.95 | 2.13 | 1.96 |
| 700 mb | 1.55 | 1.89 | 1.99 | 2.11 |
| 850 mb | 1.92 | 2.15 | 2.33 | 2.23 |
| 1000mb | 2.50 | 2.32 | 2.36 | 2.21 |

(b) No Instrument Noise

| | | | | | | |
|------------------|-------------|-----------|-----------|-----------|-----------|-----------|
| H ₂ O | # of eig's: | 4 | 4 | 4 | 4 | 4 |
| T | # of eig's: | 4 | 4 | 3 | 3 | 3 |
| | sigma | 1e-5 | 1e-3 | 1e-05 | 1e-03 | 1e-10 |
| H | | λ | λ | λ | λ | λ |

| | | | | | | |
|-------------|--------|--------|--------|--------|--------|--------|
| U(gr/sq cm) | RMSOE | RMSFE | RMSFE | RMSFE | RMSFE | RMSFE |
| 1-300mb | .00100 | .00100 | .00100 | .00100 | .00100 | .00100 |
| 1-500mb | .0256 | .0264 | .0257 | .0253 | .0251 | .0253 |
| 1-700mb | .116 | .159 | .214 | .223 | .195 | .227 |
| 1-1000mb | .425 | .405 | .419 | .374 | .409 | .374 |

T (K)

| | | | | | | |
|--------|------|------|------|------|------|------|
| 10 mb | .526 | 1.04 | 1.02 | 1.11 | 1.08 | 1.11 |
| 50 mb | 1.81 | 1.73 | 1.97 | 1.92 | 2.02 | 1.91 |
| 100 mb | 1.57 | 2.40 | 3.51 | 2.28 | 1.81 | 2.31 |
| 300 mb | 1.06 | 2.10 | 1.56 | 1.52 | 1.29 | 1.53 |
| 500 mb | 1.31 | 1.56 | 1.57 | 1.82 | 1.71 | 1.83 |
| 700 mb | 1.33 | 1.68 | 2.15 | 2.00 | 1.85 | 2.01 |
| 850 mb | 1.64 | 1.83 | 2.12 | 2.08 | 2.10 | 2.08 |
| 1000mb | 2.31 | 2.00 | 1.97 | 2.18 | 2.25 | 2.19 |

Table 2-7. Simultaneous Retrieval Results for Midlatitude Data Set:
(a) Noise, (b) No Noise

(a) Instrument Noise Added

| | | | | | |
|------------------------------|-----------|-----------|-----------|-----------|-----------|
| sigma: | 1e-10 | 1e-05 | 1e-05 | 1e-02 | 1e-01 |
| H: | λ | λ | λ | λ | λ |
| H ₂ O # of eig's: | 3 | 3 | 3 | 3 | 3 |
| T # of eig's: | 4 | 3 | 4 | 4 | 4 |
| U (gr/sq cm) | RMSOE | RMSFE | RMSFE | RMSFE | RMSFE |
| 1-300mb: | .00085 | .00085 | .00085 | .00085 | .00085 |
| 1-500mb: | .01538 | .01601 | .01503 | .01539 | .01417 |
| 1-700mb: | .06752 | .11226 | .13287 | .11208 | .12056 |
| 1-1000mb: | .24814 | .27720 | .28392 | .27360 | .25983 |

T (K)

| | | | | | | |
|---------|------|------|------|------|------|------|
| 10 mb: | 1.62 | 1.67 | - | 1.71 | 1.84 | 1.85 |
| 50 mb: | 1.52 | 1.54 | - | 1.56 | 1.64 | 1.64 |
| 100 mb: | 1.78 | 2.18 | - | 2.40 | 2.06 | 2.06 |
| 300 mb: | 1.96 | 3.40 | - | 3.68 | 3.02 | 3.01 |
| 500 mb: | 2.78 | 3.70 | - | 3.63 | 2.99 | 3.00 |
| 700 mb: | 2.24 | 3.18 | - | 3.39 | 3.16 | 3.16 |
| 850 mb: | 3.10 | 3.69 | - | 3.80 | 3.83 | 3.83 |
| 1000mb: | 4.11 | 3.63 | 3.67 | 3.44 | 3.35 | 3.36 |

(b) No Instrument Noise

| | | | | | |
|------------------------------|-----------|-----------|-----------|-----------|-----------|
| sigma: | 1e-10 | 1e-05 | 1e-05 | 1e-02 | 1e-01 |
| H ₂ O # of eig's: | 3 | 3 | 3 | 3 | 3 |
| T # of eig's: | 4 | 3 | 4 | 4 | 4 |
| H: | λ | λ | λ | λ | λ |
| U(gr/sq cm) | RMSOE | RMSFE | RMSFE | RMSFE | RMSFE |
| 1-300mb: | .00071 | .00071 | .00071 | .00071 | .00071 |
| 1-500mb: | .01413 | .01425 | .01384 | .01438 | .01301 |
| 1-700mb: | .06464 | .08961 | .10642 | .09317 | .09571 |
| 1-1000mb: | .23345 | .19612 | .20735 | .19482 | .19571 |

T (K)

| | | | | | | |
|---------|------|------|------|------|------|------|
| 10 mb: | 1.42 | 1.41 | 1.53 | 1.44 | 1.53 | 1.53 |
| 50 mb: | 1.13 | 1.12 | 1.23 | 1.16 | 1.28 | 1.28 |
| 100 mb: | 1.46 | 1.64 | 1.70 | 1.56 | 1.66 | 1.67 |
| 300 mb: | 1.55 | 2.41 | 1.59 | 2.41 | 2.02 | 2.02 |
| 500 mb: | 2.35 | 2.98 | 2.86 | 2.99 | 2.61 | 2.61 |
| 700 mb: | 1.57 | 2.56 | 2.53 | 2.75 | 2.33 | 2.33 |
| 850 mb: | 2.85 | 3.42 | 3.41 | 3.50 | 3.49 | 3.49 |
| 1000mb: | 2.80 | 2.62 | 2.52 | 2.41 | 2.29 | 2.30 |

The results depend a lot on the number of eigenvectors used as well as on the value of sigma.

A method using a different criterion for convergence has also been used. The criterion used so far is based on the total rms of the brightness temperature residuals. By the total, we imply the residuals for all the frequencies, SSM/T-2 as well as SSM/T-1.

The new criterion consist of 3 instead of 1 criterion. The first one consists of the rms for the residuals of brightness temperatures for the SSM/T-2. The second one consists of the rms for the residuals of brightness temperatures for the SSM/T-1. The third one consists of the brightness temperature for the 50.5 GHz channel.

Conditions for possible update of first guess:

TBRMS(0) = RMS of residuals of first guess - synthetic
TBRMS(0) SSM/T-2 > 1K then possibly update water vapor
TBRMS(0) SSM/T-1 < 0.5 K and TBRMS 50.5 GHz > 0.6 K then possibly
update surface temperature
TBRMS(0) SSM/T-1 > 0.5 K then possibly update surf. temp. and temp.

Above possibility rejected if:

TBRMS(1) = rms of residuals of corrected - synthetic
If TBRMS SSM/T-2 diverges then do not update water vapor
If TBRMS 50.5 GHz diverges then do not update sur. temp.
If TBRMS SSM/T-1 diverges then do not update temperature profile
(does not include surface temperature)

Results are shown in Table 2-8a,b for noise and no noise cases and 2-9a,b for tropical midlatitude noise and no noise cases.

Table 2-8. Results for New Convergence Criteria, Tropical Atmospheres:
(a) Noise, (b) No Noise

(a) With Instrument Noise

H₂O: 4 eigenvectors

T: 4 eigenvectors

First guess - statistical

TOL(1) = TOL(SSM/T-1) = 0.5

TOL(2) = TOL(SSM/T-2) = 1.0

Tolerance on surface channel = 50.5 GHz channel = 0.6 K

| H | λ | | I |
|--------------|------------------|---------|----------------|
| | sigma = 1e-05 | | sigma = 0.1 |
| U (gr/sq cm) | RMSOE | RMSFE | RMSFE |
| 1-300mb: | .00129 | .00129 | .00129 |
| 1-500mb: | .03040 | .03119 | .03062 |
| 1-700mb: | .15387 | .24773 | .31013 |
| 1-1000mb: | .55407 | .52818 | .51102 |
| T (K) | | | |
| 10 mb: | .96716 | 1.22472 | 1.33096 |
| 50 mb: | 2.45061 | 2.40394 | 2.55526 |
| 100 mb: | 2.27512 | 2.67906 | 2.85289 |
| 300 mb: | 1.62588 | 2.07338 | 1.85120 |
| 500 mb: | 1.81382 | 1.89326 | 1.92000 |
| 700 mb: | 1.55331 | 1.72099 | 1.88397 |
| 850 mb: | 1.91596 | 2.03671 | 2.09029 |
| 1000mb: | 2.49872 | 1.97584 | 2.17187 |

Table 2-8. Results for New Convergence Criteria, Tropical Atmospheres:
(a) Noise, (b) No Noise (continued)

(b) Without Instrument Noise

First guess - statistical
TOL(1) = TOL(SSM/T-1)=0.5
TOL(2) = TOL(SSM/T-2)=1.0
NITER = 1.0

Tolerance on surface channel convergence = 0.6, surface channel = 50.5 GHz

| | | | | |
|-----------------|-----------|-----------|-----------|-----------|
| H: | λ | λ | λ | λ |
| H2O # of eig's: | 4 | 4 | 4 | 4 |
| T # of eig's: | 3 | 3 | 3 | 4 |
| Sigma: | .1 | 1e-5 | 1e-10 | 1e-05 |

| | RMSOE | RMSFE | RMSFE | RMSFE | RMSFE |
|-------------|--------|--------|--------|--------|--------|
| U(gr/sq cm) | | | | | |
| 1-300mb: | .00100 | .00100 | .00100 | .00100 | .00100 |
| 1-500mb: | .0256 | .0250 | .0259 | .0259 | .0262 |
| 1-700mb: | .116 | .208 | .222 | .226 | .290 |
| 1-1000mb: | .425 | .399 | .387 | .389 | .380 |

T (K)

| | | | | | |
|---------|------|------|------|------|------|
| 10 mb: | .526 | 1.04 | 1.13 | 1.14 | .89 |
| 50 mb: | 1.81 | 2.00 | 1.92 | 1.92 | 1.75 |
| 100 mb: | 1.57 | 1.66 | 2.33 | 2.35 | 1.91 |
| 300 mb: | 1.06 | 1.13 | 1.49 | 1.50 | 1.73 |
| 500 mb: | 1.31 | 1.52 | 1.72 | 1.73 | 1.48 |
| 700 mb: | 1.33 | 1.54 | 1.81 | 1.82 | 1.63 |
| 850 mb: | 1.64 | 1.88 | 1.80 | 1.80 | 1.78 |
| 1000mb: | 2.31 | 2.31 | 1.82 | 1.82 | 1.78 |

Table 2-9. Results for New Convergence Criteria, Midlatitude Atmospheres:
(a) Noise, (b) No Noise

(a) With Instrument Noise

Midlatitude winter ocean set 2

H₂O # of eigenvectors: 3

T # of eigenvectors: 4

First guess = statistical

TOL(1) = TOL(SSM/T-1)

TOL(2) = TOL(SSM/T-2)

NITER = 1

Tolerance on surface channel = 50.5 GHz channel = 0.6K

| | | | |
|-------------|--------|-----------|-----------|
| TOL(1): | | 1.0 | 0.5 |
| TOL(2): | | 0.0 | 1.0 |
| H: | | λ | λ |
| sigma: | | 1e-05 | 1e-05 |
| U(gr/sq cm) | RMSOE | RMSFE | RMSFE |
| 1-300mb | .00085 | .00085 | .00085 |
| 1-500mb | .01538 | .01565 | .01656 |
| 1-700mb | .06752 | .11077 | .12348 |
| 1-1000mb | .24814 | .26563 | .26780 |

T (K)

| | | | |
|--------|------|------|------|
| 10 mb | 1.62 | 1.64 | 1.59 |
| 50 mb | 1.52 | 1.53 | 1.56 |
| 100 mb | 1.78 | 1.83 | 1.90 |
| 300 mb | 1.96 | 2.14 | 2.26 |
| 500 mb | 2.78 | 2.77 | 2.85 |
| 700 mb | 2.24 | 2.31 | 2.46 |
| 850 mb | 3.10 | 3.19 | 3.31 |
| 1000mb | 4.11 | 2.93 | 2.93 |

Table 2-9. Results for New Convergence Criteria, Midlatitude Atmospheres:
(a) Noise, (b) No Noise (continued)

(b) Without Instrument Noise

| | | |
|---------|-----------|-----------|
| TOL(1): | 1.0 | 0.5 |
| TOL(2): | 0.0 | 1.0 |
| H: | λ | λ |
| Sigma: | 1e-05 | 5e-05 |

| U(gr/sq cm) | RMSOE | RMSFE | RMSFE |
|-------------|-------|-------|-------|
|-------------|-------|-------|-------|

| | | | |
|-----------|--------|--------|--------|
| 1-300mb: | .00071 | .00071 | .00071 |
| 1-500mb: | .01413 | .01470 | .01490 |
| 1-700mb: | .06464 | .10432 | .10285 |
| 1-1000mb: | .23345 | .19187 | .19974 |

T (K)

| | | | |
|---------|------|------|------|
| 10 mb: | 1.42 | 1.41 | 1.46 |
| 50 mb: | 1.13 | 1.13 | 1.12 |
| 100 mb: | 1.46 | 1.50 | 1.58 |
| 300 mb: | 1.55 | 1.73 | 1.97 |
| 500 mb: | 2.35 | 2.48 | 2.74 |
| 700 mb: | 1.57 | 1.75 | 2.04 |
| 850 mb: | 2.85 | 2.95 | 3.16 |
| 1000mb: | 2.80 | 1.84 | 2.14 |

2.4.2 Mean Values of First Set as First Guess

If full statistical data to develop regression coefficients for a statistical retrieval is not available, a climatological mean profile might be an appropriate first guess. In this section we investigate the use of a mean first guess. The mean of data set 1 for both temperature and integrated water vapor profiles is used. The means are given at 4 levels for water vapor and 8 levels for temperature. These values are then interpolated to the 64 levels used by "RADTRAN."

Since the first guess is set equal to the mean of set 1, the RMS error of set 2 is approximately equal to the standard deviation of set 2. The eigenvector method was used for both temperature and integrated water vapor. This permits corrections at all levels for both temperature and integrated water vapor. Results are shown in Table 2-10 for one iteration and adding instrument noise. In this calculation only the total RMS convergence criteria was

used. Significant improvement is obtained for the total integrated water vapor for both data sets. For the tropical winter over ocean data set, the percentage of improvement over the first guess is 22% and for midlatitude winter ocean it is 14%. The temperatures for both data sets also show improvement. Levels with the largest improvements are 10 and 50 mb and the surface for the midlatitude winter over ocean data set. These results show that the physical retrieval is working since the first guess is quite bad.

Table 2-10. Retrieval Results Using Mean as a First Guess (Single Convergence Criteria Only)

| | | |
|------------------------------|-----------|-----------|
| Data set: | TWO 2 | MW02 |
| H ₂ O # of eig's: | 4 | 3 |
| T # of eig's: | 3 | 3 |
| sigma: | 1e-05 | 1e-05 |
| H: | λ | λ |
| # of iter's: | 1 | 1 |
| Tolerance: | 1.0 | 1.0 |

| U(gr/sq cm) | RMSOE | RMSFE | RMSCLI | RMSOE | RMSFE |
|-------------|--------|--------|--------|--------|--------|
| 1-300mb: | .00423 | .00423 | .00423 | .00263 | .00263 |
| 1-500mb: | .08483 | .07983 | .08479 | .04064 | .03846 |
| 1-700mb: | .45093 | .52203 | .45030 | .18775 | .17852 |
| 1-1000mb: | 1.2729 | .99557 | 1.2724 | .55725 | .47698 |

| T (K) | | | | |
|----------|------|------|------|------|
| 10 mb: | 6.98 | 5.57 | 6.93 | 5.57 |
| 50 mb: | 7.14 | 5.0 | 6.31 | 4.81 |
| 100 mb: | 5.87 | 6.2 | 5.97 | 4.55 |
| 300 mb: | 3.33 | 3.15 | 4.26 | 4.00 |
| 500 mb: | 3.52 | 3.39 | 6.17 | 5.42 |
| 700 mb: | 3.88 | 3.78 | 6.34 | 5.60 |
| 850 mb: | 4.64 | 4.8 | 5.86 | 5.37 |
| 1000 mb: | 5.46 | 5.43 | 6.87 | 5.73 |

A selective criterion of convergence has also been used with the first guess equal to the mean. The results are shown in Table 2-11. The criterion is the same as the one described above.

Table 2-11. Retrieval Results Using Selective Criteria for Convergence:
(a) Noise, (b) No Noise

Midlatitude winter ocean set 2

First guess = mean of data set 1.

Instruments: SSM/T-1 and SSM/T-2

(Use three criteria of rejection for water vapor profiles)

TOL(1) = TOL(SSM/T-1) = 0.5

TOL(2) = TOL(SSM/T-2) = 1.0

(a) Noise Added

| | | |
|------------------------------|-----------|-----------|
| H: | λ | λ |
| sigma: | 1e-05 | 1e-05 |
| H ₂ O # of eig's: | 3 | 3 |
| T # of eig's: | 4 | 3 |

| U(gr/ sq cm) | RMSOE | RMSFE | RMSFE |
|--------------|--------|--------|--------|
| 1-300mb | .00263 | .00263 | .00263 |
| 1-500mb | .04042 | .03954 | .03876 |
| 1-700mb | .18775 | .23193 | .17993 |
| 1-1000mb | .55725 | .50205 | .47380 |

T (K)

| | | | |
|--------|------|------|------|
| 10 mb | 6.93 | 4.84 | 5.57 |
| 50 mb | 6.31 | 4.07 | 4.81 |
| 100 mb | 6.00 | 4.57 | 4.53 |
| 300 mb | 4.26 | 5.88 | 3.93 |
| 500 mb | 6.17 | 7.40 | 5.43 |
| 700 mb | 6.34 | 7.05 | 5.58 |
| 850 mb | 5.86 | 5.98 | 5.37 |
| 1000mb | 6.87 | 5.57 | 5.67 |

Table 2-11. Retrieval Results Using Selective Criteria for Convergence:
(a) Noise, (b) No Noise (continued)

(b) No Noise

| | | |
|------------------------------|-----------|-----------|
| H: | λ | λ |
| sigma: | $1e-5$ | $1e-5$ |
| H ₂ O # of eig's: | 3 | 3 |
| T # of eig's: | 4 | 3 |

| | RMSOE | RMSFE | RMSFE |
|---------------|--------|--------|--------|
| U(gr/ sq cm) | | | |
| 1-300mb | .00263 | .00263 | .00263 |
| 1-500mb | .04042 | .03996 | .03786 |
| 1-700mb | .18775 | .23977 | .17884 |
| 1-1000mb | .55725 | .48121 | .46649 |
| T (K) | | | |
| 10 mb | 6.93 | 4.55 | 5.23 |
| 50 mb | 6.31 | 4.05 | 4.55 |
| 100 mb | 5.97 | 4.63 | 4.21 |
| 300 mb | 4.26 | 6.04 | 3.91 |
| 500 mb | 6.17 | 7.85 | 5.38 |
| 700 mb | 6.34 | 7.39 | 5.54 |
| 850 mb | 5.86 | 6.16 | 5.28 |
| 1000mb | 6.87 | 5.28 | 5.67 |

2.4.3 Results Summary

As indicated in the previous sections, a physical retrieval step such as that described in Section 2.3 can improve the accuracy of the statistically based first guess retrieval results. The tabulated results show that the degree of improvement is a function of the parameters of the physical retrieval step such as: (a) the number of eigenvectors used to express the temperature and water vapor profiles, (b) the ridge parameter (i.e. σ) used in the retrieval, (c) the form of the smoothing matrix (i.e. either the identity matrix or that based on eigenvalue scaling), (d) and the constraints used to terminate the iterations based on the residuals (Δ_i^n). In general it is noted that a few eigenvectors (3 or 4 for temperature, and 2 or 3 for water vapor), a ridge parameter of about 10^{-1} , the eigenvalue smoothing, and separate (rather than total RMS) constraints seem to perform best.

After concluding the series of calculations described above an error in the computer code was corrected which improved the results reported above.

Results of the physical retrieval for the tropical temperature and integrated water vapor profiles are shown in Figures 2-4a,b, respectively. The statistical first guesses described in the previous section were employed and the necessary EOFs of temperature and water vapor are evaluated from the radiosonde data set used in the generation of the first guess retrieval statistics. Physical adjustment of the temperature profile results in a slight increase of RMS error in the vicinity of the tropopause and a small improvement in accuracy near the surface. The tropopause problem is attributable both to EOF truncation representation errors and the generally weak contribution functions in this region. There is a much more noticeable improvement on the accuracy of water vapor results. Retrieval of low level moisture is considerably improved by the physical adjustment applied to the statistical first guess results. This is understandable since the physical retrieval process directly treats the inherently nonlinear dependence of channel brightness temperatures on water vapor which is not well represented by the first guess linear regression.

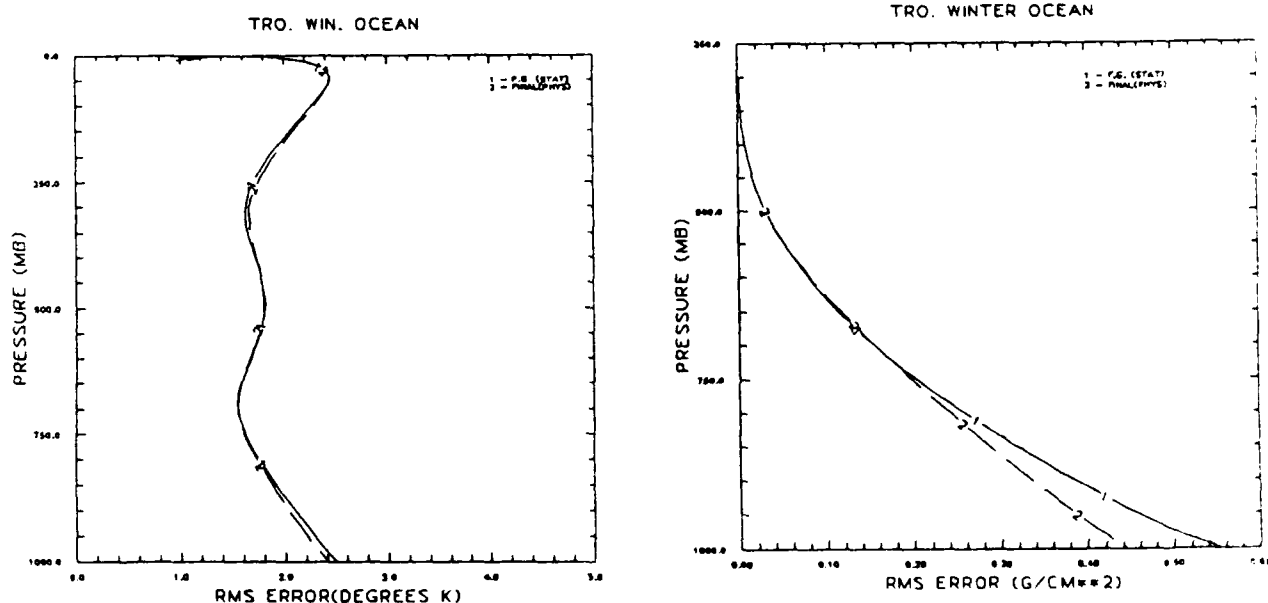


Figure 2-4. Physical retrieval results for the tropical cases.

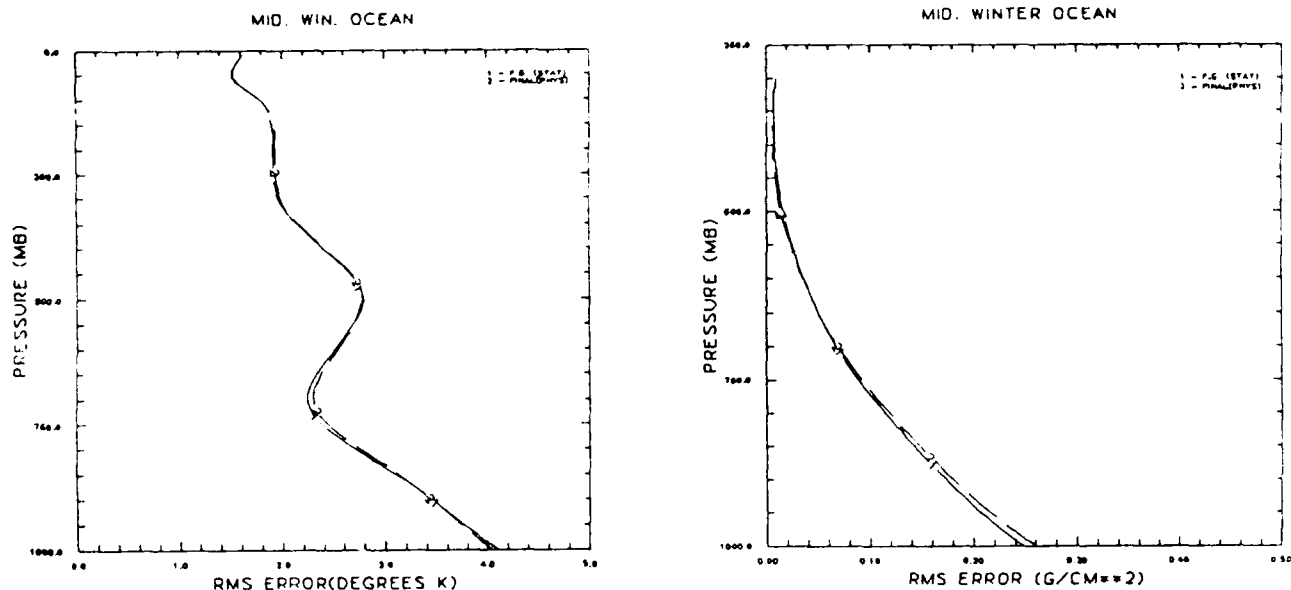


Figure 2-5. Physical retrieval results for midlatitude cases.

Results for midlatitudes are shown in Figures 2-5a, b for temperature and water vapor, respectively. For this ensemble of atmospheres no improvement over the statistical first guess is evident. However, it is worth noting that the results are not degraded either, and, having passed the brightness temperature residual comparison, the quality of the statistical first guesses for the ensemble have been verified.

2.5 The Effect of Clouds on Millimeter Wave Moisture Retrievals

To investigate the cloud signal on the various DMSP SSM/T-2 channels, both sensitivity and retrieval calculations were done. Channel weighting function and brightness temperature sensitivities to a cloud model were evaluated by inserting a cloud within a tropical model atmosphere with monotonically increasing values of the integrated liquid water content. Five different cloud models were investigated. These included altocumulus, stratocumulus, stratus, nimbostratus, and cumulus. Additionally, two values of surface emissivity were used, 0.7 and 1.0, to simulate the ocean surface

and land, respectively. Here the potential effects of beam filling clouds on millimeter wave moisture retrieval accuracy are investigated and results obtained in cloudy conditions are compared with their clear sky counterparts.

2.5.1 Cloudy Moisture Sounder Channel Weighting Functions

The effects of cloud on the optical properties of the atmosphere for the millimeter wave sounder channel frequencies were assessed by evaluating sensor weighting functions. These calculations were performed both with and without cloud so that the cloud effect could be quantified. Profiles of atmospheric absorption coefficients, $k(\nu, p)$, for each frequency of interest were calculated using the RADTRAN simulation algorithm (Falcone et al., 1982). These provided the transmission profiles (Eqns. 2.2 and 2.3) necessary to evaluate the weighting function which was defined as the change of transmittance with height in the atmosphere with unit transmittance taken at the top of the atmosphere (in the case of this calculation, at 40 km). The channel set selected consisted of the five frequencies corresponding to those of the DMSP SSM/T-2 moisture sounder. These frequencies and the design noise equivalent brightness temperatures (NEAT's) for the SSM/T-2 are given in Table 2-1. To simulate sensor and scene noise for retrieval studies, a random signal of 1K (Gaussian distribution with zero mean) was added to each simulated brightness temperature. To simulate the effect of cloud within the field-of-view of the radiometer a suitable set of cloud models was incorporated within the evaluation of atmospheric attenuation profiles. The cloud models chosen were taken from the AFGL FASCODE model (Falcone et al., 1979). Cloud attenuation, $\alpha(\nu, T, z)$, was calculated using a simple relationship (Staelin, 1966) between cloud liquid water content LWC and a frequency and temperature dependent proportionality constant $f(\nu, T)$ dependent on cloud index of refraction.

$$\alpha(\nu, T, z) = f(\nu, T) \cdot \text{LWC}(z) \quad (2.16)$$

Index of refraction data for water are from (Ray, 1972) while those for ice are from (Warren, 1983). Cloud liquid water content and vertical extent for the five cloud models chosen from (Falcone et al., 1979) are given in Table 2-12.

Table 2-12. Cloud Types, Liquid Water Contents, and Vertical Extents Used in Cloudy Brightness Temperature Simulations

| Type | Liquid Water Content (gm^{-3}) | Vertical Extent (km) |
|------------------|--|-------------------------|
| 1. Stratus | 0.15 | 0.5 - 2.0 |
| 2. Cumulus | 1.00 | 1.0 - 3.5 |
| 3. Altostratus | 0.40 | 2.5 - 3.0 |
| 4. Stratocumulus | 0.55 | 0.5 - 1.0 |
| 5. Nimbostratus | 0.61 | 0.5 - 2.5 |

The effect of an altostratus cloud (model 3) on the profiles of atmospheric optical properties at these millimeter wave frequencies is illustrated in Figures 2-6 through 2-11. Plotted are the weighting functions ($-\frac{\partial r}{\partial z}$) for six model atmospheres for the channel frequencies given in Table 2-1 both without (a) and with (b) an altostratus cloud in the field-of-view. The six model atmospheres are: (1) U. S. standard, (2) tropical, (3) mid-latitude summer, (4) mid-latitude winter, (5) sub-arctic summer, and (6) sub-arctic winter. The weighting function indicates the relative contribution of each atmospheric level to the brightness temperature at a given frequency. It can be seen from these figures that the cloud seriously restricts the sensor's ability to "sound" the atmosphere by constraining brightness temperature contributions to levels in the vicinity of the cloud (2.5 - 3.0 km for the altostratus cloud).

Figures 2-6a through 2-11a provide a useful comparison of the effect of model atmosphere on the SSM/T-2 weighting functions. The change in height distribution of each channel with temperature and water vapor profile can be quite drastic. As an example, compare the location of the peak of the 183.31 \pm 3 GHz channel weighting function (labeled as 180) for tropical (Fig. 2-7a) and midlatitude winter (Fig. 2-9a) atmospheres. The peak shifts

from 7.5 km for the tropical atmosphere to 4.5 for the midlatitude primarily due to the change in water vapor amount. Similar behavior can be noted for the other channels.

Significantly, the effect of the cloud layer on the weighting functions is apparent from Figures 2-6b through 2-11b. Since the product of the weighting function and the temperature profile determine the contribution of each atmospheric level to the brightness temperature at a given frequency, the highly cloud peaked weighting function suggests an important impact on the SSM/T-2 channels due to clouds. These figures provide an indication of which channels will be affected by clouds at various altitudes. Due to the shift of weighting functions with the model atmosphere noted above, the number of affected channels will change. For example, since channels peak higher in the tropics they will be least impacted by low cloud with the converse being true at higher latitudes where integrated water vapor amounts are less.

2.5.2 Brightness Temperature Simulations

Here we investigate the effect of cloud liquid water on brightness temperatures. The brightness temperatures were evaluated from Eqn. (2.1) using a radiosonde ensemble corresponding to either a midlatitude or tropical sounding over both land and ocean surfaces. Surface temperatures, T_s , for each simulation were assumed equal to the radiosonde temperature at 1000 mb which was taken as the surface pressure, p_s . Two values of surface emissivity, ϵ_s , were used: one for land backgrounds (1.0) and one for oceanic backgrounds (0.7). Clear air attenuation due to absorbing gases was evaluated using RADTRAN as described in the previous section. Clouds were incorporated into the brightness temperature simulation process by randomly selecting from among one of the cloud types in Table 2-12. Cloud attenuation calculated from Eqn. 2.16 was then added to the clear sky absorption for each atmospheric layer within the vertical domain specified for the selected cloud type model. It was assumed that all cloud types were equally probable, completely filled the field-of-view, and that only a single cloud layer was present. The second assumption tends to overestimate cloud impact, while the last results in an underestimate. Since the profiles of temperature and water vapor were given at constant pressure levels rather than at constant heights as are the cloud

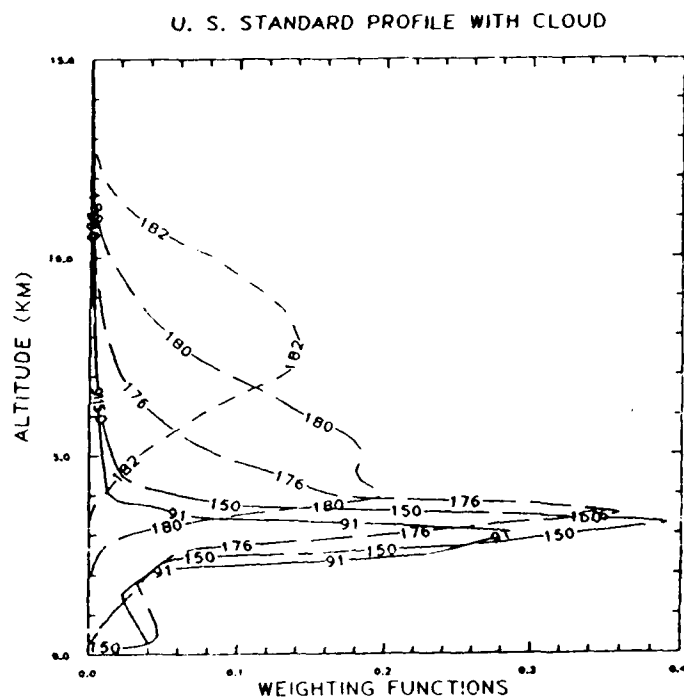
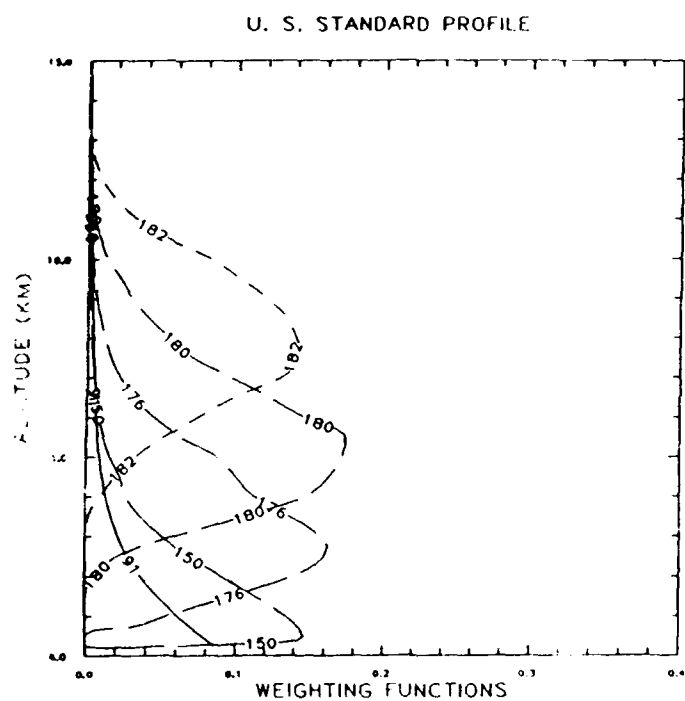


Figure 2-6. SSM/T-2 weighting functions for U.S. standard profile:
(a) clear, (b) cloudy.

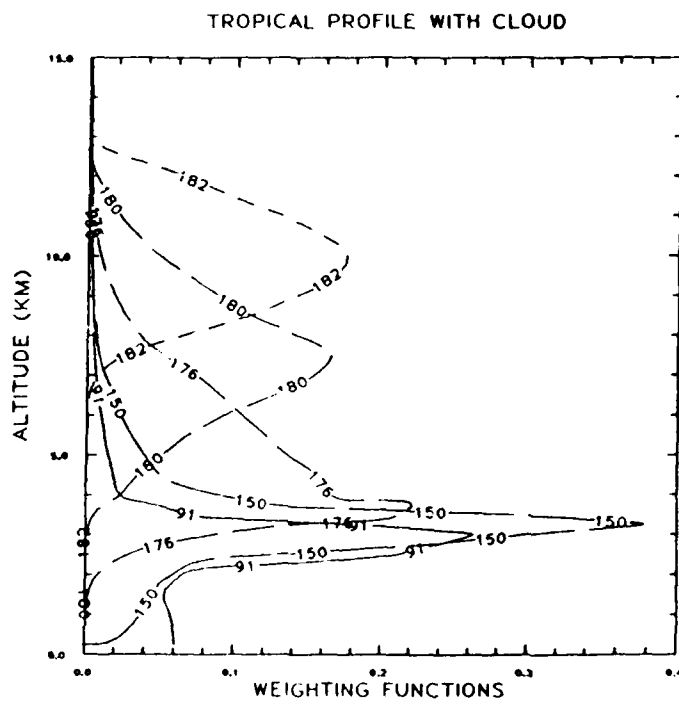
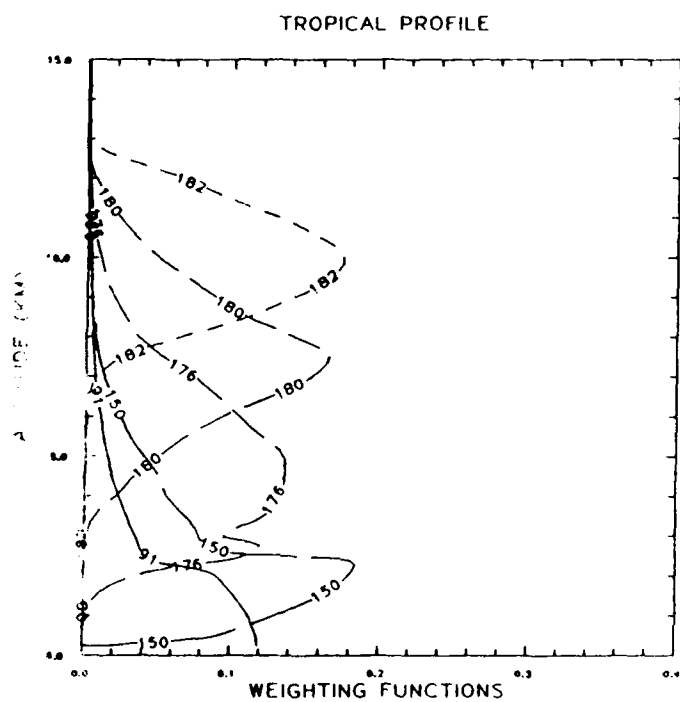


Figure 2-7. SSM/T-2 weighting functions for tropical profile: (a) clear,
(b) cloudy.

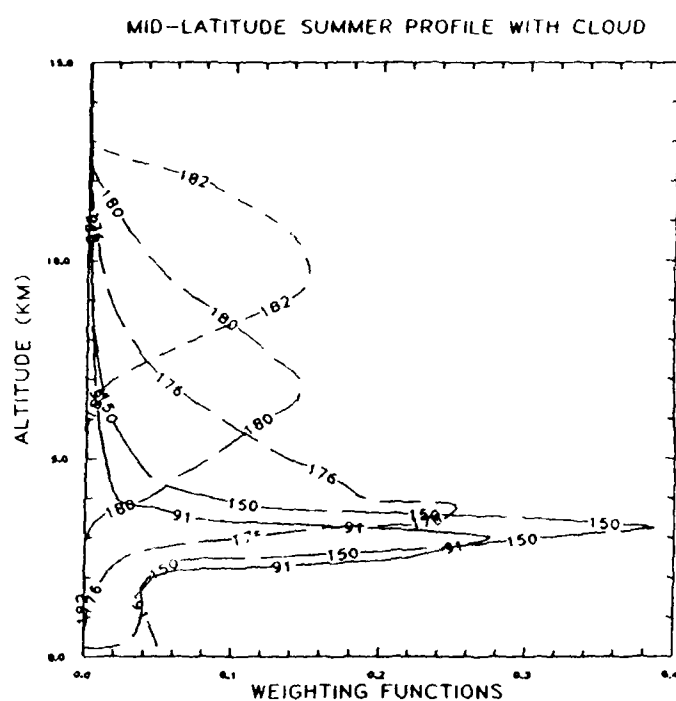
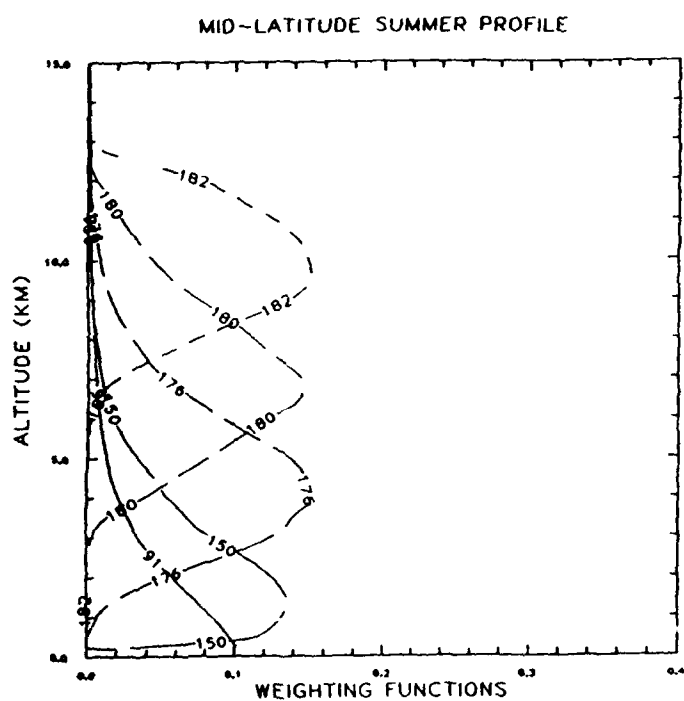


Figure 2-8. SSM/T-2 weighting functions for midlatitude summer profile:
(a) clear, (b) cloudy.

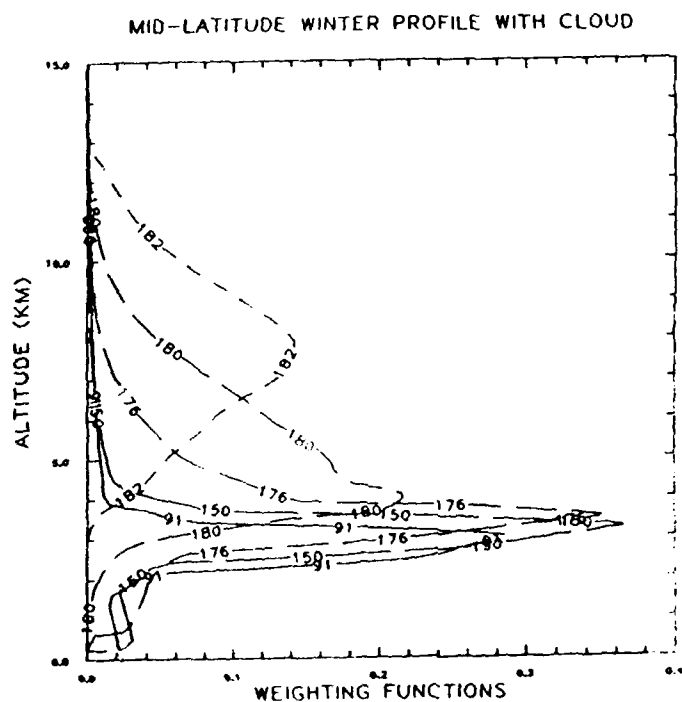
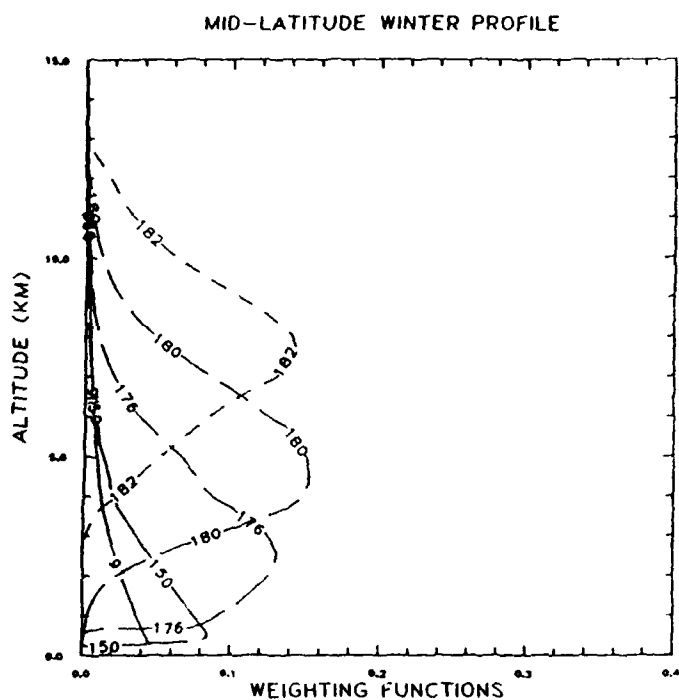


Figure 2-9. SSM/T-2 weighting functions for midlatitude winter profile:
(a) clear, (b) cloudy.

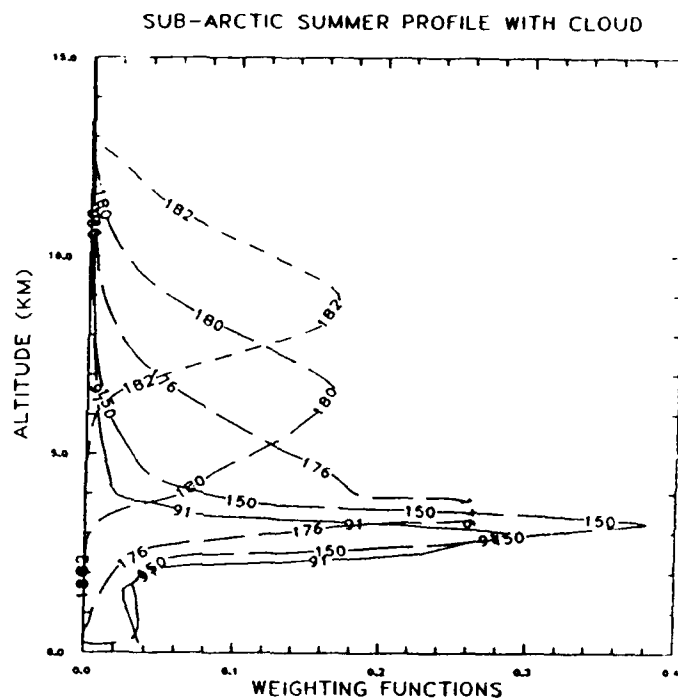
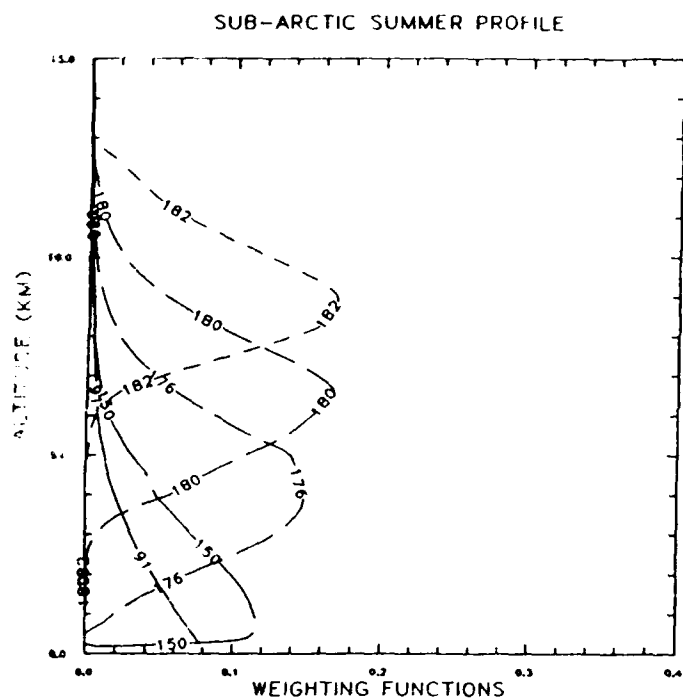


Figure 2-10. SSM/T-2 weighting functions for subarctic summer profile:
(a) clear, (b) cloudy.

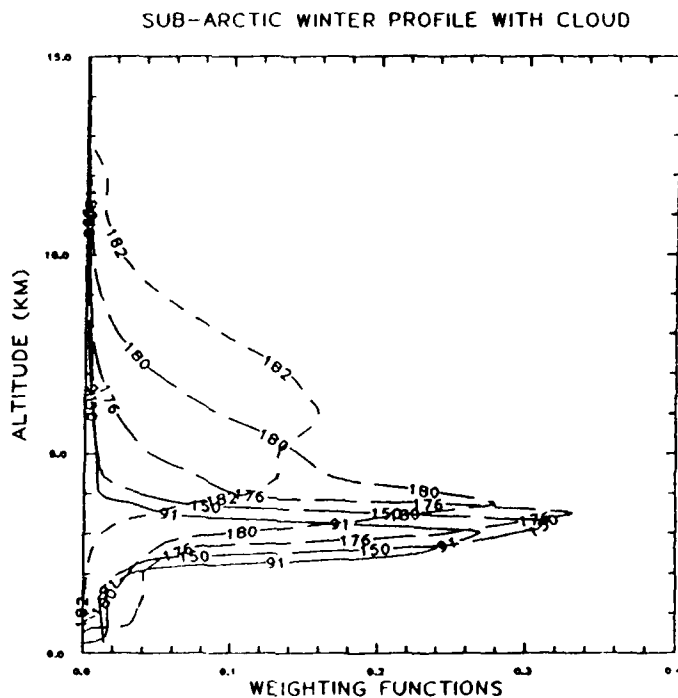
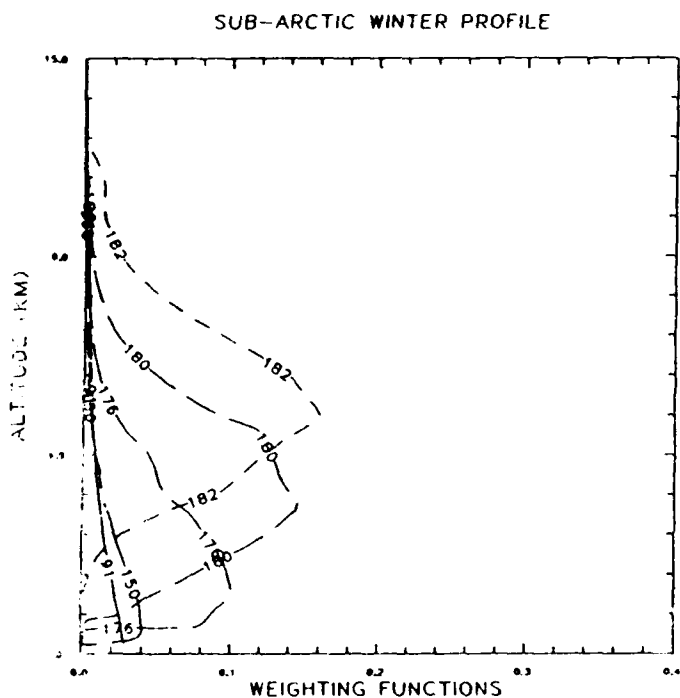


Figure 2-11. SSM/T-2 weighting functions for subarctic winter profile:
(a) clear, (b) cloudy.

models, cloud vertical extent had to be interpolated to the appropriate pressure level within individual profiles. Within cloudy layers relative humidity was not adjusted to saturation. For the tropical atmospheric retrievals reported, requiring saturation within individual model layers had little effect on retrieval results.

The impact of this cloud effect on calculated brightness temperatures is illustrated in Figures 2-12 through 2-16. Each figure is annotated by cloud model and surface emissivity (ocean, a, and land, b). Plotted is channel brightness temperature vs. integrated liquid water content. The dashed lines correspond to the dependence of each channel's response to changes in liquid water content for the particular cloud chosen. A solid horizontal line appears in each figure. This corresponds to a brightness temperature equivalent to the physical emission temperature of the cloud top. This is the temperature which would be sensed by an infrared radiometer, i.e., that corresponding to an optically thick cloud. The cloud top temperature is in the upper left hand corner of each figure.

Examining these results, a number of themes emerge:

- (a) For low clouds, the 183 GHz channels are virtually unaffected by increases in cloud liquid water. This is apparent from the flat line behavior of the 184.32, 186.31, and 190.31 GHz curves. This does not mean that there is no cloud impact on the water vapor retrieval, however.
- (b) Although the 183 GHz channels are unaffected, the window channels at 90 and 150 GHz do respond to the cloud water presence. Water vapor retrieval accuracy is highly dependent on these channels. The 90 GHz channel is more sensitive to cloud than the 150 GHz channel.
- (c) It is interesting to compare the figures for the same cloud type with different backgrounds, i.e., land vs. ocean. There is virtually no difference in the signatures of the 183 GHz channels since they do not see the surface. The 90 and 150 GHz channels differ considerably depending on background. Over the ocean these channels are cold (the surface temperature is about 300 K). Over land it is a few degrees cooler than the surface temperature due to water vapor effects. The presence of the

cloud introduces a relatively warm emission source over the ocean and a somewhat cooler one (due to its altitude over the land). Thus increasing integrated cloud liquid water warms the signal at 90 GHz over the ocean and cools it over land. Over land, behavior is the same as that in the infrared region except that the cloud is not opaque.

- (d) Sensitivity to cloud presence is a function of cloud top altitude, optical thickness (here cloud liquid water content), and the underlying surface. Over the ocean, lower clouds are more detectable, since they are warmer. Over land, higher clouds are more detectable. Lower clouds look radiometrically like the surface (as they do in the infrared).
- (e) As the cloud liquid water content increases, the brightness temperatures at 90 and 150 GHz asymptote to the cloud top temperature. Thus with sufficient water content, the window channel signals should provide an indication of cloud top height.
- (f) For higher clouds (see the cumulus cloud model result), a response from the 183 GHz channels is evident. This is manifested as a cooling, as the cloud blocks emission from warmer levels below the cloud top. The cumulus cloud quickly becomes optically thick. Over the ocean, the brightness temperature at 90 GHz quickly saturates and then begins to cool. These curves resemble brightness temperature vs. rainfall rate relationships at lower frequencies.

In summary, these calculations indicate that cloud affects millimeter wave sensor channels and that there is potentially information on cloud presence and height in the brightness temperature data obtainable from the millimeter wave moisture channels.

2.5.3 Water Vapor Profile Retrievals in the Presence of Clouds

Vertical moisture profile retrievals were obtained from independent samples of simulated sensor brightness temperatures using a statistical inversion technique (Rodgers, 1976; Gaut et al., 1975). The essential element of the scheme is to choose, in a statistical sense, the most probable combination of

atmospheric and surface properties which produces the set of measured radiometric data values. It is a general regression technique which minimizes the mean square error between the estimated and observed values of the parameter of interest. Here the desired parameters are the absolute abundance of water vapor (molecules cm^{-2}) in six layers corresponding to 0-200, 200-300, 300-500, 500-700 mb, and 850-1000 mb, respectively. Parameter and resultant data vector ensembles are divided into two groups, designated A and B, corresponding to a priori and retrieval subsets, respectively. Water vapor profiles are retrieved from the B data vectors based on statistics developed from the a priori A set. An estimate of the parameter vector p is obtained from the simulated data vector ϕ , [i.e. the channel, brightness temperatures $T_b(\nu)$] from:

$$p = D \cdot \phi, \quad (2.17)$$

where the D-matrix is computed from the a priori parameter/data vector ensemble A using:

$$D = C(p, \phi) C^{-1}(\phi, \phi) \quad (2.18)$$

where p is the parameter vector from the a priori set, ϕ is a generalized data basis function defined as

$$\phi = \text{column} \left[1, \frac{d_1 - \langle d_1 \rangle}{\langle d_1 \rangle}, \dots, \frac{d_m - \langle d_m \rangle}{\langle d_m \rangle} \right] \quad (2.19)$$

for m channel radiometric data d in the dependent set A (d_i , $i = 1, \dots, m$), the brackets denote the mean value operator, and $C(\phi, \phi)$ and $C(p, \phi)$ are the diagonalized autocorrelation and crosscorrelation matrices of (ϕ, ϕ) and (p, ϕ) respectively. For the SSM/T-2 channel set specified in Table 2-1, $m=5$. The effect of cloud on water vapor profile retrieval accuracy is assessed by including cloud in the data vector simulation. Independent retrieval statistics were then evaluated for clear and cloudy situations. Thus, clear cases are retrieved using a "clear" D matrix and cloudy cases using a "cloudy" D matrix. This approach avoids the application of nonrepresentative statistics for either clear or cloudy cases. It should be noted, however, that in prac-

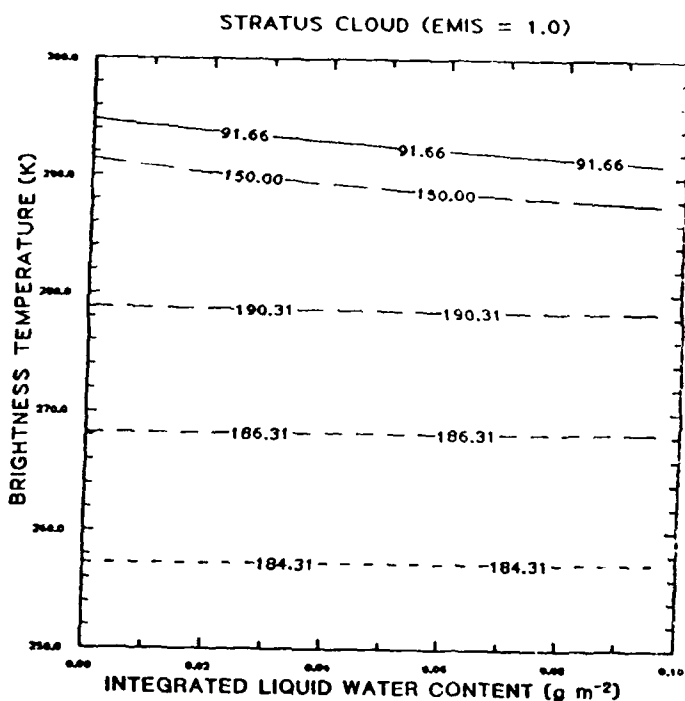
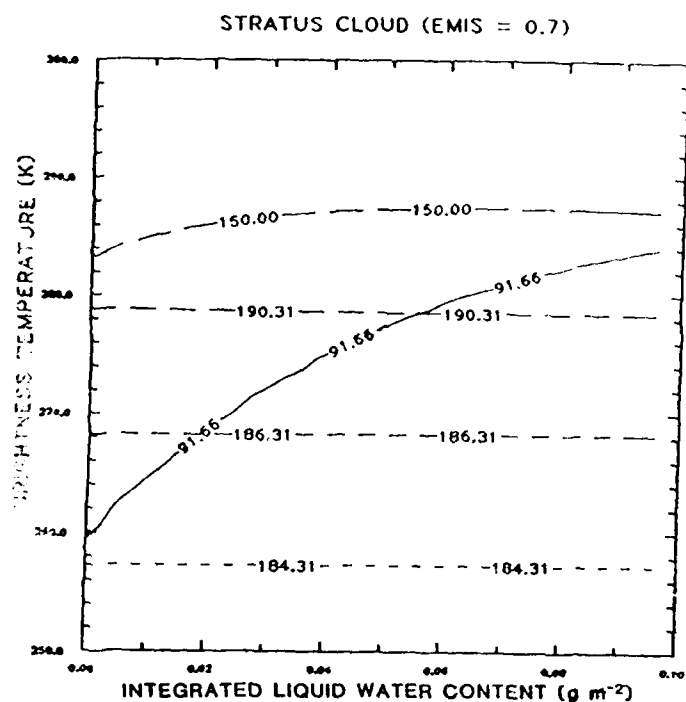


Figure 2-12. Brightness temperature (K) versus integrated liquid water content (g/cm^{-2}) over: (a) ocean and (b) land for stratus cloud.

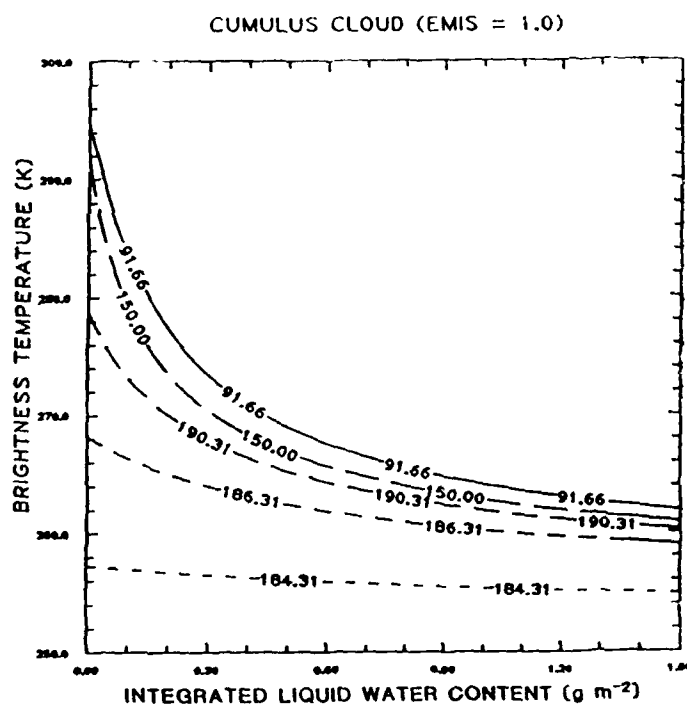
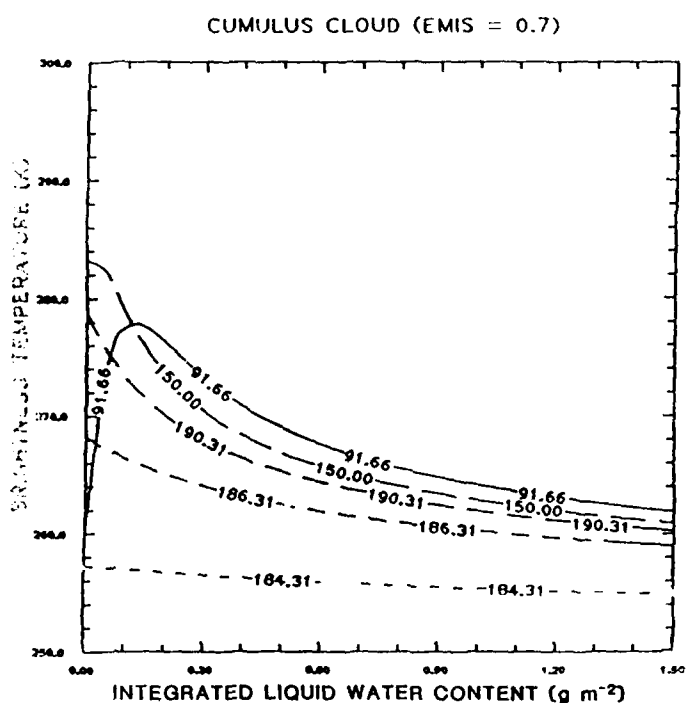


Figure 2-13. Brightness temperature (K) versus integrated liquid water content (g/cm^{-2}) over: (a) ocean and (b) land for cumulus cloud.

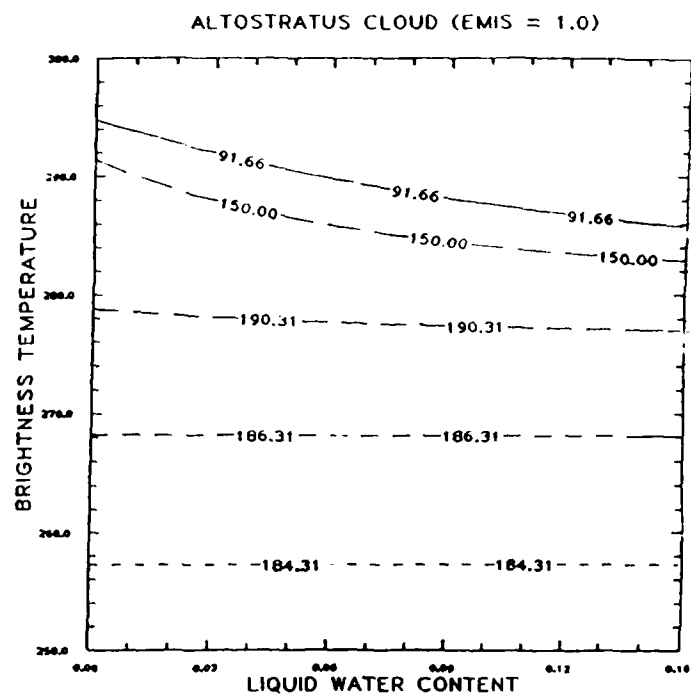
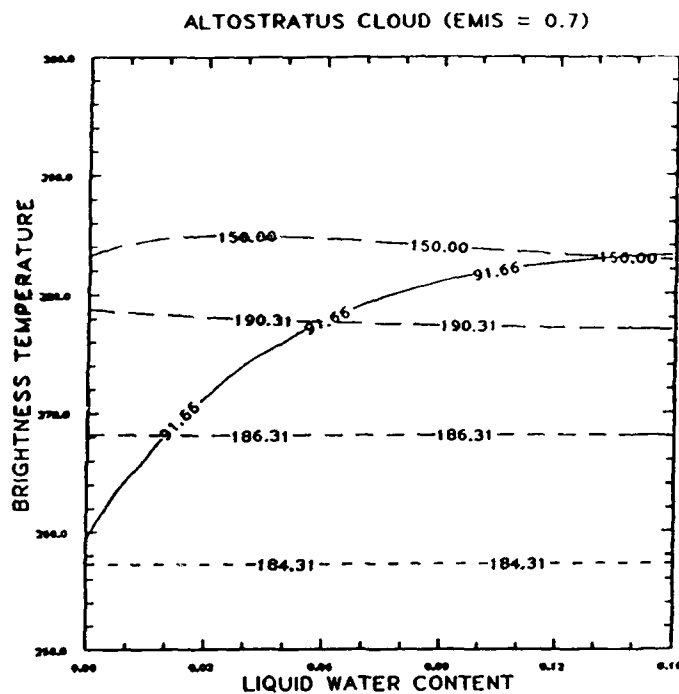


Figure 2-14. Brightness temperature (K) versus integrated liquid water content (g/cm^2) over: (a) ocean and (b) land for altostratus cloud.

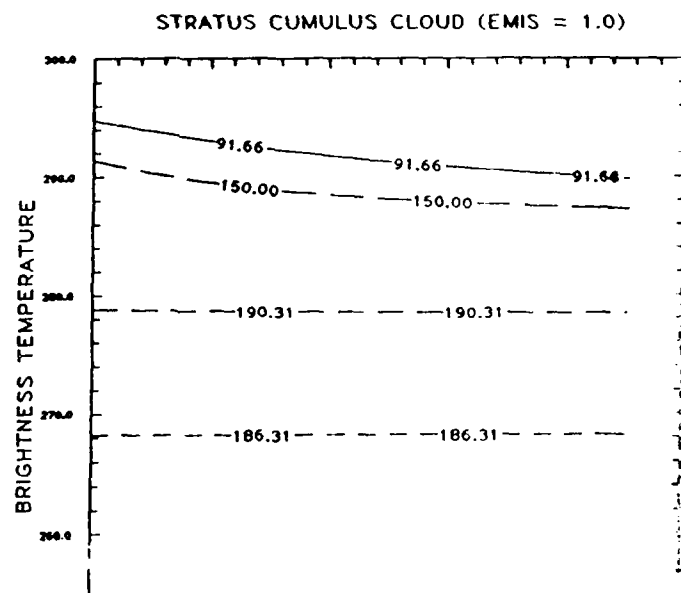
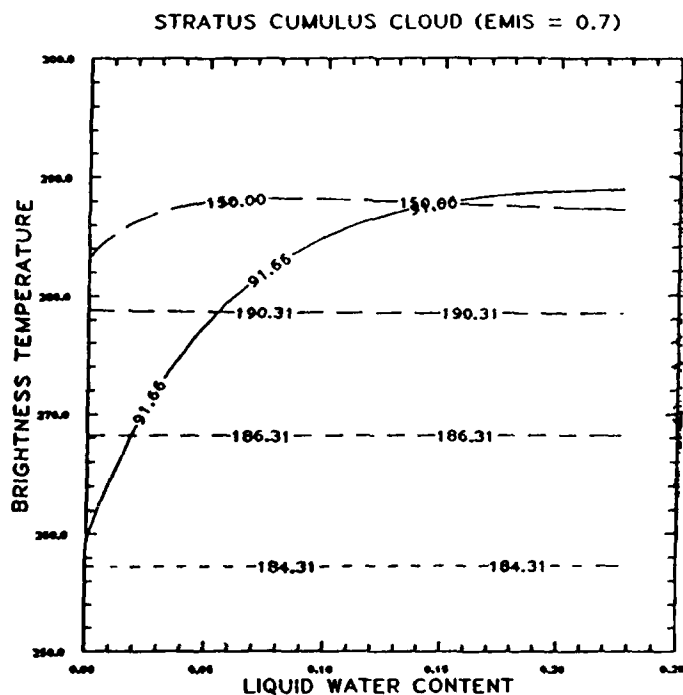


Figure 2-15. Brightness temperature (K) versus integrated liquid water content (g/cm^2) over: (a) ocean and (b) land for stratocumulus cloud.

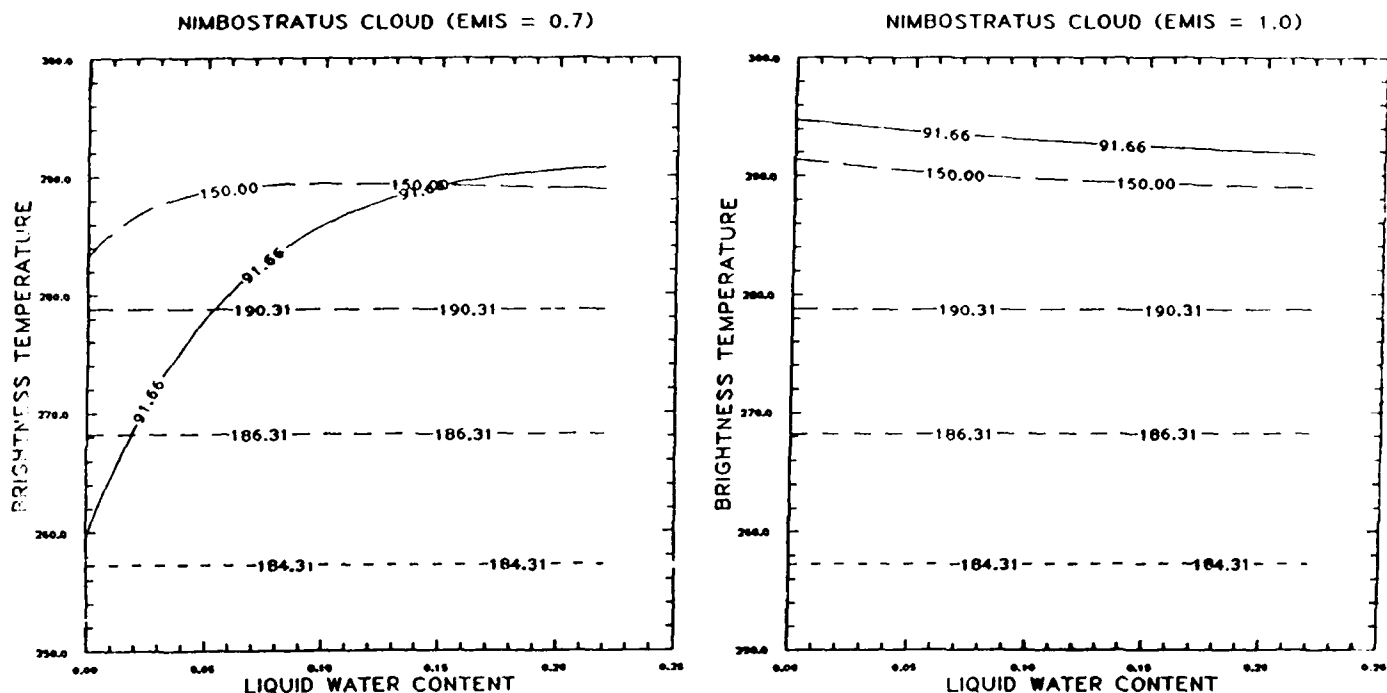


Figure 2-16. Brightness temperature (K) versus integrated liquid water content (g/cm^2) over: (a) ocean and (b) land for nimbostratus cloud.

tice it may not always be possible to identify clear and cloudy cases from the data itself. Retrieval accuracy was assessed by comparing inferred layer water vapor abundances to those in the actual profiles (i.e. those used in the B set simulations) and then evaluating the fractional root mean square (RMS) error over the ensemble of retrievals. The RMS fractional error for each layer k evaluated for the set of $N = 100$ independent soundings was defined as:

$$\text{RMS}(k) = \frac{1}{\langle u(k) \rangle} N^{-1} \left\{ \sum_{j=1}^N [u(k,j) - \langle u(k) \rangle]^2 \right\}^{1/2}, \quad (2.20)$$

where $u(k,j)$ and $\langle u(k) \rangle$ are the retrieved and actual water vapor amounts for the k^{th} layer and j^{th} sounding, respectively, and $\langle u(k) \rangle$ is the layer mean value. For comparison, the same statistic was evaluated assuming the mean of the ensemble retrieval for each sounding, i.e. by replacing u by $\langle u \rangle$ itself. This provides a measure of the RMS fractional error obtained when only climatological mean estimates are available.

A comparison of statistical water vapor profile retrieval results for clear and cloudy cases is illustrated in Figures 2-17 and 2-18. Plotted are layer fractional RMS errors as a function of mean layer pressure for clear and cloudy tropical soundings over oceanic (Figure 2-17) and land (Figure 2-18) backgrounds. Each figure also shows the RMS fractional error obtained when climatology (i.e. the layer mean value) is used in Eqn. (2.20) as the retrieved layer value. This result is related to the climatological variance of the sample and provides a measure of retrieval skill. The ratio of the retrieval RMS fractional error to that of the climatology curve in each figure is a measure of the remaining unexplained variance after the retrieval process. Thus small values of this ratio are deemed skillful retrievals and no skill is demonstrated as this ratio approaches unity.

It can be seen that the selected millimeter wave channel set should provide water vapor retrievals which are quite skillful in clear situations over ocean backgrounds, particularly in the middle troposphere. Over land, the retrievals are still skillful although improvement over climatology is not quite as distinctive. The enhanced retrieval skill over the low emissivity oceanic background can be extrapolated to other low emissivity surfaces such as dry snow which provide high contrast for atmospheric emission.

The clear atmosphere retrieval results can be contrasted with those obtained in cloudy situations. The fractional RMS error of the simulated retrievals over both oceanic and land backgrounds is increased considerably due to the presence of beam filling cloud. The effect is particularly noticeable over the oceans where the clear retrievals appear to be quite good. Notably, at upper tropospheric levels (pressures below about 600mb), cloudy retrieval accuracies are about the same, regardless of background. Thus it appears that the presence of an obscuring cloud over the ocean reduces the apparent advantage of millimeter wave sounding against the comparatively low emissivity ocean surface in clear situations.

While the retrieval approach adopted here to demonstrate the effect of clouds is quite simple, it is analogous to that proposed for operational implementation with SSM/T-2 millimeter wave sounder data (Stogryn, personal communication). Within the context of such statistical retrievals, the treatment of cloud is problematical. Given the potential degradation of water vapor profile retrievals due to cloud presence, a method which explicitly

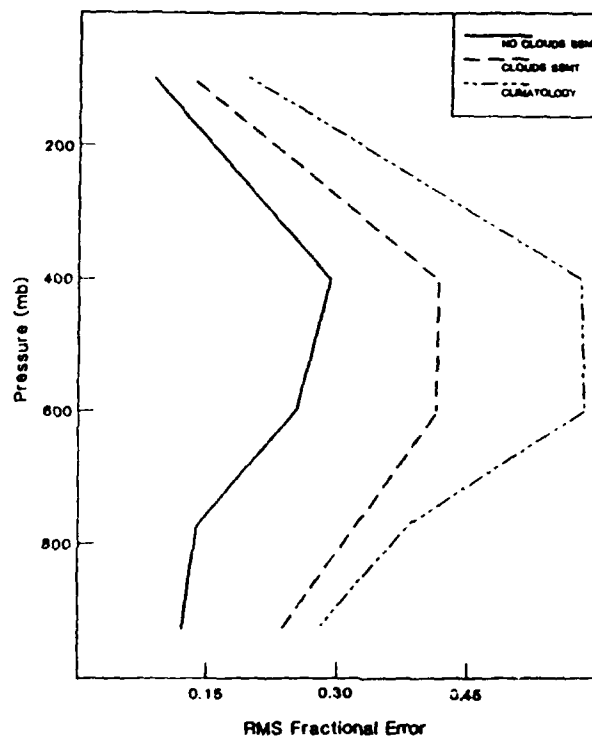


Figure 2-17. Water vapor retrieval RMS fractional errors for tropical, oceanic soundings with clear atmospheres (solid), cloudy atmospheres (dashed), and climatology (short dashes).

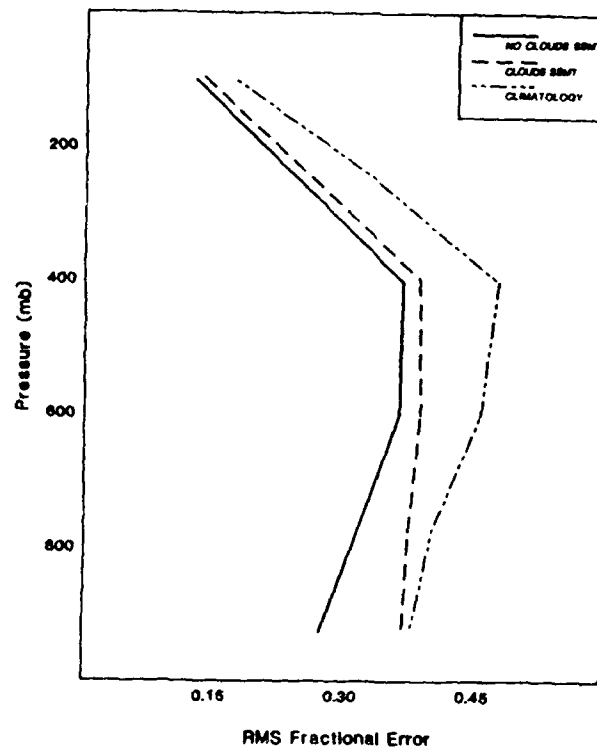


Figure 2-18. Water vapor retrieval RMS fractional errors for tropical land soundings with clear atmospheres (solid), cloudy atmospheres (dashed), and climatology (short dashes).

treats cloud within the retrieval algorithm may be usefully applied. Physically based approaches used for infrared sounder data may provide appropriate treatments.

2.6 A Unified Retrieval Methodology for the DMSP Meteorological Sensors

The potential for improving statistical retrievals of temperature and moisture profiles using a physical retrieval was demonstrated in Sections 2.3 and 2.4. In Section 2.5, the degradation of moisture retrieval results due to cloud presence was illustrated. Here we propose a method to incorporate all DMSP meteorological sensor data including that from the SSM/T, SSM/T-2, SSM/I, and OLS (see Table 2-1) into a unified retrieval.

2.6.1 Proposal Scheme

The unified retrieval approach for the DMSP illustrated in Figure 2-19 employs physical considerations and allows for the incorporation of all data sources. Recognizing potential operational constraints, an attempt has been made to build on the attributes of the existing DMSP retrieval capability and experience. The microwave sensor data, T_b^0 , is employed with the "D" matrix

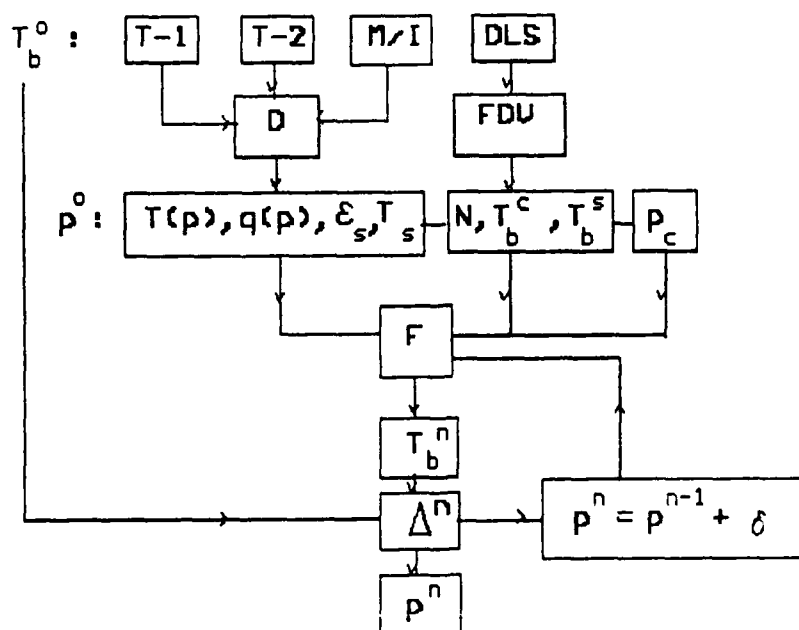


Figure 2-19. Schematic of unified DMSP retrieval scheme.

statistical retrieval to provide first guesses for the desired parameters, P^0 : temperature, $T(p)$, and water vapor profiles, $q(p)$, surface emissivity, ϵ_s , and temperature, T_s . Simulated brightness temperatures, T_b^n , are then evaluated to examine the consistency of the first guesses with the observations. The forward problem calculation (denoted by F in Fig. 2-19) is accomplished using the RADTRAN simulation code (Falcone et al, 1982) as modified by Isaacs et al (1985a). When the residuals, Δ^n , (i.e. differences between simulated and observed brightness temperatures) are small, the process terminates. However, when residuals are larger than a preset tolerance (usually determined by the sensor noise equivalent brightness temperatures (NE Δ T) and scene noise), the procedure goes on to adjust the first guess profiles. This adjustment is accomplished by using the residuals in a simultaneous physical retrieval.

Cloud or precipitation in the field-of-view (FOV) of the microwave sensors can be problematic. Precipitation will generally preclude soundings of temperature and moisture and the determination of surface properties. Quality control flags for precipitation (as well as precipitation amounts) can be obtained from the SSM/I statistical retrieval (Lo, 1983; Jin and Isaacs, 1987). Isaacs and Deblonde (1987) have discussed the potential impact of cloud on statistical millimeter wave water vapor retrievals and evaluated the sensitivity of these channels to cloud presence. Cloud fields from the DMSP OLS (using an appropriately spatially averaged subset of visible and infrared imagery) aid in cloud/no cloud discrimination. To determine first guess cloud properties within the FOV necessary to accomplish the physical retrieval step, the high spatial resolution OLS imager data is utilized. Image processing of this data within the relatively larger microwave footprint provides first guess cloud coverage, N , and equivalent brightness temperatures (EBTs) for cloud top and surface, $T_b^{c,s}$. Cloud top brightness temperature along with the first guess temperature profile yields a first guess cloud top pressure, p_c . Over the oceans, cloud properties derived from the OLS imager data are supplemented by information on cloud integrated liquid water content (ILWC) available from the SSM/I. Cloud ILWC provides a parameterization of cloud optical thickness and emissivity. These cloud properties are required to treat the effect of cloud on the SSM/T-2 sensor data and therefore are input to the forward problem.

2.6.2 Processing of OLS Imagery Data for Cloud Property Retrieval

In cloudy areas, cloud coverage and cloud top height first guesses are necessary for the physical retrieval step (Equation 2.1 is modified.) Co-located with the microwave sensors aboard the DMSP spacecraft, the Operational Linescan System (OLS) provides both visible and infrared imagery at high spatial resolution. With much higher spatial resolution, the visible and infrared data from the OLS imagery can be used to characterize the uniformity of the much larger microwave footprints. In those areas where the contributions from the atmosphere to microwave brightness temperature are small (i.e., nonprecipitating situations), visible or infrared data is able to provide guidelines on the uniformity of the surface observed within a field-of-view. When clouds obscure portions of the microwave field-of-view, the imager data provides the complementary capability of cloud property determination.

Classically, techniques to infer FOV non-uniformity have been referred to as texture analysis methods. A number of approaches can be used for texture analysis including: (a) examination of the spatial power spectrum of an image through Fourier decomposition, (b) edge enhancement, and (c) spatial coherence. We have chosen the spatial coherence approach (Coakley and Bretherton, 1982) for the determination of both cloud and surface properties from OLS data. The statistics evaluated are the local mean (\bar{I}) and local standard deviation (LSD) of radiance (or gray shade) values. The LSD is calculated for $n \times n$ sets of pixels.

A plot of LSD_k vs. \bar{I}_k gives the cloud coverage fraction within the microwave footprint and the EBT of the surface and effective cloud top. Figures 2-20a,b illustrate LSD_k vs. \bar{I}_k frequency plots for a partially cloudy microwave FOV over the ocean evaluated using GOES visible and infrared imagery. The spike in the visible result (Fig. 2-20a) denotes the surface reflectance value due to clear visible pixels. The higher reflectivity, signatures with nonzero standard deviation result from partially cloudy pixels. In the infrared data (Fig. 2-20b), the highest and lowest EBTs correspond to the surface and cloud

top emission, respectively. The cloud top EBT is used with the first guess temperature profile to obtain the first guess effective cloud top pressure, P_c .

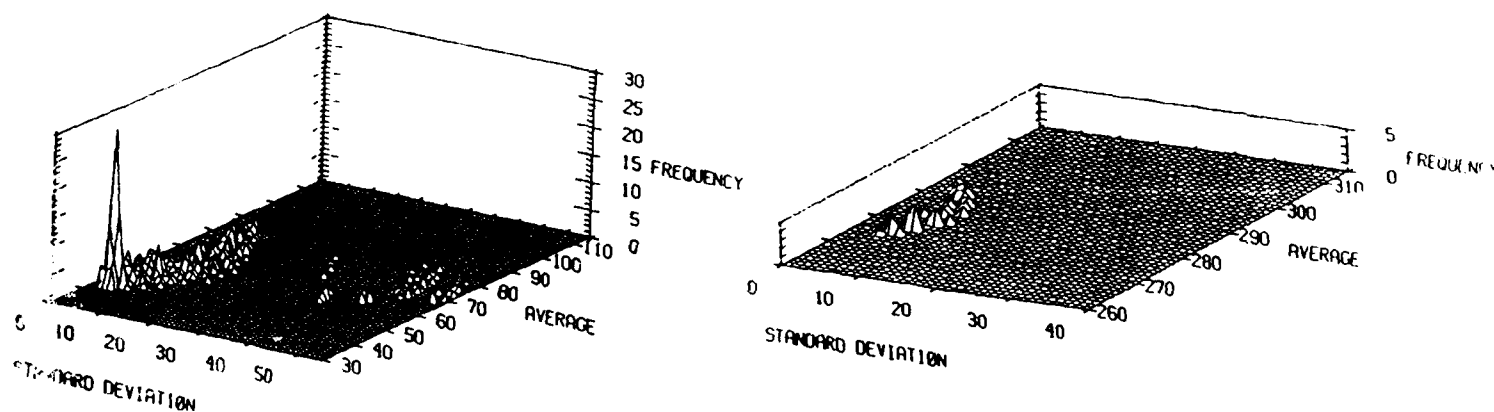


Figure 2-20. Spatial coherence results for partially cloudy microwave field-of-view using: (a) visible and (b) infrared GOES imager data.

3. TASK 2 - SIMULATION MODEL ENHANCEMENTS

Four subtasks were completed during the first year's effort to enhance the simulation model performance. These are described in this section.

3.1 Multiple Scattering

The multiple scattering submodel to treat large cloud droplets and liquid and glaciated precipitation used in the Phase I effort was based on the discrete ordinate method as described by Liou (1973) and Liou et al. (1980). In this approach the scalar radiative transfer equation for brightness temperature within the scattering cloud is reduced by Gaussian quadrature of degree n

(in fact the method is referred to in some circles as the Gaussian quadrature method) to a set of $2n$ coupled differential equations:

$$u_i \frac{dT_i(\tau)}{d\tau} = T_i(\tau) - \sum_{j=1}^n (C_{i,-j} T_{-j} + C_{i,j} T_j) - (1-w) T \quad (3.1)$$

where T_i is the brightness temperature at the i th Gauss zenith angle cosine u and:

$$C_{i,j} = \frac{1}{2} \sum_{l=0}^{2n+1} a_j (2l+1) w_l P_l(\mu_i) P_l(\mu_j) \quad (3.2)$$

In the expression above, the w_l 's are coefficients of the Legendre polynomial expansion of the phase function and the a_j are the Gaussian quadrature weights ($a_j = a_{-j}$; $\mu_j = -\mu_{-j}$). The solution for each T_i is given by:

$$T_i = \sum_{j=-n}^n L_j g_j(u_j) \exp(-k_j \tau) + T_c \quad (3.3)$$

where the g_j and the k_j are the eigenvectors and eigenvalues of the system of equations, respectively, and T_c is the cloud temperature. The L_j 's are constants determined by the boundary conditions of the problem.

Liou (1973) originally discussed a variety of numerical stability problems associated with his application of the polynomial root searching method and subsequent evaluation of the corresponding eigenvectors. This method was also implemented within the microwave program supplied to AFGL (Liou et al., 1980). We implemented a new method to evaluate eigenvalues and eigenvectors based on available, standardized algebraic eigensolution methods. The advantage of these approaches is that they increase accuracy and decrease the time required to find the solutions to these systems of equations. This approach has already been tried to solve analogous equations for the scattering of solar radiation (Stamnes and Swanson, 1981; Stamnes and Conklin, 1984) using algorithms available from the IMSL (1975) library.

This approach was implemented within the discrete ordinate multiple scattering code for thermal radiation using matrix eigensystem routines from the EISPACK (Smith et al., 1975) program set available on AER's Harris H800 computer. Table 3-1 compares the eigenvalues obtained using both Liou's root searching method and the EISPACK code. These were generated for a case treating the evaluation of brightness temperatures at 50.5 GHz looking at a rain-

rate of 5 mm/h using 16 streams (eight up and eight down). Both positive and negative eigenvalues are used for a total of 16 roots. The root searching calculations had to be performed in quad precision on the Harris (approximately double precision on other machines) in order to insure convergence. By using the EISPACK eigensystem solution in place of the root searching methods, accuracies were matched and exceeded and a time saving of about a factor of ten was realized in the section of the discrete ordinate code which evaluated the eigenvalues and eigenvectors.

Aside from the method of eigensystem solution this code operates identically to and has the same restrictions as that used in the Phase I study. For example, it does not treat polarization (see section 3.3) and looks only at nadir. Additionally, the code must be run along with the attachment of appropriate subroutines from the EISPACK library.

Table 3-1. Comparison of Eigenvalues From Liou's Root Searching Method for the Discrete Ordinate Method and those from the EISPACK Routines

| Eigenvector # | Liou | EISPACK |
|---------------|-------|-----------|
| 1 | 0.948 | 0.947994 |
| 2 | 1.030 | 1.029818 |
| 3 | 1.116 | 1.116219 |
| 4 | 1.274 | 1.273931 |
| 5 | 1.552 | 1.552476 |
| 6 | 2.089 | 2.088644 |
| 7 | 3.390 | 3.389966 |
| 8 | 10.04 | 10.036796 |

3.2 Mie Scattering Parameters

The discrete ordinate code discussed in the previous section requires, among its various inputs, the Mie scattering parameters for the particular frequency and rainfall droplet size distribution desired. Unfortunately, this data is not calculated on-line with the program and must be supplied by the

user. In order to circumvent this inconvenience, a subroutine was written which provided the necessary input data on line with specification of a few simple meteorological parameter inputs such as rainfall rate, desired size distribution (Marshall-Palmer or Best), and phase of the precipitation (i.e., water or ice). This parameterization is based on the published values of Savage (1978) and is briefly discussed below and in Isaacs et al. (1988a). The algorithm is valid between the frequencies of 19.35 and 230 GHz and for the temperature range between 263 and 283 K. An algorithm suitable for completing exact Mie theory calculations is also described.

3.2.1 Precipitation Scattering Property Parameterization

The RADTRAN computer code (Falcone et al., 1982) was developed by the Air Force Geophysics Laboratory (AFGL) to provide atmospheric attenuation and brightness temperature calculations for typical atmospheric paths over the frequency range from 1 to 300 GHz. RADTRAN provides a design tool which can readily be used to assess potential environmental impacts on microwave and millimeter wave sensors. The atmospheric attenuation submodels of the clear atmosphere, fog, cloud, and rain used in RADTRAN have been thoroughly documented (Falcone et al., 1979). The models for fog, cloud, and rain attenuation have also been incorporated into the commonly used FASCODE accelerated line-by-line code (Clough et al., 1986). These codes can be used directly to evaluate atmospheric brightness temperatures in the absence of significant contributions to path radiance due to multiple scattering. This is generally the case for non-precipitating environments.

When precipitation is present, however, evaluation of the multiply scattered brightness temperature field requires both a generalization of the radiance solution and appropriate supplementary data on precipitation scattering properties. To generalize the radiance solution, the multiple scattering version of RADTRAN uses a numerical, Gaussian quadrature approach to the radiative transfer equation (Jin and Isaacs, 1985). The FASCODE approach is based on an approximation of the multiple scattering source function (Isaacs et al., 1987). Both treatments require the specification of precipitation scattering optical properties including the extinction coefficient (km^{-1}), single scattering albedo, and the angular scattering function. These data are not currently implemented within RADTRAN and must be supplied by the user.

Precipitation scattering properties are generally available via standard Mie theory calculations. The Mie theory formalism requires a knowledge of particle size distribution and index of refraction (Falcone et al., 1979). The index of refraction, in turn, is dependent on frequency, phase (i.e. ice or water), and temperature. To avoid the cumbersome necessity of performing on-line Mie theory calculations to support each possible combination of these model variables within multiple scenario brightness temperature simulations, a parameterization has been developed based on the existing Mie theory calculations of Savage (Savage, 1978). This parameterization is available for implementation within both RADTRAN and FASCODE.

The resultant subroutine provides an efficient method to obtain the extinction coefficient, single scattering albedo, and angular scattering function over the frequency domain from 19 to 240 GHz. The angular scattering function is given in terms of its first eight Legendre polynomial expansion coefficients. Precipitation angular scattering functions are not highly anisotropic at microwave frequencies and this number of terms usually suffices to describe them. Furthermore, this number of terms is consistent with the Gaussian quadrature required to specify the brightness temperature field (Jin and Isaacs, 1985; Savage, 1978). The scattering function asymmetry factor used in the FASCODE multiple scattering approximation is easily obtained from a knowledge of the second Legendre coefficient.

Input parameters to the subroutine consist of frequency (GHz), rainfall rate (mmhr^{-1}), temperature (deg C), phase (i.e. water or ice), and size distribution. The subroutine allows the user to choose either the Marshall-Palmer or Best size distribution (Savage, 1978). Details of the selected size distribution are varied with rainfall rate; higher rainfall rates skewing the distributions to larger drop sizes. Various checks are made on the input data to insure internal consistency with the stored data domain. A binary search routine is executed and a simple interpolation is performed to provide desired scattering properties at intermediate temperatures and frequencies not covered by the internal data set.

We have compared scattering parameters obtained using this subroutine with the results of exact Mie theory calculations. Comparisons were done at millimeter wavelength since precipitation angular scattering functions are more pronounced at these frequencies and thus provides a worse case assess-

ment. Fig. 3-1 compares extinction coefficient (BEXT) and single scattering albedo (OMEGA0) calculated by the subroutine (lines) and exact Mie theory calculations (symbols) throughout the millimeter wave region from 89.5 to 183 GHz at two values of the rainfall rate (2 and 5 mmhr⁻¹). Fig. 2 illustrates much the same comparison at selected frequencies for the first eight Legendre polynomial coefficients of a Marshall-Palmer size distribution of rain drops with a rainfall rate of 5 mmhr⁻¹. In general the subroutine produces scattering properties quite comparable to the more computationally demanding exact Mie theory calculations.

To assess the accuracy of the precipitation scattering properties for RADTRAN brightness temperature simulations, calculations were performed using an exact Gaussian quadrature, numerical solution to the multiple scattering radiative transfer equation (Jin and Isaacs, 1985) using both exact Mie theory data and those obtained from the subroutine described above. Brightness temperature differences were at most one or two tenths of a degree over the frequency range from 89.5 to 183 GHz. This is less than the noise equivalent brightness temperature achievable by radiometers operating in this frequency range. The subroutine thus provides precipitation scattering properties which are of considerable practical value for brightness temperature simulation purposes.

When less accurate brightness temperature field simulations are adequate, considerable computer time can be saved by using an approximate multiple scattering approach. We have compared exact numerical results (Jin and Isaacs, 1985) and those obtained using the FASCODE multiple scattering approximation (Isaacs et al., 1987). The model consisted of a 3 km rain layer with rainfall rate of 15 mmhr⁻¹. Optical depths and single scattering albedos at 19.35 and 37 GHz were (0.91, 0.21) and (3.20, 0.39), respectively. The surface temperature was assumed to be 287.0 K and the rain layer was nonisothermal with a mean layer temperature of 271.0 K and temperature gradient of 19.5 K over the 3 km layer. Results of the comparison are illustrated in Fig. 3-3 as a function of viewing angle. Brightness temperature differences between exact (lines) and approximate (symbols) results are generally a few degrees except near the horizon (i.e. 90 degrees). This behavior is due to the multiple scattering approximation which is more accurate for angles near the zenith. Even at the horizon, the percent error for the 37 GHz case (Fig. 3-3b) is

about 5%. This is well within the 20% RMS error cited for the approximation (Isaacs et al., 1987).

This approach should efficiently provide the required microwave scattering properties of precipitation with sufficient accuracy to support brightness temperature simulation calculations such as those in the multiple scattering version of RADTRAN.

3.2.2 Exact Mie Scattering Algorithm

For situations not represented by the parameterization discussed above, it is necessary to perform the Mie theory calculations for the desired conditions to obtain the necessary input data for the discrete ordinate method multiple scattering code. Specifically, the data necessary are the extinction coefficient, the albedo of single scattering, and the angular scattering function. The angular scattering function is input as coefficients w_1 of the normalized Legendre polynomial series, i.e.:

$$p(\theta) = \sum_{l=1}^N w_l P_l(\theta) \quad (3.4)$$

where the P_l are the Legendre polynomials. The number of terms required is equal to the number of streams desired in the brightness temperature calculation. For example, a 16 stream calculation will require sixteen coefficients and yield a phase function with an accuracy of $N=16$ terms in the summation of equation 3.4.

In order to provide the capability to generate the required Mie parameters for arbitrary size distributions, temperatures, and updated complex index of refraction data, a set of computer codes has been modified to run on the AFGL Cyber. These codes called RAD1 and RAD2 are taken from the algorithms developed by Dave (1972). The first program, RAD1, calculates the optical parameters and coefficients of the Legendre series representing the scattering properties of a single spherical particle. The second program, RAD2, calculates the analogous properties for a chosen size distribution of particles. The size distribution can be chosen from among the discontinuous power law

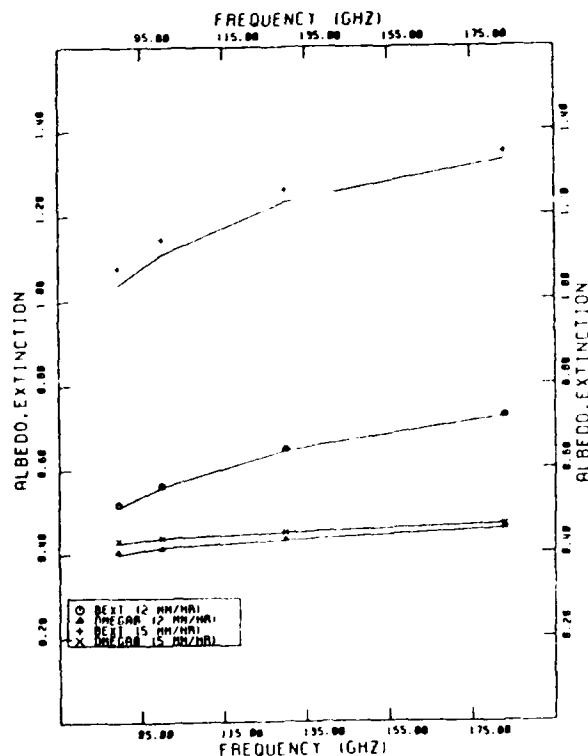


Fig. 3-1. Comparison of extinction coefficient (BEXT) and single scattering albedo (OMEGA0) calculated by the subroutine (lines) and exact Mie theory calculations (symbols) throughout the millimeter wave region from 89.5 to 183 GHz at two values of the rainfall rate (2 and 5 mmhr^{-1}).

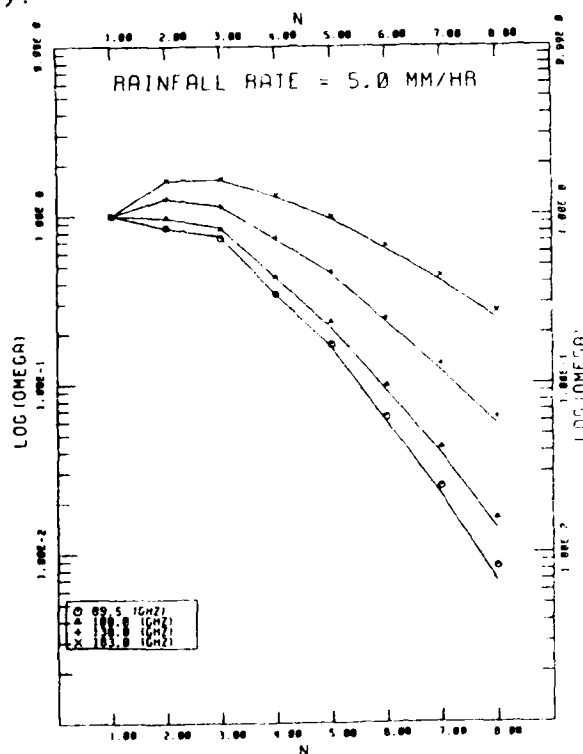


Fig. 3-2. Comparison of the first eight Legendre polynomial coefficients (N) of a Marshall-Palmer size distribution of rain drops with a rainfall rate of 5 mmhr^{-1} calculated by the subroutine (lines) and exact Mie theory calculations from 89.5 to 183 GHz.

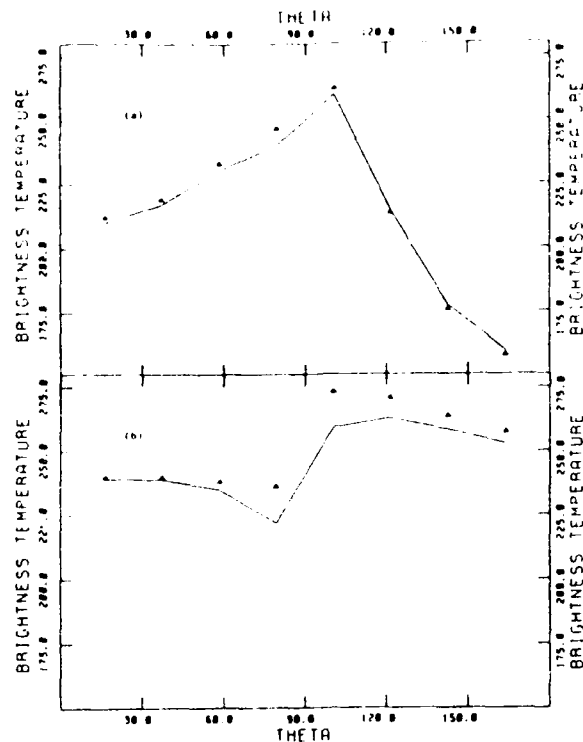


Fig. 3-3. Comparison between exact (lines) and approximate (symbols) brightness temperature calculations as a function of viewing angle (THETA) for a 3 km rain layer with rainfall rate of 15 mmhr^{-1} at (a) 19.35 GHz and (b) 37.0 GHz.

distribution, the modified gamma distribution, and the log-normal distribution. The modified gamma distribution, for example, given by:

$$n(r) = a r^{\alpha} \exp(-b r^{\gamma}) \quad (3.5)$$

can be used to express the commonly used Marshall-Palmer distribution for precipitation:

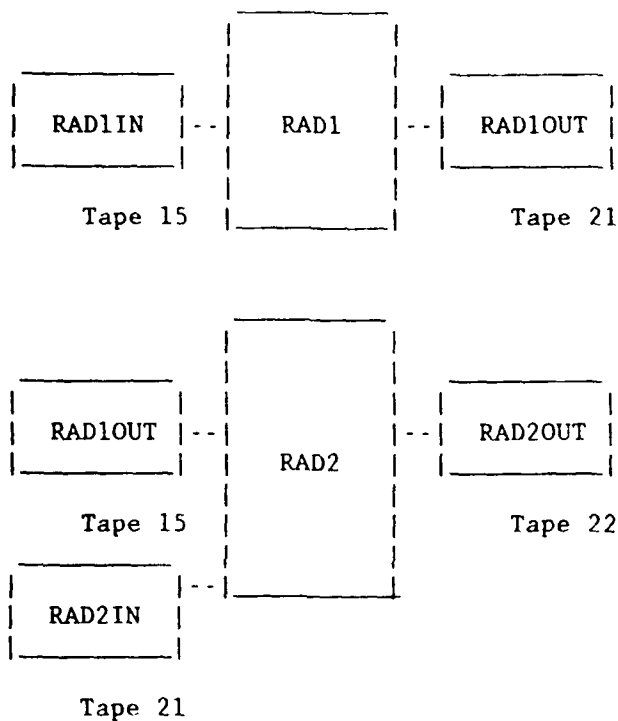
$$n(r) = N_0 \exp(-b r) \quad (3.6)$$

where $N_0 = 8.0 \times 10^6 \text{ m}^{-4}$ and $b = 8200 R^{-0.21}$, and R is the rainfall rate in mm/h. The log-normal distribution is convenient to use to fit experimental drops size data.

Table 3-2 summarizes the file structure for the RAD1 and RAD2 programs and their relationship to one another. For RAD1, a single input file is

required and a single output file results. The output file from RAD1 is used as one input file to RAD2. A second RAD2 input file specifies the parameters defining the desired size distribution.

Table 3-2. File Structure Relating RAD1 and RAD2 Programs



The input file RAD1IN is a single record which specifies the real and imaginary parts of the complex index of refraction, n_1 and n_2 , respectively, the initial Mie parameter, x , the Mie parameter increment, δx , the total number of x 's desired, Nx , and an integer specifying the desired program option, NOPT (-1 or 2). To obtain the desired output file for RAD2 the option NOPT - 1 is selected. The input file and format is illustrated in Table 3-3.

Table 3-3. RAD1IN Input File and Format

| Card 1 | N1 | N2 | X1 | DELX | NX | NOPT |
|--------|-------|-------|-------|-------|----|------|
| | D15.5 | D15.5 | D15.5 | D15.5 | I5 | I5 |

The Mie parameter x is a dimensionless function of the droplet radius, r , and wavelength, λ , given by:

$$x = 2\pi r / \lambda \quad (3.7)$$

The specification of the input file for RAD1 is not independent of that for RAD2 which requires the upper and lower limits in radius to the integration of optical properties over the desired size distribution. The range of Mie parameters calculated by RAD1 must at least span that asked for in the integration of the RAD2 program. For example, if the desired wavelength of the calculation is λ , and the upper and lower radius limits are r_2 and r_1 , respectively, the initial Mie parameter value, x , specified in the RAD1IN file must be less than or equal to:

$$x_{\min} = 2\pi r_2 / \lambda \quad (3.8)$$

Furthermore the largest Mie parameter calculated by RAD1 x_{\max} must be greater than or equal to:

$$x_{\max} = x + \delta x * Nx = 2\pi r_1 / \lambda \quad (3.9)$$

The main input file to RAD2 in the output file of RAD1 which we have called RAD1OUT. This file contains Nx records corresponding to the Mie efficiency factors for extinction, absorption, and scattering and the Legendre polynomial expansion coefficients for each size specified in the input to RAD1 in the interval from x to $x + \delta x * Nx$. The other input file RAD2IN consists of three records illustrated in Table 3-4 for the modified gamma distribution (see equation (3.5)).

Table 3-4. RAD2IN Input File and Format

| | | | | | | |
|--------|-----------|------------|------------|----------|-------|----|
| Card 1 | a | α | b | γ | blank | 2 |
| Card 2 | λ | r_{\min} | r_{\max} | | | |
| Card 3 | blank | | | | | |
| | D15.5 | D15.5 | D15.5 | D15.5 | I5 | I5 |

The parameter JDIS determines the type of size distribution selected with values 1, 2, and 3 corresponding to the discontinuous power law distribution, modified gamma function, and log-normal distribution, respectively. Specifications for the other size distribution options can be found in Dave (1972).

Output from RAD2 is illustrated in Table 3-5. Two calculations are illustrated, both for Marshall-Palmer size distributions with 5 mm/h of rain (see equation (3.6)). The results at the top of the table are for a frequency of 89.5 GHz (i.e., 0.335 cm) while those at the bottom are for 183 GHz (i.e., 0.164 cm). The values numbered from 1 to N concluding each output are the coefficients of the Legendre polynomial expansion of the phase function, w_1 (see equation (3.4)). The first 16 of these coefficients would be required as input for a sixteen stream run of the discrete ordinate multiple scattering code.

3.3 Thermal Radiative Transfer for Polarized Inhomogeneous Nonisothermal Atmospheric Precipitation and Statistical Retrieval of Related Parameters

3.3.1 Introduction

A numerical approach has been developed to treat the polarized thermal radiative transfer theory applicable to inhomogeneous (stratified), nonisothermal layers composed of different spherical Mie scatterers. Calculations are performed to obtain the microwave brightness temperatures at the

Table 3-5. Sample Output Files from the RAD2 Code for a Marshall-Palmer Rain Distribution at 5 mm/h for 89.5 (top) and 183 (bottom) GHz

(a) 89.5 GHz

```

NPART= 1.500E+03
WAVELENGTH=3040.01 R SUB MIN =100.0000 R SUB MAX =4000.00
DELTA X = 0.0050 REP 0.76000 DELT = 1.00000
WAVELENGTH AND RADII ARE IN MICRON UNITS.
MODIFIED GAMMA DISTRIBUTION: A = 1.6000E-05 ALPHA = 0.0000E+00
B = 0.0000E+00 GAMMA = 1.0000E+00
(BETA SUB EXT )/TOTPAR = 7.07209E-03 7.07209E-03
(BETA SUB SCAT)/TOTPAR = 3.06029E-03 3.06029E-03
(BETA SUB ABS )/TOTPAR = 4.01180E-03 N = 30 4.01180E-03
1 0.99999950304E+00 0.84926661835E+00 0.73303075408E+00 0.34264942205E+00
5 0.17103001108E+00 0.64006765390E-01 0.24690200366E-01 0.83516436871E-02
9 0.08010101540E-00 0.39609807504E-03 0.23225695601E-03 0.85344872203E-04
13 0.02550819750E-04 0.14017421297E-05 0.21151001496E-05 0.57760467109E-06
17 0.01489710157E-06 0.35175703002E-07 0.74883034765E-03 0.14209293766E-08
21 0.02398042064E-09 0.36281896132E-10 0.48630796155E-11 0.58987853374E-12
25 0.06450027070E-10 0.63527845696E-14 0.56034755253E-15 0.44013831866E-16
29 0.00400331490E-17 0.18067481834E-18 0.91592887805E-20 0.34729192991E-21
33 0.10810009903E-22 0.00000000000E+01 0.00000000000E+00 0.00000000000E+00

```

(b) 183 GHz

```

NPART= 1.500E+03
WAVELENGTH=1603.02 R SUB MIN =100.0000 R SUB MAX =4000.00
DELTA X = 0.0050 REP 0.76000 DELT = 0.81000
WAVELENGTH AND RADII ARE IN MICRON UNITS.
MODIFIED GAMMA DISTRIBUTION: A = 1.6000E-05 ALPHA = 0.0000E+00
B = 0.0000E+00 GAMMA = 1.0000E+00
(BETA SUB EXT )/TOTPAR = 8.84404E-03 8.84404E-03
(BETA SUB SCAT)/TOTPAR = 4.14132E-03 4.14132E-03
(BETA SUB ABS )/TOTPAR = 4.70270E-03 N = 50 4.70270E-03
1 0.9999998257E+00 0.16291053949E+01 0.16508725193E+01 0.13304212097E+01
5 0.09105924618E+00 0.66663533653E+00 0.43842449028E+00 0.27248934529E+00
9 0.06661650546E+00 0.98704599117E-01 0.57685245240E-01 0.33039035000E-01
13 0.01872350305E-01 0.10461304104E-01 0.57961525285E-02 0.31778801820E-02
17 0.01730419094E-02 0.03467771902E-03 0.50195241105E-03 0.26781619551E-03
21 0.01421680780E-03 0.75041592322E-04 0.39411660154E-04 0.20577708927E-04
25 0.01067720306E-04 0.54552789190E-05 0.27986093565E-05 0.14041190173E-05
29 0.06900327167E-06 0.32513409104E-06 0.15060541641E-06 0.65091911357E-07
33 0.02620355117E-07 0.07170094278E-08 0.32983680809E-08 0.10223022628E-08
37 0.00894596525E-09 0.75092971500E-10 0.17904750885E-10 0.39396948817E-11
41 0.00030278130E-10 0.15010789124E-12 0.26818649693E-13 0.43952415286E-14
45 0.06674759998E-15 0.93575785118E-16 0.12053382907E-16 0.14160849749E-17
49 0.00490000000E-18 0.13080252001E-19 0.11030930469E-20 0.63364559701E-21
53 0.00000000000E-20 0.00000000000E+01 0.00000000000E+01 0.00000000000E+01

```

SSM/1 frequencies 19.35, 22.235, 37, and 85.5 GHz in the presence of atmospheric precipitation with a top ice crystal layer or inhomogeneous structure. The surface emission from various underlying media including calm and rough ocean, sea ice, snowpack, and vegetation are taken into account. Functional relationships between emitted thermal radiation from atmospheric precipitation and rainfall parameters are discussed. By using a statistical regression technique (the D-matrix method), the geophysical parameters, rain rate, and emissivity from the underlying surface, etc., are retrieved from simulated data. The error analysis is discussed.

Radiative transfer theory applicable to the multiple scattering of microwaves has been extensively applied to the study of atmospheric precipitation and clouds (Wilheit et al., 1977; Ishimura and Cheung, 1980; Tsang and Kong, 1977; Jin and Kong, 1983). The previous modeling, however, has focused on the single homogeneous, isothermal layer of Mie scatterers. In well-developed precipitating clouds, it has been observed (Wilheit et al., 1982) and calculated by the one-layer model (Wilheit et al., 1982; Huang and Liou, 1983) that an ice crystal layer over precipitation significantly cools the emergent microwave thermal emission, especially at higher frequencies. Here a numerical approach is described to solve the coupled radiative transfer equations for two-stratified, nonisothermal layers composed of different (component and size distributed) spherical Mie scatterers. It is applied to calculations of emitted thermal radiation from atmospheric precipitation with a top ice crystal layer or with nonhomogeneous structure (e.g., two layers of precipitation with different rainfall rates). Two radiative transfer equations are solved by the Gaussian quadrature method. The coefficients of the eigenvectors in the two respective regions are determined by solving four coupled boundary conditions. The emission effects from various underlying media, including calm and rough sea surfaces, dry and wet snowpacks, first- and multi-year sea ice, and land with varying soil moisture content and vegetation are modeled by a layer of scattering medium (Jin, 1984).

Geophysical parameter retrieval is an inverse problem for remote sensing of atmospheric and earth terrain surface properties. The retrieval of atmospheric temperature and water vapor profiles have been studied for non-precipitating atmospheres based upon the scalar nonscattering radiative transfer equations (Rodgers, 1976; Gaut et al., 1973; Rosenkranz et al.,

1982). In this paper, we apply the statistical D-matrix retrieval technique to retrieve the geophysical parameters of interest in remote sensing of precipitation over ocean and land. By a Monte Carlo method, the most probable combination of the atmospheric and surface properties for available measurements is selected in a statistical sense. Then, by our simulation modeling calculation described above, a set of simulated radiometric data is produced. By using a statistical regression technique, the appropriate D-matrix is obtained to retrieve the desired parameters, such as rain rate, surface emissivities for both vertical and horizontal polarizations, atmospheric opacity, temperature lapse rate, and surface temperature. Results indicate that the statistical D-matrix method is working properly for the retrieval of these geophysical parameters in the presence of atmospheric precipitation. Some restrictions and error analyses are also discussed.

3.3.2 Thermal Radiative Transfer Theory

The theoretical model is shown in Figure 3-4. Two layers, region f and region l, are composed of different spherical Mie scatterers with complex dielectric constants ϵ_{sf} and ϵ_{sl} , respectively, and appropriate size distributions. Temperature profiles are assumed to be linear with the lapse rate Γ_f and Γ_l ($^{\circ}\text{C}/\text{km}$) in respective regions. From the vector radiative transfer theory and Gaussian quadrature method (Tsang and Kong, 1977; Jin and Kong, 1983) we have the radiative transfer equations as follows:

$$\begin{aligned} \cos\theta_i \frac{d}{dz} I_{\beta_l}(\theta_i, z) = & (k_{al} + k_{gl}) CT_l(z) - (k_{el} + k_{gl}) I_{\beta_l}(\theta_i, z) \\ & + \sum_{j=-N}^N a_j [(\beta_i, \beta_j)_l I_{\beta_l}(\theta_j, z) + (\beta_i, \alpha_j)_l I_{\alpha_l}(\theta_j, z)]. \end{aligned} \quad (3.10a)$$

$$\begin{aligned} \cos\theta_{if} \frac{d}{dz} I_{\beta_f}(\theta_{if}, z) = & (k_{af} + k_{gf}) CT_f(z) - (k_{ef} + k_{gf}) I_{\beta_f}(\theta_{if}, z) \\ & + \sum_{j=-N_f}^{N_f} a_j [(\beta_i, \beta_j)_f I_{\beta_f}(\theta_{jf}, z) + (\beta_i, \alpha_j)_f I_{\alpha_f}(\theta_{jf}, z)]. \end{aligned} \quad (3.10b)$$

where the subscripts 1 and f denote the functions or parameters taken in the respective region 1 and region f; β , α denote vertical or horizontal polarization v or h; k_a , k_e are the absorption and extinction coefficients of the scatterers; k_g is the atmospheric gas (oxygen and water vapor) absorption coefficient; $T(z)$ is the physical temperature profile of atmosphere; (β_j, β_j) , (β_i, α_j) , etc., are the scattering phase functions calculated by Mie scattering theory; a_j are Christoffel numbers, N is the number taken by Gaussian quadrature. The temperature profiles are assumed as

$$T_1(z) = T_1^{(0)} - (z+d) \cdot \Gamma_1 \quad (3.11a)$$

$$T_f(z) = T_f^{(0)} - z \cdot \Gamma_f, \quad (3.11b)$$

where $T_1^{(0)}$, $T_f^{(0)}$ are the temperature at $z = -d, 0$ (Fig. 3-4). In the case of atmospheric precipitation, where the fractional volume of scatterers is very small, the mean permittivities of region 1 and f are not quite different. Thus, we can assume that

$$\theta_{fi} = \theta_i \text{ and } N_f = N \quad (3.12)$$

Therefore, $a_{jf} = a_j$. Otherwise, $\cos\theta_{fi}/\cos\theta_i$ can be decided by the Snell's law, and a_{jf} can be calculated by the trapezoidal rule. The coupled boundary conditions are obtained as follows:

$$I_{\beta f}(\pi - \theta, z = s) = 0 \quad (3.13a)$$

$$I_{\beta 1}(\pi - \theta, z = 0) = I_{\beta f}(\pi - \theta, z = 0) \quad (3.13b)$$

$$I_{\beta 1}(\theta, z = 0) = I_{\beta f}(\theta, z = 0) \quad (3.13c)$$

$$I_{\beta 1}(\theta, z = -d) = \gamma_{12\beta}(\theta) I_{\beta 1}(\pi - \theta, z = -d) + \tau_{12\beta}(\theta) T_2 \quad (3.13d)$$

where

$$\begin{aligned} \tau_{12\beta}(\theta) T_2 &= [1 - \gamma_{\beta}(\theta)] T_2 e^{-k_{ga} D \sec\theta} \\ &+ k_{ga} \sec\theta \int_0^D dz T_a(z) e^{-k_{ga}(D-z)\sec\theta} \end{aligned} \quad (3.14a)$$

$$+ \gamma_{\beta}(\theta) k_{ga} \sec \theta e^{-k_{ga} D \sec \theta} \int_0^D dz T_a(z) e^{-k_{ga} z \sec \theta}$$

$$\text{and } \gamma_{12\beta}(\theta) = 1 - t_{12\beta}(\theta) \quad (3.14b)$$

where the underlying surface reflectivity $\gamma_{\beta}(\theta)$ is determined by the calculations given in (Smith et al., 1979) for underlying scattering medium. From the Gaussian quadrature, we obtain the solutions of equations (3.10) and (3.10) in terms of the respective eigenvectors, corresponding eigenvalues and unknown coefficients which will be determined by the coupling boundary conditions ((3.13a) through (3.13d). Substituting these solutions into (3.13a) - (3.13b) we obtain the desired coefficients by matrix inversion. Then, finally, we obtain the observed brightness temperature in region 0 as

$$\bar{T}_B = \bar{T}_o^{(0)} + (\bar{E}_f + \bar{Q}_f) \cdot \bar{X}_f + (\bar{E}_f - \bar{Q}_f) \cdot \bar{U}_f(s) \cdot \bar{Y}_f + \frac{\mu_i}{k_{af}} \bar{\Gamma}_f. \quad (3.15)$$

where $\mu_i = \cos \theta_i$,

$$\bar{T}_B = \text{column } [T_{v1}, \dots, T_{vN}, T_{h1}, \dots, T_{hN}],$$

$$\bar{T}_o^{(0)} = \text{column } [T_o^{(0)}, \dots, T_o^{(0)}], \quad T_o^{(0)} = T_f^{(0)} - s \Gamma_f,$$

$$\bar{\Gamma}_f = \text{column } [\Gamma_f, \dots, \Gamma_f],$$

$$\bar{X}_f = \text{column } [x_{1f}, \dots, x_{2Nf}] \text{ determined by (3.13a)-(3.13d),}$$

$$\bar{Y}_f = \text{column } [Y_{1f}, \dots, Y_{2Nf}] \text{ determined by (3.13a)-(3.13d)}$$

$$\bar{E}_f = 2N \times 2N \text{ eigenvector matrix}$$

$$\bar{Q}_f = 2N \times 2N \text{ matrix related with the eigenvector}$$

$$\bar{U}_f(z) = \text{diag } [e^{-\alpha_{1f} z}, \dots, e^{-\alpha_{2Nf} z}], \quad \alpha_{if} (i=1, \dots, 2N) \text{ eigenvalue}$$

One of the numerical results is shown in Fig. 3-5. We take $N = 6$. The permittivity of ϵ_{sf} , ϵ_{sl} , and ϵ_b of calm ocean are calculated by the Debye formula, a Marshall-Palmer precipitation dropsize distribution is used for liquid and solid precipitation in both regions 1 and f. Results indicate a significant cooling for 85.5 GHz due to the top ice layer, even at moderate rain rates. Dotted lines show the case without the top ice layer. By modeling the underlying media as a layer of random discrete scatterers and choosing physically reliable parameters for the size, fractional volume, and permittivity of the scatterers and layer thickness, background permittivity, etc., the emissivity $e_\beta(\theta)$, and reflectivity $r_\beta(\theta)$ are calculated and input into the calculation of (3.14a) and (3.14b) for underlying rough sea surface with foam, FY and MY sea ice, dry and wet snow, moistured land and vegetation. More results and detailed discussions will be given in the future paper.

3.3.3 Statistical Retrieval of Geophysical Parameters

By the Monte Carlo method, we choose, in a statistical sense, most probable combinations of geophysical parameters to reproduce the available measurements through the forward calculations by our theoretical modeling. The inverse problem is whether these geophysical parameters can be inferred from the simulated radiometric measurements. From the statistical retrieval techniques (Rogers, 1976; Gaut et al., 1975; Isaacs and Deblonde, 1987) D-matrix method, the estimated parameters of p is generated by

$$\underline{p} = \underline{D} \cdot \underline{\phi} \quad (3.16)$$

where the D-matrix is previously computed by

$$\underline{D} = \underline{C}(p, \underline{\phi}) \underline{C}^{-1}(\underline{\phi}, \underline{\phi}) \quad (3.17)$$

where \underline{p} , \underline{d} are the parameter and data vectors, the underbar denotes the vector, $\underline{\phi}$ is a generalized data basis function and defined as $\underline{\phi} =$ column $(1, (\bar{d}_1 - \bar{d}_1)/\bar{d}_1, \dots, (\bar{d}_m - \bar{d}_m)/\bar{d}_m)$ for m channel radiometric data, where superbar denotes the mean value, $\underline{C}(p, \underline{\phi})$ and $\underline{C}(\underline{\phi}, \underline{\phi})$ are the correlation matrices of $\underline{p}, \underline{\phi}$ and $\underline{\phi}, \underline{\phi}$, respectively.

We specify the most interesting parameters: rain rate, emissivity for both vertical and horizontal polarization from the underlying surface, atmospheric opacity, temperature lapse rate, and surface temperature, to combine the parameter vector p . The data vector d is obtained from the simulated results of eight channels (four frequencies, 19.35, 22.235, 37, and 85.5 GHz) viewing the surface at a nadir angle of 54° . By using 100 observations of ensemble parameter vector p_A and data vector d_A (set A) to compute D-matrix, another ensemble d_B of set B is then used to estimate the parameter p_B , and the ground truth p_B will be compared for overall error analysis. In the presence of multiple scattering in precipitation and surface emission, the relationship between d and p is much more sophisticated than a simple linear function. However, in a statistical sense, as long as the mean value and variance of the ensemble set B are not significantly deviated apart from a priori set A, the retrieval techniques of D-matrix is working fairly well.

Results are shown in Figs. 3-6 and 3-7 for retrieval of rain rate and emissivity of underlying surface. It is shown that as the mean value and variance of set B is close to those in a priori set A, retrievals are fairly good. Large deviation from a priori value causes large error in retrieval since D-matrix relies on a priori information as given in (3.17).

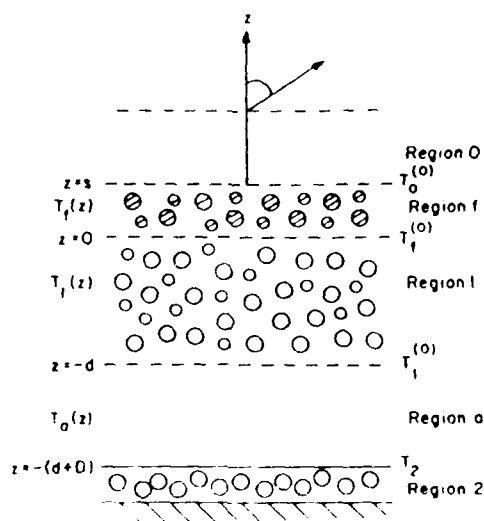


Figure 3-4. The geometry of the theoretical modeling.

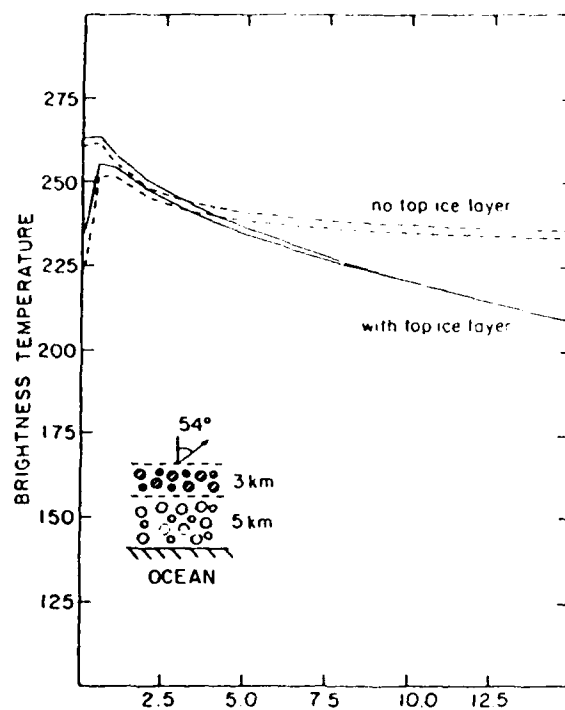


Figure 3-5. Brightness temperature vs. rain rates.

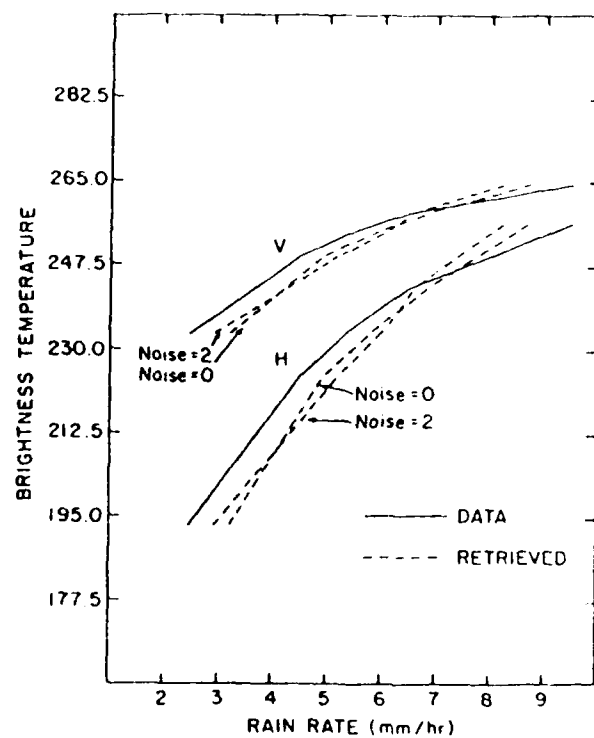


Figure 3-6. Retrieval of rain rates.

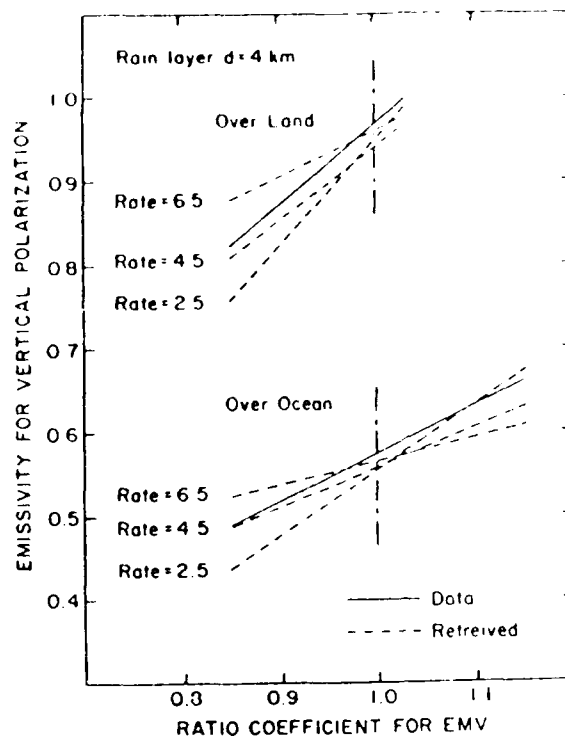


Figure 3-7. Retrieval of emissivities.

3.4 Surface Modeling

The Air Force Geophysics Laboratory (AFGL) RADTRAN code is used to calculate transmission and brightness temperature spectra for atmospheric slant paths in the frequency range between 1 and 1000 GHz (Falcone et al., 1979; Falcone et al., 1982). The atmospheric attenuation submodels of the clear atmosphere, fog, cloud, and rain used in RADTRAN have been thoroughly documented (Falcone et al., 1982). These submodels provide the necessary data to evaluate gaseous and particulate emission and other potential contributions to slant path brightness temperature from scattering in the atmosphere due to the presence of precipitation. The RADTRAN code is frequently applied to microwave systems effectiveness simulation studies for both airborne and satellite-based sensors viewing the earth's surface. Such applications require the capability to supplement the atmospheric radiative transfer calculation with realistic models of the microwave properties of the sensor scene field-of-view allowing for variations in polarization and frequency dependence of emissivity

due to changes in surface type. Frequently, this information is provided via available empirical data sets. However, the range of available field measurements is limited. In order to facilitate the evaluation of sensor performance throughout a range of pertinent geophysical surface scenarios, deterministic models of microwave surface emission are desired which can be exercised concurrently with the models for atmospheric transmission. To achieve this goal, a set of microwave surface emission models has been implemented to accompany the RADTRAN atmospheric properties model (Isaacs et al., 1988b). In addition to obvious applications to microwave background simulations, application of such models to remote sensing simulation studies can also provide a theoretical basis for understanding of the sensitivity of microwave sensor data to variations in relevant hydrological parameters such as soil moisture, snow, and vegetative moisture content.

3.4.1 Surface Modeling Approaches

The selection of a simple surface modeling approach is made difficult by the complexity of geophysical surfaces. For example, homogeneous dielectric slab models for both land and ocean have been commonly used to provide the required surface emissivity parameters to initiate brightness temperature simulation calculations. It is apparent from an examination of recent microwave satellite imagery that such approaches cannot reproduce the fidelity of the complex fields of observed surface properties. This is due to the neglect of important physical mechanisms such as scattering by such approaches, and their failure to treat the spatial inhomogeneities in dielectric properties due to the inherent physical structures of real surfaces. On the other hand, it is necessary to consider the computational level of effort required to model all of the physics, even if it were well understood.

Related to the choice of an appropriate model, is the detail of surface type characterization desired, i.e. how many surface types to treat. In reality, of course, there is a continuum of geophysical surface types. A sufficiently general model can attempt to simulate some of the behavior exhibited by subsets of surface types within this continuum by choosing appropriate parameterizations of relevant surface properties and varying them within representative ranges. The choice of surface types employed within the RADTRAN surface modeling package was based both on the desire to treat a com-

prehensive set of surfaces and, to some extent, on the requirements of potential model users with specific surface related simulation applications. The surface types selected are: (a) calm and rough ocean, (b) first year (FY) and multiyear (MY) sea ice, (c) wet and dry snow over land, (d) wet and dry soil, (e) vegetation, and (f) land. The land surface type provides a background for snow, soil, and vegetation models in addition to its potential role as a distinct surface type itself.

Both the calm ocean and land are modeled as simple dielectric slabs. The other surface types, however, clearly require a more sophisticated modeling treatment. As the following discussion will indicate, it is not appropriate to treat all of the surface types delineated above by a single formalism. Therefore, two distinct approaches have been applied in the development of these surface emission models: that based on wave theory for random discrete scatterers and that based on radiative transfer theory for continuous random media. In the sections to follow, the former approach is applied to modeling the ocean surface, sea ice, and snow, while the latter is applied to both soil and vegetation. These approaches are summarized in Table 3-6.

Table 3-6. Surface Model Types and Modeling Approaches

| Model | Surface Type | Modeling Approach |
|-------|--------------|----------------------------|
| 1 | Calm ocean | Dielectric slab |
| 2 | Rough ocean | Random discrete scatterers |
| 3 | FY sea ice | Random discrete scatterers |
| 4 | MY sea ice | Random discrete scatterers |
| 5 | Dry snow | Random discrete scatterers |
| 6 | Wet snow | Random discrete scatterers |
| 7 | Land | Dielectric slab |
| 8 | Wet soil | Continuous random medium |
| 9 | Vegetation | Continuous random medium |

In the wave theory approach for random discrete scatterers, one or more layers is defined consisting of a dielectric medium with either uniform properties or containing a random distribution of discrete dielectric spheres

with distinct dielectric properties. These latter inclusions give the medium scattering properties which by appropriate choice of the background and inclusion permittivities can be tuned to exhibit the observed behavior of sea ice and dry snow, for example. The radiative transfer approach for continuous random media approaches the problem of modeling the surface from a different perspective. Some surfaces are spatially inhomogeneous in their dielectric properties, yet the inhomogeneities are not due to discrete spherical scatterers. The approach provides an alternative treatment in which the permittivity is varied continuously throughout the medium. Furthermore, these spatial variations are parameterized in such a manner that the relative effects of variations in the vertical and horizontal physical structure of the medium can be modeled. The application of this approach to soils and vegetation is obvious.

3.4.2 Application of Wave Theory Models for Discrete Scatterers

A variety of surface types can be modeled as either: (a) a single layer with uniform dielectric properties, (b) a single layer including a random distribution of discrete scatterers, or (c) two bounded layers, each with one of the above characteristics. The most straightforward example of the first type is the calm ocean surface which has been modeled in this study as a homogeneous half space medium with microwave dielectric properties calculated by the Debye formula. Figure 3-8 illustrates the resultant variation of emissivity with frequency for each polarization and a look angle of 54° . This angle was chosen to correspond to that of a conically scanning radiometer such as the NIMBUS 7 Scanning Multichannel Microwave Radiometer (SMMR) or DMSP Special Sensor Microwave Imager (SSM/I). The emissivity of a rough sea surface is greater than that of a smooth sea because the wind-driven rough sea surface is covered with a layer of foam and white caps. Calm seas are defined as those for which the ocean surface wind speed is less than about 7 ms^{-1} , while rough seas are present when surface wind speeds exceed this critical value. The effect of white water (foam and white caps) have been modeled as a layer of porous dielectric (Droppleman, 1970) and a series of thin water films (Rosenkranz, 1972). In this study, the wind-driven rough sea is modeled by a layer of random discrete scatterers with a periodic rough surface. The dependence of emissivity on look angle is shown in Figure 3-9. Numerical

results are consistent with observations (Rosenkranz, 1972). Increased emissivity due to the foam layer is about 0.04 at a look angle of 11° , and the resultant brightness temperature increase is about 11° , which corresponds to a wind speed of about 10 m/sec. Increase of the fractional volume of foam would also increase the brightness temperature.

Snowpack over land is modeled as a bounded layer of random discrete scatterers. Dry snow is composed of ice particles and air, while wet snow consists of small water drops, ice particles, and air. The wave theory approach for a bounded layer of random discrete scatterers is used to calculate the emissivity (Jin and Kong, 1984). This approach includes first and second order scattering effects and is especially applicable to modeling densely distributed random discrete scatterers. Figure 3-10 shows the frequency dependence of snowpack emissivity at a look angle of 54° . A snow depth of 60 cm is assumed. As frequency increases, the effect of scattering is enhanced. This results in a decrease of emissivity. Figure 3-11 also shows the variation in snowpack emissivity with wetness. As wetness increases, the emissivity of the snowpack gradually increases due to increased thermal emission. Snowpack emissivity as a function of angle at 18.0 GHz is illustrated in Figure 3-11. For comparison, the angular variation of emissivity for a snow-free land surface is included. There is a significant decrease in the vertical emissivity due to the presence of snow. This difference is modulated by variations in both snow depth and wetness.

The approach can also be applied to calculate the emissivities of first year (FY) and multiyear (MY) sea ice. It is known that there is a strong contrast between the emissivity of sea ice and that of the ocean. The emissivity of sea ice depends on age, thickness, salinity, density, composition and surface characteristics (Comiso, 1983). To some extent, thickness, t , and density, ρ , are correlated with ice age. First year sea ice has a layer of thin congelation ice (20 cm , $\rho \approx 0.85\text{ gm/cm}^3$) over a thick congelation ice layer ($\rho \approx 0.92\text{ gm/cm}^3$). Multiyear sea ice has a recrystallized ice layer ($t \sim 50\text{ cm}$) over a congelation ice layer with thickness up to 500 cm. The recrystallized ice layer of MY sea ice ($\rho \approx 0.7\text{ gm/cm}^3$) has a large fractional volume of air pockets which cause scattering and darken thermal emission from the underlying medium. In our calculations, MY sea ice was modeled as a bounded layer of random discrete scatterers (air pockets embedded in homogene-

ous ice medium) over a homogeneous ice medium, while FY sea ice is modeled as two layers of homogeneous ice media with appropriate complex dielectric constants. Calculated emissivities as functions of frequency and look angle for FY and MY sea ice are shown in Figures 3-12 and 3-13, respectively. Results are fairly consistent with the observations and experimental data (Comiso, 1983; Simonett, 1983).

3.4.3 Application of Radiative Transfer Theory Models for Continuous Random Media

Experimental measurements of the thermal emission from wet soil and vegetative canopies have been studied by a number of investigators (Ulaby et al., 1983; Ulaby and Jedlicka, 1984; Schmugge et al., 1977; Schmugge, 1983) by means of truck-mounted, airborne, and satellite radiometers at low frequencies, such as 1.4 and 5 GHz. Measurements at higher frequencies have not been well studied due to some difficulties (Ulaby et al., 1983). Theoretical analyses are usually restricted to finding an effective permittivity for wet soil and vegetation at these frequencies. Modeling using the radiative transfer equation including multiple scattering, has, however, also been investigated (Wang and Schmugge, 1980; Wang et al., 1984).

In the RADTRAN surface emissivity model implementation wet soil and vegetation are modeled as layers of continuous random medium bounded by an underlying homogeneous medium. Random dielectric fluctuations in these media are characterized by their respective spatial correlation functions. The mean permittivity and variance are calculated by using the appropriate multiphase mixture formula (Ulaby and Jedlicka, 1984; Wang and Schmugge, 1980). A numerical Gaussian quadrature method similar to that described in (Jin and Isaacs, 1987) is then used to solve the radiative transfer equation to calculate emissivity.

The theoretical model for wet soil or vegetative canopy consists of a layer of random medium with permittivity $\epsilon(\vec{r})$, with mean value, ϵ_m , and fluctuating part, $\epsilon_f(\vec{r})$:

$$\begin{aligned}\epsilon(\vec{r}) &= \epsilon_m + \epsilon_f(\vec{r}), \\ \langle \epsilon_f(\vec{r}) \rangle &= 0.\end{aligned}\tag{3.18}$$

The mean value of the permittivity, ϵ_m , may be related to the relevant mixture components and the physical structure of the layer. In our soil model, the empirical mixture formula given by Wang and Schmugge (Wang and Schmugge, 1980) is used:

$$\begin{aligned} \text{For } W_c \leq W_t \\ \epsilon_m &= W_c \epsilon_x + [P - W_c] \epsilon_b + (1 - P) \epsilon_{\text{rock}} \\ \epsilon_x &= \epsilon_{\text{ice}} + [\epsilon_{\text{water}} - \epsilon_{\text{ice}}] [W_c/W_t]^\gamma \end{aligned} \quad (3.19a)$$

$$\begin{aligned} \text{For } W_c > W_t \\ \epsilon_m &= W_t \epsilon_x + [W_c - W_t] \epsilon_{\text{water}} + (P - W_c) \epsilon_b + (1 - P) \epsilon_{\text{rock}} \\ \epsilon_x &= \epsilon_{\text{ice}} + [\epsilon_{\text{water}} - \epsilon_{\text{ice}}]^\gamma \end{aligned} \quad (3.19b)$$

where W_c is the volumetric moisture, and W_t is the transient moisture. The transient moisture denotes the turning point for transition of the dielectric permittivity from slow to steep behavior, ϵ_x stands for the dielectric constant of the initially absorbed water, γ is a parameter (about 0.3 to 0.5), ϵ_{ice} , ϵ_{water} , ϵ_{rock} , and ϵ_b are the dielectric constants for ice, water, rock, and background medium, respectively. Equation 3.19 is an empirical formula which is based on the behavior of the biphasic dielectric properties of water in soils, i.e., below the transient moisture, the dielectric property of the soil water is thought to be like that of ice, while above W_t , the water dielectric constant is used. In our calculations the following constants are used: $W_t = 0.25$, $\gamma = 0.45$, $P = 0.5$, $\epsilon_{\text{rock}} = (5, 0)$, $\epsilon_{\text{ice}} = (3, 0.01)$, and ϵ_{water} is calculated by the Debye formula which depends on the temperature and frequency (Sadiku, 1985).

For a vegetative canopy, the four-phase refractive model of the mixture following (Schmugge et al., 1977) is used as

$$\sqrt{\epsilon_v} = V_a + V_{fw} \sqrt{\epsilon_{\text{water}}} + V_{bw} \sqrt{\epsilon_{bw}} + (1 - m_v - V_a) \sqrt{\epsilon_{\text{bulk}}} \quad (3.20a)$$

where V_a , V_{fw} , and V_{bw} are the volumetric fraction of air, free water, and bound water in the vegetation, respectively; m_v is the volumetric wetness of the vegetation, ϵ_{bw} is taken as that of ice, and the bulk dielectric constant, ϵ_{bulk} is taken as (5.5, 0.1). Therefore, the mean value, ϵ_m , in the layer of vegetation is

$$\epsilon_m = V_v \epsilon_v + (1 - V_v) \epsilon_b \quad (3.20b)$$

where V_v is the volumetric layer fraction, taken to be 0.0033 and the quantity $(1 - m_v - v_z) \approx 0.1$ (Ulaby and Jedlicka, 1984). The variance δ is calculated from

$$\delta = \frac{V_v |\epsilon_v - \epsilon_m|^2 + (1 - V_v) |\epsilon_b - \epsilon_m|^2}{|\epsilon_m|^2} \quad (3.21)$$

The above formulas (3.19) and (3.20) and parameters are consistent with available measurements of the permittivity at 1.4 and 5 GHz (Ulaby and Jedlicka, 1984; Wang and Schmugge, 1980). These expressions were extended to higher frequencies (19.35, 22.235, and 37 GHz) for calculation of the mean value ϵ_m , based on the observation that the dielectric constants of ice and rock are not very sensitive to changes in the frequency in this region, while the dielectric constant of water can be calculated by the Debye formula. It has been assumed that the possible anisotropic and inhomogeneous properties of vegetation are not significant enough to effect this approximation.

The correlation function of dielectric fluctuation in random media is usually assumed to be Gaussian in the transverse direction and exponential in the vertical (Tsang and Kong, 1976).

$$\langle \epsilon_f(\bar{r}_1) \epsilon_f^*(\bar{r}_2) \rangle = \delta |\epsilon_m|^2 \exp \left[- \frac{[x_1 - x_2]^2 + [y_1 - y_2]^2}{\ell_\rho^2} - \frac{|z_1 - z_2|}{\ell_z} \right] \quad (2.22)$$

The transverse and vertical correlation lengths ℓ_ρ , ℓ_z , and variance, δ , which characterize the magnitude of scattering effects, are dependent on the size, shape, and spatial distribution of the scatterers. An analysis applying these concepts to simple dry snowpack can be found in (Vallese and Kong, 1981). For the more complicated case of a vegetative canopy, it is possible to define the optimal correlation lengths which give the proper scattering intensity magnitudes.

By using the radiative transfer equation in region 1, and applying the Gaussian quadrature method (Jin and Isaacs, 1987; Tsang and Kong, 1976),

$$\cos\theta_i \frac{d}{dz} I_\beta[\theta_i, z] = k_a C T_1 - k_e I_\beta[\theta_i, z] + \sum_{j=-N}^N a_j \left[[\beta_i, \beta_j] I_\beta[\theta_j, z] + [\beta_i, \alpha_j] I_\alpha[\theta_j, z] \right] \quad (3.23)$$

where β and α denote the vertical and homogeneous polarization v or h, and k_a and k_e are the absorption and extinction coefficients, respectively, in region 1. Sixteen quadrature points are used in the calculation. The scattering phase functions are as follows (Tsang and Kong, 1976).

$$\begin{aligned} (v, v') &= Q(\theta, \theta') e^{-W} \{ [\sin^2\theta \sin^2\theta' + 1/2 \cos^2\theta \cos^2\theta'] I_0(W) \\ &\quad + 2 \sin\theta \sin\theta' \cos\theta \cos\theta' I_1(W) + (1/2) \cos^2\theta \cos^2\theta' I_2(W) \} \\ (v, h') &= Q(\theta, \theta') e^{-W} (1/2) \cos^2\theta [I_0(W) - I_2(W)] \\ (h, v') &= Q(\theta, \theta') e^{-W} (1/2) \cos^2\theta' [I_0(W) - I_2(W)] \\ (h, h') &= Q(\theta, \theta') e^{-W} (1/2) [I_0(W) + I_2(W)] \end{aligned} \quad (3.24)$$

$$Q(\theta, \theta') = \frac{\delta k'^4 \ell_\rho^2}{4} \cdot \left\{ \frac{\ell_z}{1 + k'^2 \ell_z^2 (\cos\theta - \cos\theta')^2} \right\} e^{-[k' \ell_\rho / 2]^2 (\sin\theta - \sin\theta')^2}$$

$$W = (1/2) k'^2 \ell_\rho^2 \sin\theta \sin\theta'$$

The boundary conditions are:

$$I_\beta(\theta_1, z=0) = \gamma_{01} \beta(0) I_\beta(\theta, z=0) \quad (3.25)$$

$$I_\beta(\theta_1, z=-d) = \gamma_{12} \beta(\theta) I_\beta(\pi - \theta, z=-d) + C t_{12} \beta(\theta) T_2,$$

where $t_{12} \beta(\theta) = 1 - \gamma_{12} \beta(\theta)$. By solving equations (3.23) through (3.25) we obtain

$$\bar{I}(\theta_1, z=0) = C \left[\bar{T}_1 + (E + Q) \cdot \bar{x} + (E - Q) \cdot U(d) \cdot \bar{y} \right], \quad (3.26)$$

Therefore, the brightness temperatures at the altitude $Z = D$ are given by:

$$\begin{aligned} T_{B\beta}(\theta_{i0}, z=D) &= \{1 - \gamma_{\beta 01}(\theta_{i0})\} \frac{1}{C} I(\theta_i, z=0) e^{-\int_0^D k_g(z) \sec\theta_{i0} dz} \\ &\quad + \int_0^D dz T_a(z) k_g(z) \sec\theta_{i0} e^{-\int_z^D k_g(z') \sec\theta_{i0} dz'} \end{aligned} \quad (3.27)$$

$$+ \gamma_{\beta 01}(\theta_{i0}) e^{-\int_0^D k_g(z) \sec \theta_{i0} dz} \int_0^D dz T_a(z) k_g(z) \sec \theta_{i0} e^{-\int_0^z k_g(z') \sec \theta_{i0} dz'}$$

where θ_{i0} are determined by Snell's law

$$\sqrt{\epsilon'_m} \sin \theta_i = \sqrt{\epsilon_0} \sin \theta_{i0}. \quad (3.28)$$

Eqn. (3.27) provides the required brightness temperature solutions above an atmosphere with gas absorption coefficient equal to $k_g(z)$.

The roughness of the underlying medium, region 2, is treated following (Choudhury et al., 1979) where only the coherent part of the scattered field is taken into account

$$\gamma_{\beta 12}(\theta) = \gamma_{\beta 12}^{(o)}(\theta) e^{-h \cos^2 \theta} \quad (3.29)$$

where $\gamma_{\beta 12}^{(o)}(\theta)$ is the reflectivity for a smooth surface, and h is the effective roughness which is generally smaller than the physical roughness. Tsang and Newton (Tsang and Newton, 1982) obtained a more sophisticated formula which includes the incoherent part and calculated relevant results for 1.4 GHz at a nadir angle for a half-space model. In the two-layer model with a rough boundary at $z = -d$, the incidence of thermal emission should be accounted for from all angles; the approximated calculation near the nadir angle cannot be used. Therefore, our model uses only the effective h to take account of the roughness contribution as given in (3.29). In fact, for fully-grown vegetation, the vegetative canopy will likely shield the soil contribution completely, and the contribution of (3.29) from region 2 is probably not significant at all.

Frequency dependent vertical and horizontal emissivities for dry and wet soils are illustrated in Figure 3-14. Corresponding look angle dependent emissivity results evaluated at a frequency of 18 GHz are shown in Figure 3-15. The model used consists of two layers: an upper layer with a

depth of 50 cm and variable soil moisture and a lower layer with a fixed wetness of 0.2. The dry soil has a moisture volume of 0.1 while the wet soil has a moisture volume of 0.5. Calculations are shown for correlation lengths of (ℓ_p, ℓ_z) equal to (0.1, 1.0), respectively. The observed decrease of brightness temperature with increased soil moisture for both polarizations is illustrated. Notably, the magnitude of emissivity is much more dependent on the specified correlation lengths at low values of soil moisture where scattering is important.

Applying the model to vegetation, specification of the appropriate correlation lengths becomes significant. The correlation lengths are defined such that as the distance between two points becomes larger than the correlation length, their correlation will be less than e^{-1} . Therefore, the correlation lengths actually correspond to a measure of the scatterer size, shape, and spatial distribution. Increasing ℓ_p or ℓ_z means that the scatterers are distributed more horizontally or vertically, respectively. Therefore, the appropriate ℓ_p or ℓ_z for different vegetation canopies are important at high frequencies. If scatterers are spherical, the correlation length is approximately equal to the radius. For fully grown corn, for example, ℓ_z is larger than ℓ_p due to the predominantly vertical physical structure. If the random medium has a laminar structure, i.e. one where vegetation is oriented predominantly in the horizontal direction then $\ell_p \rightarrow \infty$. For this geometry, the behavior of emissivity simulates that of a stratified medium.

Figures 3-16 and 3-17 illustrate emissivity results for four different vegetation models based on two vegetation moisture volumes (0.1, 0.5) and two thicknesses (20 and 200 cm, respectively). Calculations are shown for correlation lengths of (ℓ_p, ℓ_z) equal to (0.1, 1.0), respectively. In general, the behavior of the emissivity results can be understood in terms of the influence of the scattering mechanism. Scattering is enhanced for higher vegetative moisture volumes and thicknesses and tends to depolarize the surface emission. At higher frequencies, this depolarization due to vegetation becomes more significant. Thus referring to Figures 3-16 and 3-17, vegetation model 3 (thickness, 200 cm; moisture volume, 0.5) exhibits the lowest surface emission polarization across this frequency range, while model 2 (thickness, 20 cm; moisture volume, 0.1) exhibits the highest. These vegetation models are characterized by high and low scattering, respectively, with models 1 and

4 exhibiting intermediate scattering properties. As can be seen in Figure 3-17, complete depolarization is reached at progressively lower frequencies as the scattering character of the vegetation increases as defined above. In fact, model 3 is unpolarized at all frequencies within this domain, while model 2 is totally polarized.

Using the vegetation surface emissivity models, brightness temperatures were evaluated for comparison to available field data. All ground truth measurements are given by Wang et al. (Wang et al., 1984). Figures 3-18 and 3-19 compare model results with measurements at 1.4 GHz for fully-grown corn and cut corn; Figure 3-21 shows the results at 5 GHz for dry corn. In general, the model results at these frequencies are quite good. This provides confidence to extend the model to higher frequencies. Calculations also indicate that scattering effects are negligible, especially at 1.4 GHz, since the brightness temperatures T_B are not sensitive to any change of l_ρ , l_z , or letting $\delta = 0$.

At higher frequencies, furthermore, the mean values, ϵ'_m and ϵ''_m decrease. Therefore the emissivities of the vegetative canopy become larger and resultant brightness temperatures T_B will be higher than those at low frequencies. As the observation angle increases, the random layer of scatterers exhibits more backscattering, which in turn darkens thermal emission. Therefore, at high frequencies, brightness temperature decreases monotonically as the observation angle increases. This behavior for higher frequencies is different from that at low frequencies (cf. Figures 3-18 through 3-19). At larger angles, warming effects due to atmospheric gas absorption in the atmospheric layer above the surface also become significant. The effect of multiple scattering also increases with increasing frequency. This effect significantly darkens the thermal emission. The appropriate choice of correlation length and their relative magnitudes also affects resultant brightness temperatures. As $l_\rho > l_z$, the laminar structure will cause more backscattering and significantly cool the thermal emission. For a fixed volumetric moisture fraction, increases in the magnitudes of l_ρ , l_z will also enhance backscattering and cool (i.e., decrease) the thermal emission. The larger the ratio l_z/l_ρ , the warmer the brightness temperature. Conversely, decreasing the correlation length gives warmer brightness temperatures, since there is less scattering. The modeled brightness temperature is also a func-

tion of the thickness and wetness of the vegetation. As the vegetation wetness increases, the brightness temperature will increase due to more thermal emission. For additional increases in wetness, saturation is reached. This characteristic behavior is enhanced for thicker vegetation. Once saturation is reached, brightness temperatures decrease since more scattering and attenuation cool the emission. This behavior is different from that at low frequencies, where brightness temperature monotonically increases.

3.4.4 Comparison with SMMR Data

3.4.4.1 Data Sample

Nimbus 7 Scanning Multichannel Microwave Radiometer (SMMR) data was used to provide a comparison to RADTRAN simulated sensor data for a selected subset of relevant surface models. The choice of surface types simulated was determined by the availability of suitable SMMR data sets. The SMMR observes ten channels (five dual-polarized frequencies: 6.6, 10.7, 18, 21, and 37 GHz) and scans conically with an angle of incidence on the surface of the earth of 50 degrees. The SMMR is described in Gloersen and Barath (1977) and NASA (1978). For selected Nimbus-7 passes, therefore, SMMR data were acquired from NSSDC (National Space Science Data Center) in the TCT (Calibrated Temperature Tape) format. The TCT format presents the data as brightness temperatures for actual SMMR footprints, with the FOV locations determined from the pierce points corresponding to the four antenna angles. The locational accuracy is good, usually within half a footprint (A. Chang, personal communication).

SMMR data at frequencies of 6.6, 10.6, 21, and 37 GHz were sampled for selected test areas from brightness temperature maps created from the SMMR data tapes. Both vertical and horizontal polarizations were used. Test areas were chosen to provide data on specific earth surface types including the calm ocean (Case 1), moderate vegetation (Case 2), and heavy vegetation (Case 3). All brightness temperatures were spatially smoothed to the resolution of the 6.6 GHz channels. Spatial resolution at this frequency is approximately 160 km. It was not necessary to insure that the observed field-of-view was

spatially uniform since it is our purpose to provide simulation models which are consistent with data averaged over typical sensor footprints.

3.4.4.2 Results of Data Comparison

Simulated SMMR brightness temperature data were calculated using the RADTRAN atmospheric transmission/brightness temperature model. Appropriate atmospheric profile input data for temperature and water vapor were obtained from a summer midlatitude model. This model also provided surface temperature data. SMMR data collected over the north central United States provides a surface background of moderate vegetation. Three subregions were selected and frequency dependent SMMR brightness temperature data were plotted. These data for each area are illustrated in Figure 3-21. Both vertical and horizontal polarizations are shown for each area and frequency. The data for area 1 shows a vertical brightness temperature near 255 K which is near constant with frequency. The horizontal brightness temperature for this case is about 25 K colder with the polarization difference decreasing with frequency. The data from areas 2 and 3 are qualitatively similar except that brightness temperatures are about 18 K higher. The corresponding model simulations are also presented in Figure 3-22 for comparison. The vegetation model was used to evaluate surface emissivity. Four vegetation types are shown corresponding to variations in the thickness of the vegetation and its moisture content. The least amount of scattering is given by the vegetation 2 model. This can be diagnosed from the large polarization differences at low frequencies which decreases with frequency. This result for a vegetation depth of 20 cm and vegetative moisture content of 0.1 is very similar to that for bare moist soil, e.g. the vegetation does little to mask the soil emission. The most scattering case is for vegetation 3 with a thickness of 200 cm and a moisture value of 0.5. In this model the polarized surface is completely masked by scattering in the vegetative layer and the polarization difference is very small. An examination of Figure 3-22 indicates that the domain of the model simulations brackets the actual SMMR data. That is on average the properties of the vegetation in the SMMR fields-of-view plotted in Figure 3-21 are between those of light and heavy vegetation. No attempt was made to tune the vegetation emission models to fit the data, however, it is clear that some intermediate degree of scattering would suffice. This could be achieved by adjusting the thickness or moisture content.

The second set of comparisons uses SMMR data from the southeastern United States. Again three subareas were chosen. Areas 1 and 2 were selected over the calm ocean. Calmness was judged from the magnitude of 37 GHz brightness temperature and precipitating areas were avoided by examining the 37 GHz polarization difference. The third area was chosen over a heavily vegetated region of central Florida. SMMR brightness temperatures for these areas are plotted as a function of frequency in Figure 3-22. It can be seen that the signatures of the first two areas and that of area three are quite distinct. Furthermore areas 1 and 2 are very similar. The simulated brightness temperatures for the oceanic cases are also shown in Figure 3-22. Here, both calm and rough sea models are illustrated. Comparison of these results with the data for areas 1 and 2 shows excellent agreement for the calm ocean simulation. Indeed, surface wind speeds for this time and area are reported to be low (i.e. less than 3 m/s). Simulation results for the area 3 are shown in the upper part of Figure 3-22. Again four possible models of the surface vegetation are illustrated which bracket the data. The small polarization difference of the data is consistent with the heavy vegetation model with high scattering, however, the magnitudes of the brightness temperatures for data and model are offset. This is most likely due to a difference between the actual and modeled surface temperatures.

3.4.5 Summary and Conclusions

A surface property modeling subpackage has been described which supplements the atmospheric transmission and radiance simulation capability provided by the AFGL RADTRAN computer algorithm. A variety of geophysical surface types are treated by the subpackage which calculated frequency and polarization dependent surface emissivities for use by RADTRAN in support of earth viewing microwave remote sensing system simulations. The theoretical basis for the emissivity calculation depends on surface type. Two distinct approaches are implemented: that based on wave theory for discrete scatterers and that based on radiative transfer theory for continuous random media. The former approach is used to model the ocean surface, various forms of sea ice, and snow over land, while the latter is used to treat soils and vegetation.

Calculations of polarized surface emissivity using these models illustrate the diverse frequency dependent signatures of the various surface

types. The angular dependence of surface emissivity is also illustrated. Using these surface emissivities as input to the RADTRAN atmospheric transmission submodels, simulated brightness temperature spectra have been computed for a variety of surface types. These simulations have been compared with Nimbus-7 SMMR data collected over selected areas. The comparisons illustrate that the simulation algorithm brightness temperature values based on the calculated surface emissivities provide a reasonable qualitative description of the spectral properties of the SMMR brightness temperatures. Further comparisons are necessary to validate the models especially for moist soil, snow, and sea ice.

In summary, the emissivity modeling subpackage significantly enhances the capability of the RADTRAN code to provide realistic brightness temperature simulations for sensors viewing geophysical surfaces.

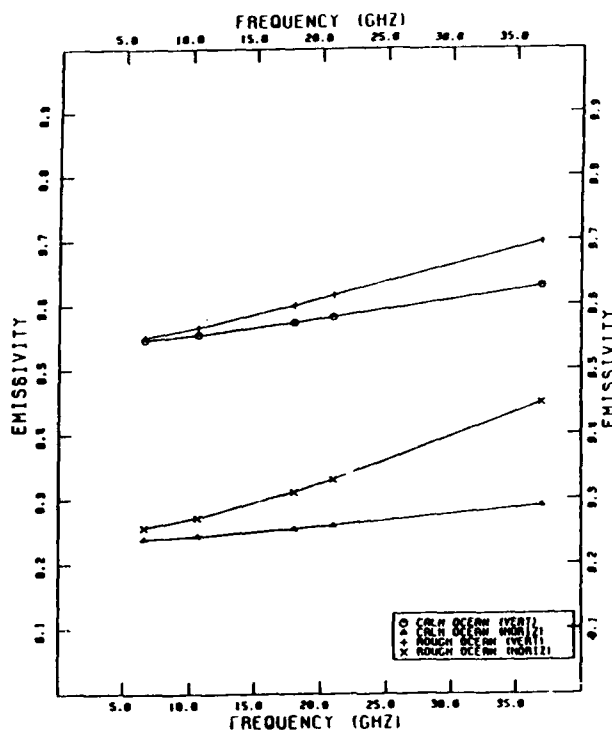


Figure 3-8. Frequency dependence of ocean surface emissivity for calm ($u < 7\text{ms}^{-1}$) and rough ($u \geq 7\text{ms}^{-1}$) ocean at a look angle of 54° .

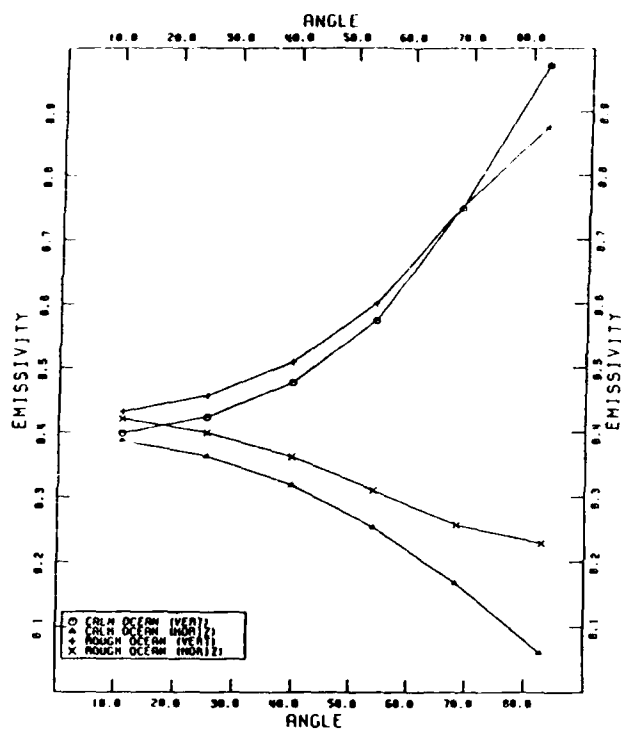


Figure 3-9. Look angle dependence of ocean surface emissivity for calm ($u < 7\text{ms}^{-1}$) and rough ($u \geq 7\text{ms}^{-1}$) ocean at a frequency of 18.0 GHz ($T_s = 273\text{K}$).

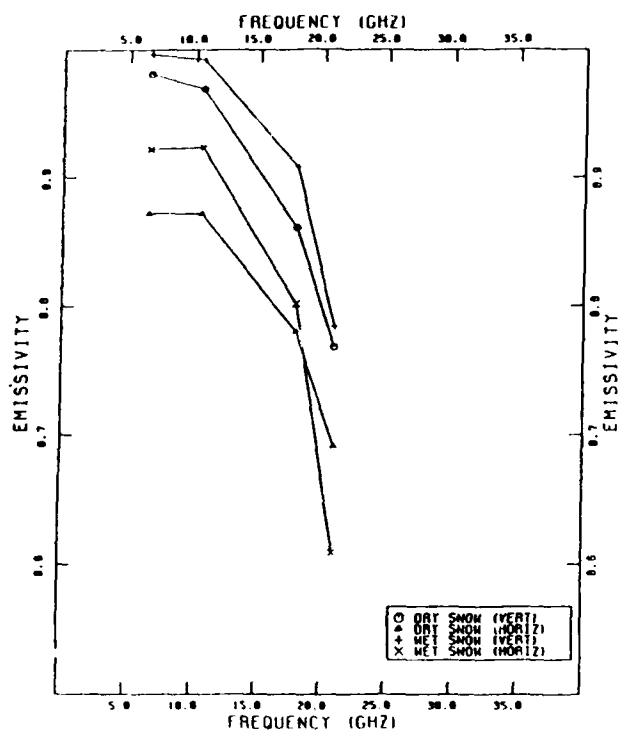


Figure 3-10. Frequency dependence of dry and wet snowpack emissivity at a look angle of 54° ($T_s = 273\text{K}$).

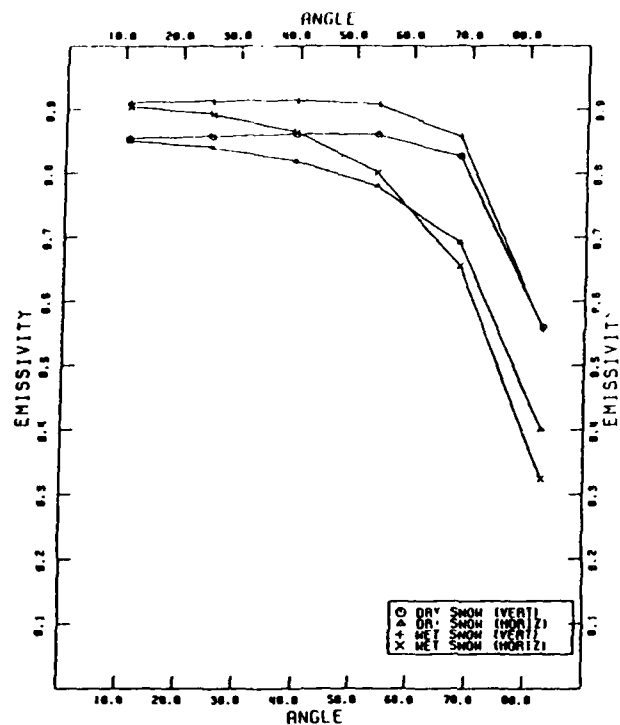


Figure 3-11. Look angle dependence of dry and wet snowpack emissivity at a frequency of 18.0 GHz ($T_s = 273.K$).

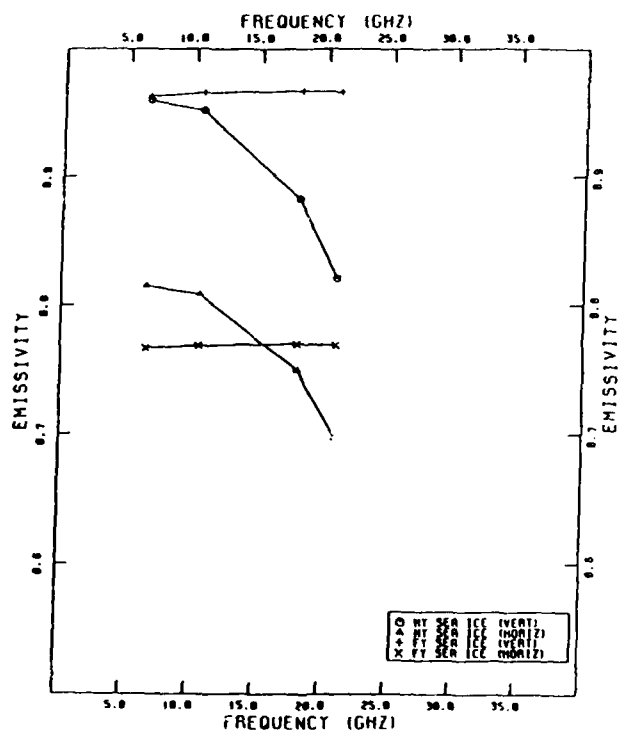


Figure 3-12. Frequency dependence of first year and multiyear sea ice emissivity at a look angle of 54° ($T_s = 273.K$).

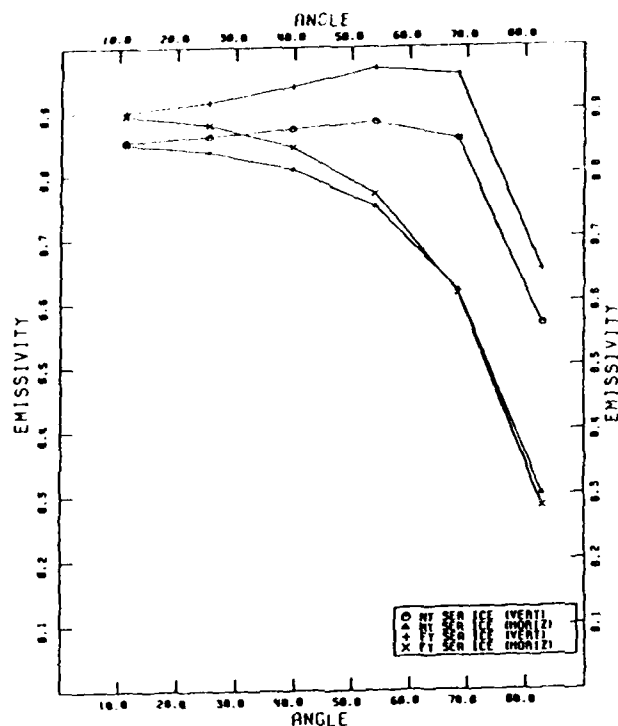


Figure 3-13. Look angle dependence of first year and multiyear sea ice emissivity at a frequency of 18.0 GHz ($T_s = 273.K$).

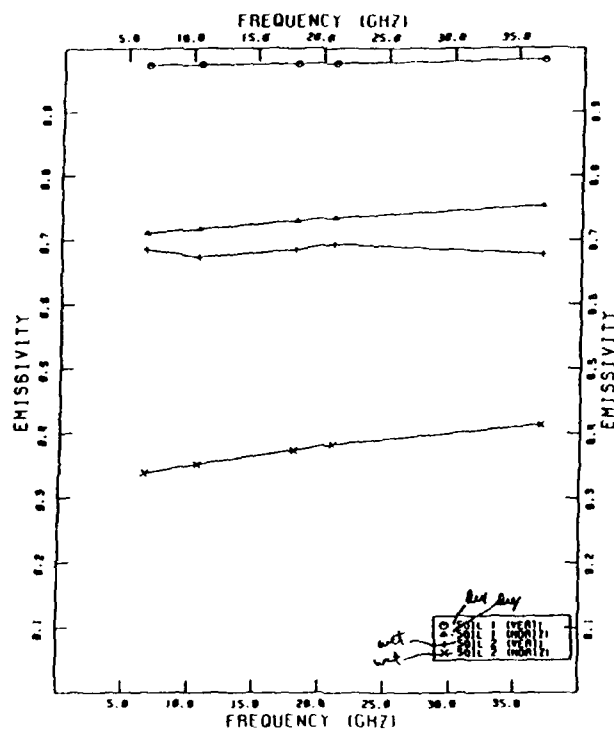


Figure 3-14. Frequency dependence of dry and wet soil emissivity at a look angle of 54°.

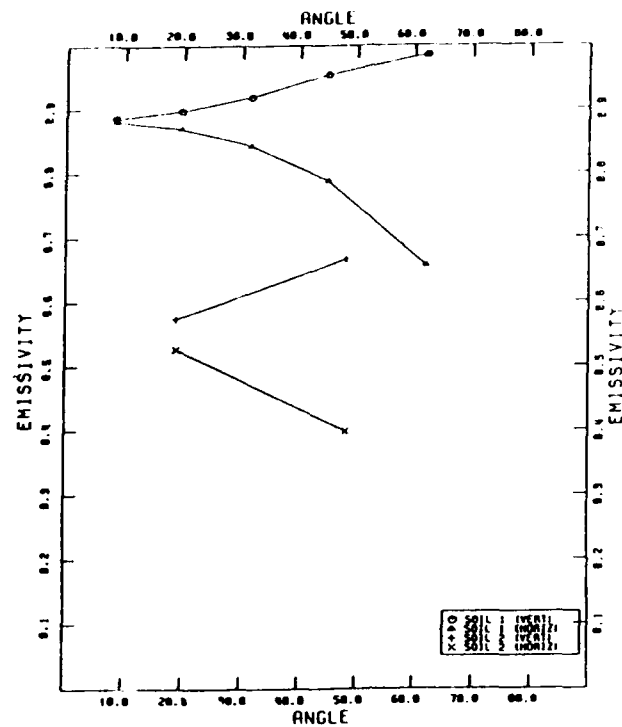


Figure 3-15. Look angle dependence of dry and wet soil emissivity at a frequency of 18.0 GHz.

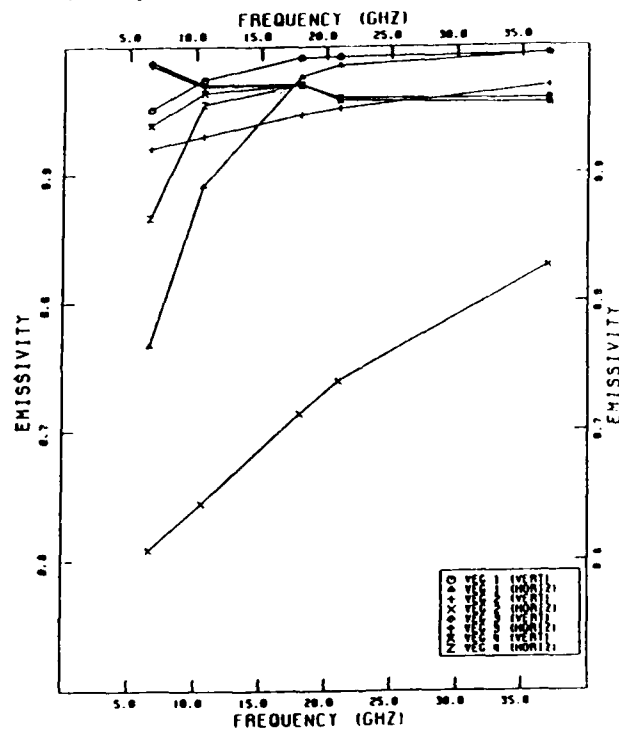


Figure 3-16. Frequency dependence of surface emissivity at a look angle of 54° in the presence of vegetation with various moisture contents and layer thicknesses.

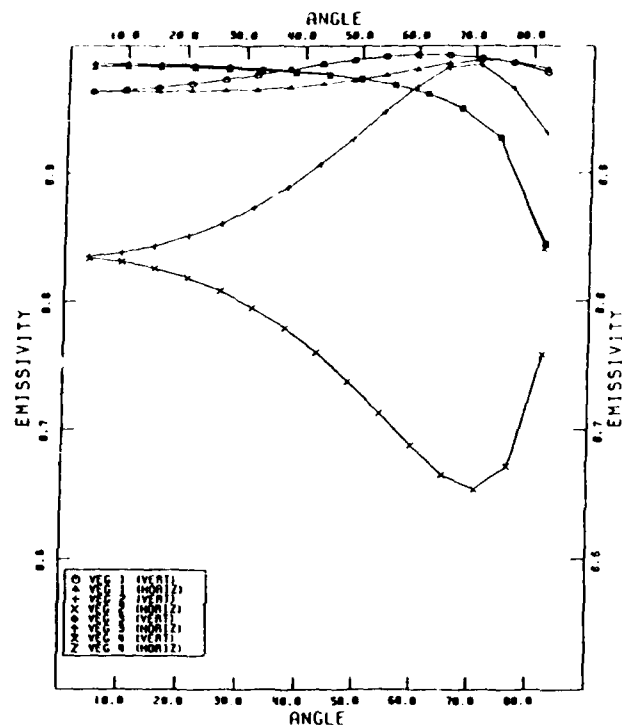


Figure 3-17. Look angle dependence of surface emissivity at a frequency of 18.0 GHz in the presence of vegetation with various moisture contents and layer thicknesses.

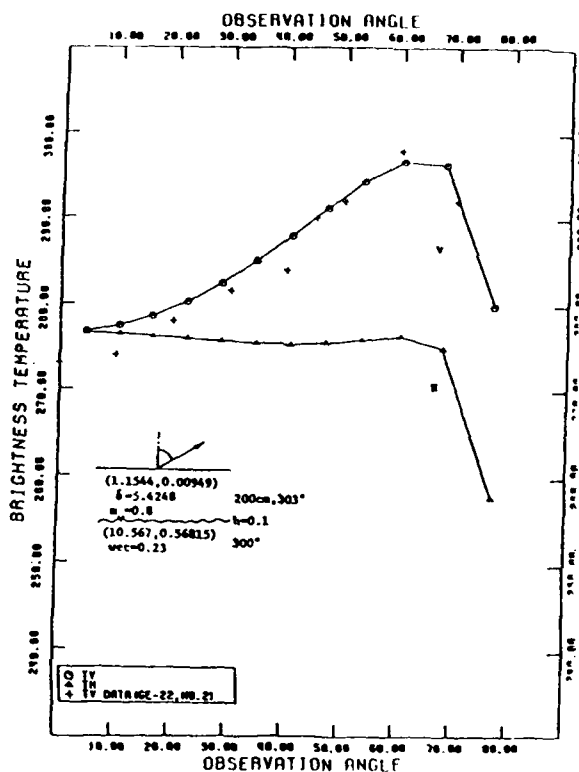


Figure 3-18. Brightness temperature as a function of angle for fully grown corn at a frequency of 1.4 GHz.

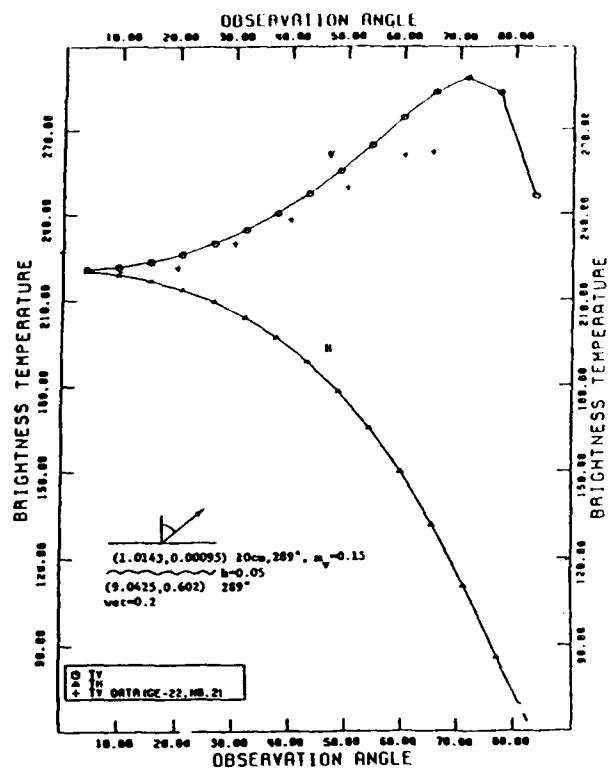


Figure 3-19. Brightness temperature as a function of angle for cut corn at a frequency of 1.4 GHz.

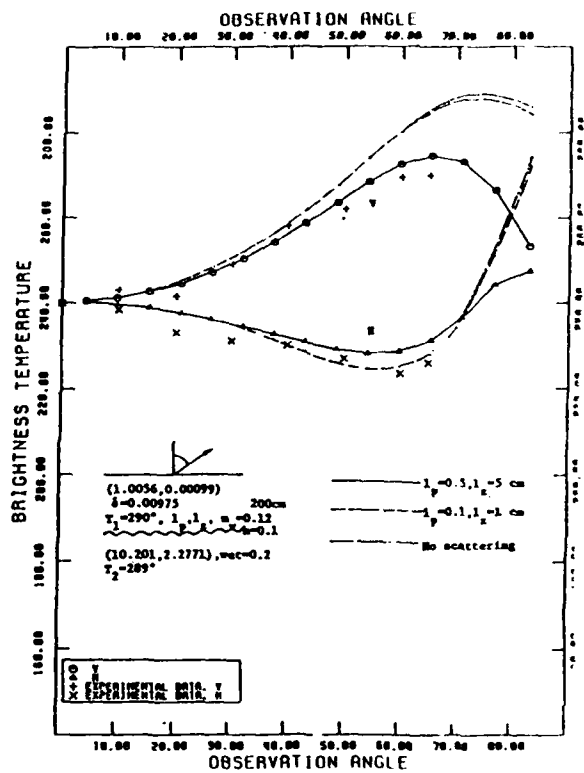


Figure 3-20. Brightness temperature as a function of angle for dry corn at a frequency of 5 GHz.

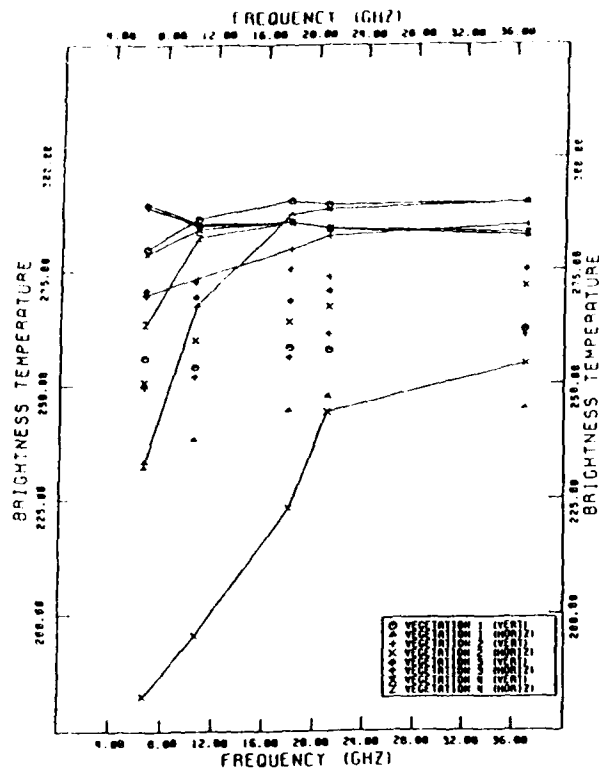


Figure 3-21. Comparison of SMMR brightness temperature data with RADTRAN model simulations for case 1 (ocean) and case 3 (heavy vegetation).

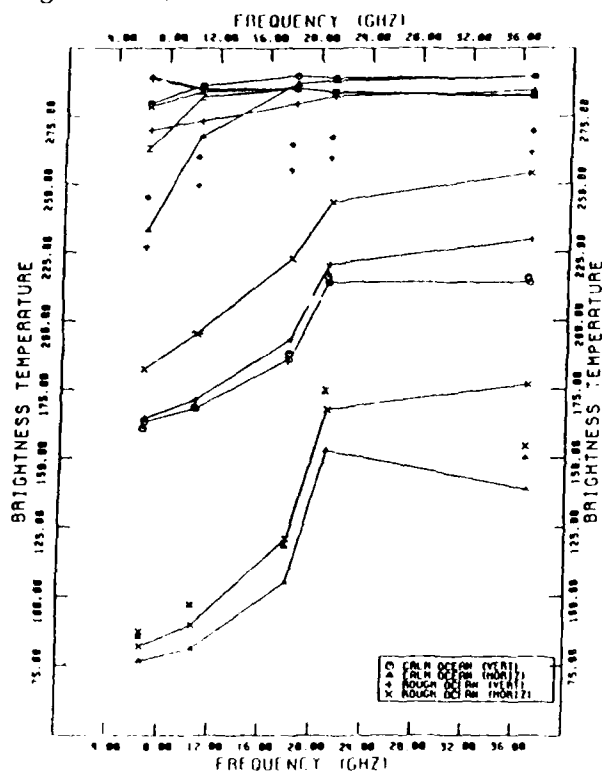


Figure 3-22. Comparison of SMMR brightness temperature data with RADTRAN model simulation for case 2 (moderate vegetation).

4. SSM/I FOOTPRINT CHARACTERIZATION USING OTHER DMSP SENSORS

4.1 Background

Observed brightness temperatures at window frequencies used in the retrieval of temperature and water vapor near the earth's surface are quite sensitive to the emissivities of the underlying surface. For example, the accuracy of water vapor retrievals near the surface is much better in general over the oceans than over land. This is due to the greater contrast to water vapor emission provided by the less emissive ocean surface background. For this reason, the inclusion of data from the SSM/I microwave imager at spatial resolutions of from 12.5 to 50 km can potentially improve the retrievals of temperature and moisture by helping to characterize the emissive properties of the fields-of-view for the SSM/T-1 microwave temperature and SSM/T-2 microwave moisture sounders. These sensors have spatial resolutions of about 180 and 50 km, respectively.

Likewise, retrievals are to be performed for a variety of meteorological parameters using data from the SSM/I sensor itself. Again, over spatial scales of up to 50 km there is considerable variation in the properties of both the atmosphere and the underlying surface. As an imager, the SSM/I seeks to measure both atmospheric and surface parameters. The size of the field-of-view would not be a problem if it was smaller than the characteristic scales of the phenomenon to be measured. Unfortunately this is not the case. Desired atmospheric parameters such as cloud liquid water, precipitation, and water vapor commonly vary on scales of as little as a few kilometers. Individual convective elements, for example, are typically a kilometer or so in horizontal extent. Likewise surface properties such as soil moisture, vegetation, snow cover, and sea ice vary on many scales. It must be understood that retrievals of these quantities based on simulations which assume uniform conditions within the SSM/I sensor field-of-view will be biased when observing non-uniform conditions. It is likely that nonuniform conditions will be common.

Other sources of data exist to help in characterizing the nonuniformity within the SSM/I field-of-view. Colocated with the SSM/I aboard the DMSP spacecraft, the Operational Linescan System (OLS) provides both visible and

infrared imagery at high spatial resolution. Currently there are no plans to use these data along with that from the microwave imager, although there are advantages from the perspectives of both meteorological analysis and SSM/I retrievals (Isaacs and Barnes, 1985). With much higher spatial resolution, the visible and infrared data from the OLS imagery can be used to provide guidelines on the uniformity of the SSM/I footprints. In those areas where the contributions from the atmosphere to microwave brightness temperature are small (i.e., nonprecipitating situations), daytime visible data should be able to provide guidelines on the uniformity of the surface observed within an SSM/I field-of-view. This capability will be degraded when clouds obscure portions of the field-of-view.

In cases of precipitation, the availability of visible and infrared data should considerably enhance the information content of the microwave retrieval by providing guidelines to ascertain the spatial uniformity of the rainfall. It is well known that a variety of methods exist to monitor rainfall which are based on the use of visible and infrared data alone (see Barrett and Martin, 1981). These methods differ from those used with microwave data since they are based on inferences derived from empirical relationships between the properties of the clouds accompanying the precipitation and the magnitude of the rainfall. The microwave methods result from actual interaction between the microwave radiation and precipitation and, but for the larger field-of-view, should potentially provide more quantitative rainfall rate retrievals. Nevertheless, the visible and infrared data has a spatial resolution advantage over the microwave data. Thus a combination of the two data sources (i.e., microwave and vis/IR) should be exploited.

Based on the considerations outlined above, we have undertaken to investigate the application of visible and infrared imagery from the OLS to aid in the characterization of the uniformity of the field-of-view of the microwave imager. This investigation has focused on two questions: (1) can high resolution visible and infrared imagery provide information on the uniformity of the microwave field-of-view either when observing the surface or atmospheric phenomenon such as precipitation?, and (2) can radiative transfer models of the surface emissivity and precipitation be used along with information obtained from the OLS imagery on the nonuniformity of the observed scene to simulate the averaging process which occurs within the microwave field-of-

view? In undertaking this task we have used the precipitation and surface emission modeling tools described in Sections 3.3 and 3.4 of this report, respectively.

4.2 Imagery Analysis of Microwave, Visible, and Infrared Data

In order to evaluate the feasibility of characterizing the uniformity of the microwave imager field-of-view using visible and infrared imagery and assess the resulting benefits for non-uniform scene modeling, the use of real data was desired. Since SSM/I data was not yet available, this study relied on archived Scanning Multichannel Microwave Radiometer (SMMR) data from the Nimbus-7 spacecraft. The SMMR data was used in conjunction with concurrent OLS data obtained in photographic positive imagery format. The data subset was previously used to investigate the capabilities of combining these sensors for the purpose of analyzing precipitation situations for tactical forecast situations.

The SMMR data used in the analysis as an analog for SSM/I imagery were obtained from the NASA Goddard Spaceflight Center in the CELL-ALL format. The CELL-ALL listings provide horizontal and vertical polarized brightness temperatures for each of the five SMMR frequencies. The spatial resolution varies with frequency from 150 km for the 6.6 GHz channel to 60 km for the highest frequency SMMR channel at 37 GHz. The 37 GHz data from the SSM/I, for example, should be available at a spatial resolution of about 25 km. It should be noted that the data used is considered to be preliminary, unverified data, i.e., final antenna corrections have not been applied, however, it should be more than adequate for these purposes.

Since digital data is not readily available from the operational DMSP OLS, digital analysis has been performed using simulated OLS data. The simulation process is based on transformation of Landsat MSS data obtained in digital format using a methodology described in Isaacs et al., (1986) and briefly reviewed below. The Landsat data has higher spatial and spectral resolution than the DMSP data. In order to simulate DMSP data, the Landsat data is spatially averaged to the desired resolution of DMSP LF or LS data. Since the four MSS spectral bands cover the wavelength domain between 0.4 and 1.1 μm spanned by the DMSP OLS visible data, the MSS data can also be

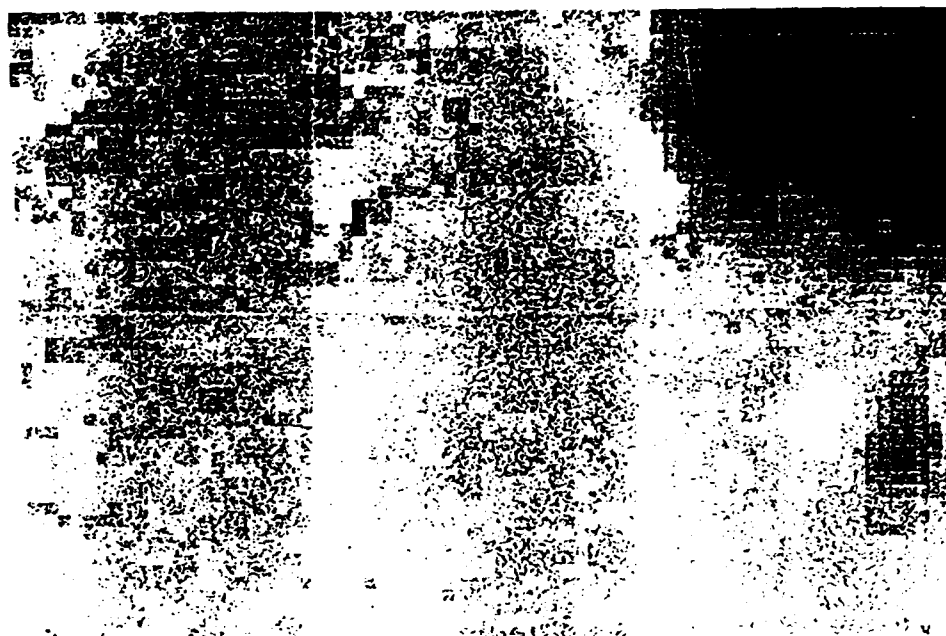
spectrally averaged to provide the DMSP bandpass to high accuracy. An example of this transformation is illustrated in Figure 4-1. Figure 4-1a is the original scene depicted from Landsat MSS bank 4 ($0.4-0.5 \mu\text{m}$). Figure 4-1b is the same scene transformed to simulate DMSP OLS LS data using all four MSS bands and spatially smoothed to provide the correct spatial resolution. The width of the original Landsat data was chosen to be 600 pixels. This corresponds to approximately 50 km or the width of the field-of-view for the 37 GHz channels of the SSM/I. As can be seen from the resolution element size for the simulated OLS LF data in Figure 4-1b, the microwave field-of-view corresponds to about one hundred visible fields-of-view.

To investigate the non-uniformity of the microwave footprint using visible and infrared data, we must assume that spectral signatures which are manifested in the visible and infrared data also result in microwave non-uniformity. This assumption should be quite reasonable. Essentially, for visible data we assume that those surface types which differ in visible reflectance also differ in microwave emissivity. The gross categories of soil, vegetation, water, snow, ice, etc. obey this simple rule. For the infrared data, the assumption is that types with differing infrared emissivity and/or emission temperature also differ in microwave emissivity. For surface features, this may not always be true. For example, bare soil and snow cover may have the same infrared signature (i.e. same surface temperature and emissivity), but have different microwave signatures due to microwave signatures of water bodies and land surfaces will differ due to varying thermal heat capacities, while their respective microwave emissivities are quite different due to distinctive permittivities. For atmospheric rather than surface sources of non-uniformity, such as precipitating cells, the correlation between visible/infrared and microwave signatures will insure that the adopted assumption is valid. It is understood that clear, non-precipitating areas will rarely be confused with cloudy, precipitating areas in visible or infrared data.

To characterize the non-uniformity of the microwave footprint, therefore, one must quantify the non-uniformity of essentially a problem in image processing. Classically, techniques to infer non-uniformity have been referred to as texture analysis methods. A number of approaches can be used for texture analysis including: (a) examination of the spatial power spectrum of an image



a



b

Figure 4-1. (a) High resolution Landsat visible data corresponding to the area of a single microwave FOV; (b) same area transformed to correspond to DMSP spatial and spectral resolution.

through Fourier decomposition, (b) edge enhancement, and (c) spatial coherence. We have chosen to investigate the spatial coherence approach since it has application in the determination of cloud properties from high resolution scanner data (Coakley and Bretherton, 1982; Coakley, 1983). This data analysis method might thus be applicable to the determination of both cloud and surface properties from OLS data.

Simply stated the approach quantifies what the eye observes when viewing an image or a portion thereof. The statistic evaluated is the local standard deviation (LSD) of radiance (or gray shade) values for the k th $n \times n$ subset of the field-of-view. The LSD is calculated as:

$$LSD_k = \left[\frac{1}{n^2} \sum_{i=1}^n \sum_{j=1}^n (I_{i,j} - \bar{I}_k)^2 \right]^{1/2} \quad (4.1)$$

where $I_{i,j}$ is the radiance of an individual pixel within the $n \times n$ subset array, and \bar{I}_k is the mean radiance of the k th subset given simply by:

$$\bar{I}_k = \frac{1}{n^2} \sum_{i=1}^n \sum_{j=1}^n I_{i,j} \quad (4.2)$$

To characterize a field-of-view consisting of a total of K individual $n \times n$ subsets (i.e. a total of $K \times n \times n$ pixels), the local standard deviation (LSD_k) and mean (\bar{I}_k) are calculated for each subset. A plot of LSD_k vs. \bar{I}_k will then give the following information:

- (a) If the field-of-view is uniform, all LSD_k values will be identically zero, and all \bar{I}_k values will be equal to the constant scene radiance.
- (b) If there are a few distinctive regions of constant radiance, LSD_k values will be generally small, and \bar{I}_k values will assume those of the discernable subregions.
- (c) For a general case, LSD values and \bar{I}_k values will be continuously variable.

For realistic geophysical fields-of-view, the idealized characterizations of the spatial coherence approach described above will be modified. In

general, we would expect to obtain clusters of points with the (LSD, \bar{I}) domain. Simply cluster analysis methods could then be used to identify significant clusters and define criteria for inclusion of individual pixels. Based on the cluster analysis, the microwave field-of-view can be divided into a small number of each FOV assignable to each category could be determined. Figure 4-2 illustrates an analogous application to the determination of fractional cloud cover using infrared scanner data from Coakley and Bretherton (1982). The local standard deviation vs mean radiance (expressed as brightness temperature) plot forms an arch. The cluster at the foot of the arch with highest temperature and lowest LSD can be identified with uniform sub-regions radiating at the surface temperature, while the other foot at lower temperatures can be identified with the top temperature. The other pixels with intermediate temperatures and nonzero local standard deviations in the arch are partially cloudy fields-of-view.

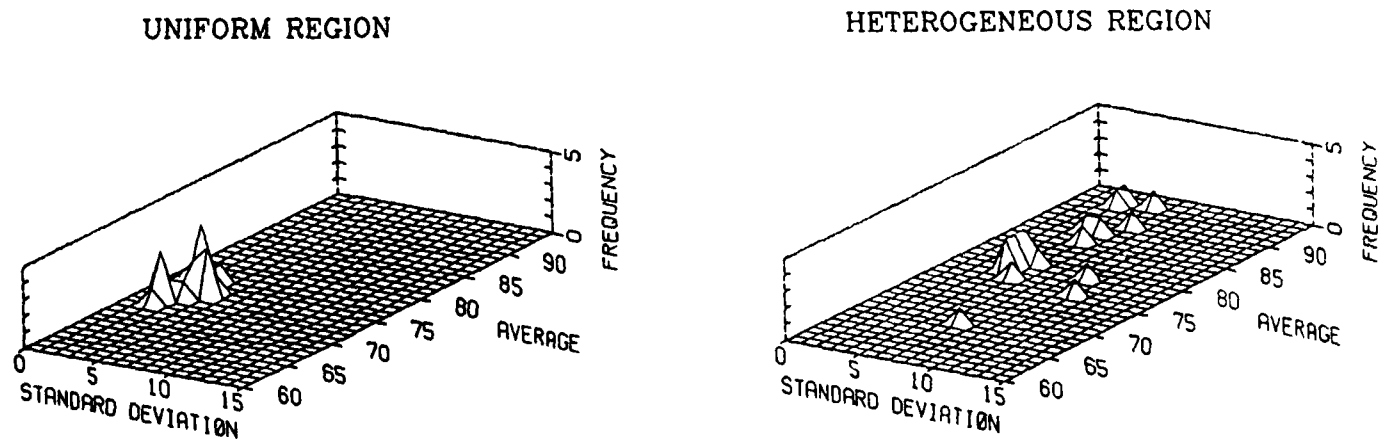


Fig. 4-2 Spatial Coherence Approach for Characterizing Field-of-View
Uniformity: (a) uniform FOV, (b) FOV with a few distinct regions.

4.3 Modeling Nonuniform Fields-of-View

The imagery analysis techniques described in the previous section provides a basis to obtain information on the non-uniformity of the microwave field-of-view based on the concurrent use of visible and infrared imagery data with higher spectral resolution. For example, based on the texture analysis arguments presented, visible data can be used, first to decide whether the microwave field-of-view is non-uniform, and, if so, to segment the FOV into a reasonable number of individual subregions which have similar characteristics. These subregions can then be assigned the emissive or radiative characteristics of known surface or atmospheric categories (i.e. rain, soil, water, snow, etc.), given that sufficient a priori data is available.

In this section we discuss how fields-of-view which have been determined to be non-uniform can be modeled. The information assumed available through the concurrent availability of high resolution visible and infrared data includes the fraction of the microwave field-of-view which belongs to a given type category, F_1 . It is assumed that we can model the emissive or radiative properties of these categories using one of the models described in Section 3 of this report.

If it is assumed that the i th microwave field of view at frequency j consists of $N_j \times M_j$ pixels, each with surface emissivity and temperature given by e_j and T_s , respectively, then the area averaged brightness temperature, T_j^i , will be given by:

$$T_j^i = \frac{\sum_{n=1}^{N_j} \sum_{m=1}^{M_j} e_j^{nm} T_s^{nm}}{(N_j M_j)} \quad (4.3)$$

For a completely uniform field-of-view, the surface emissivities for each pixel will be identical, i.e.:

$$e_j^{mn} = e_j \quad (4.4)$$

Thus, for a uniform surface temperature, T_s , the i th field-of-view brightness temperature will be:

$$T_j^i = e_j T_s \quad (4.5)$$

If the field-of-view is characterized as nonuniform, the pixel by pixel distribution given by equation (4.1) is too general for practical use. Instead, a few surface type categories such as those listed in Table 3-6 of Section 3.4 can be used. Assuming that L categories are utilized and that the fraction of the total pixels in each category is F_ℓ , equation (4.3) can be written as:

$$T_j^i = \sum_{\ell=1}^L F_\ell e_\ell T_s \quad (4.6)$$

where:

$$\sum_{\ell=1}^L F_\ell = 1 \quad (4.7)$$

Equation 4.6 assumes that the surface temperature is uniform throughout the i th field-of-view. If this is not the case and surface temperatures are deducible on a pixel by pixel basis, then (4.6) can be generalized to give:

$$T_j^i = \sum_{\ell=1}^L F_\ell e_\ell \sum_{m=1}^M \sum_{n=1}^N T_s^{mn} \quad (4.8)$$

where N_ℓ and M_ℓ are the number of pixels in each type category and:

$$\sum_{\ell=1}^L M_\ell N_\ell = M_j N_j \quad (4.9)$$

The desired characteristics of the microwave field-of-view uniformity can be obtained to some degree by exploiting the information content of high spatial resolution imager data. A field-of-view analysis technique based on these concepts is currently under investigation (see Isaacs et al., 1988c).

5. CONCLUSIONS AND RECOMMENDATIONS

5.1 Summary and Conclusions

This report has documented the following research accomplishments and milestones:

- Developed RADTRAN based models for the simulation of microwave and millimeter wave satellite sensor data applicable to the SSM/I, SSM/T-1, and SSM/T-2 (non scattering cases, i.e. no precipitation).
- Extended simulation capabilities to treat multiple scattering by clouds and precipitation including effects of polarization.
- Developed parameterization of precipitation extinction, scattering, and angular scattering properties (has been adopted for use in FASCODE!).
- Developed surface polarization/emissivity subpackage capable of treating ocean, sea ice, snow, soil wetness, and various types of vegetation.
- Evaluated accuracy of 183 GHz water vapor retrievals and SSM/I precipitation retrievals using statistical approach.
- Identified and evaluated the effect of cloud on millimeter wave moisture retrieval.
- Developed and tested unified, non-linear, physically based retrieval method to obtain temperature and water vapor profiles and surface temperature and emissivity from the SSM/T-1, SSM/T-2, and SSM/I instrument suite.
- Demonstrated improvement of above retrievals over purely statistical results for simulated data sets.
- Developed image processing based approaches to characterize microwave fields-of-view using high spatial resolution visible/infrared imager data (add-on task).

In this report we have focused on the retrieval of temperature and moisture using the DMSP microwave temperature sounder (SSM/T-1) and millimeter wave moisture sounder (SSM/T-2). It has been demonstrated that in cloud free conditions, the retrieval of moisture using a purely statistical approach is improved considerably when data from the temperature sounder is combined with that of the moisture sounder. The moisture sounder data appears to do little to improve the statistical retrieval of temperature. Furthermore, and significantly, it has been demonstrated that additional information can be obtained from the brightness temperature data of both instruments by adjusting the statistical retrieval first guess profiles of temperature and moisture using physically based considerations. The effect of this optional physical retrieval step is to increase the accuracy of inferred surface temperatures and moisture near the surface.

The physically based correction is in effect, a single iteration of a general physical inversion scheme such as that proposed by Chahine. The method used is to simulate sensor brightness temperatures based on the first guess profiles of temperature and moisture and guesses for the surface temperature and emissivity. The simulation is performed using a numerical scheme to integrate the equation of radiative transfer. The moisture and temperature profile first guesses are simply the statistical retrievals obtained from the operational statistically based algorithms for the SSM/T-1 and that proposed for the SSM/T-2. In our tests we used an analogous "D" matrix approach based on the work of Gaut et al. (1975) to provide this first step. Once the sensor data is simulated based on the first guesses, it is compared with the actual data. If the differences are less than an acceptable tolerance (determined by sensor and numerical noises), the statistical first guess is accepted as the final retrieval. If not, the difference between the simulated and actual brightness temperatures (i.e., the residual) is used to correct the first guess profiles. The scheme used to perform this adjustment is that discussed by Smith et al. (1985). The effect of this correction is to decrease the residual, and thus to make the retrieved profiles more consistent with the observed brightness temperatures. In order to increase the computational efficiency of the overall scheme, we have performed our calculations based on a single corrective step.

In order to optimally obtain these quantities, we believe that it is necessary to consider a unified retrieval scheme combining the moisture sounder data with that from the SSM/T-1 microwave temperature sounder, the SSM/I microwave imager, and the OLS. Although there are distinct advantages to this type of approach, it has not to our knowledge been proposed for operational use. On the contrary, it is planned that data from the three microwave mission sensors cited (i.e., SSM/T-1, SSM/T-2, SSM/I).

This report prescribes a unified retrieval approach tailored to the DMSP meteorological sensor suite. All of the available data is utilized in a multispectral sense. The existing operational statistical retrieval capability is exploited to provide parameter first guesses. First guess derived brightness temperature simulations are then compared with the original data and adjustments, based on sensor channel residuals, are made to the first guesses as required. A physically based simultaneous retrieval provides the appropriate parameter adjustments. Results of a retrieval simulation calculation illustrate the improvements possible to the statistical first guesses by utilizing all sensor data multispectrally and to the first guess parameters by employing the physical adjustment step. Recognizing the potential effect of clouds on the millimeter wave data, a method is outlined to introduce required first guess cloud information by image processing visible/infrared imager data. This procedure provides the opportunity to characterize the uniformity (both atmospheric and surface) of the relatively large microwave FOV. This provides potential insights into both cloud and surface type classification with implications for determining their emissivities.

While the retrieval approach outlined has been formulated as a stand alone system, its most important application may be to provide data for use in a numerical weather prediction model. In this context it is noted that modifications to the procedure outlined are desirable. Operationally, for example, it may be advantageous to obtain some first guess elements such as the temperature and moisture profiles from model predicted fields. Furthermore, in the context of a prediction model application, forecast error covariances may be used as constraints on the adjustment process (J. Eyre, personal communication). These changes are not inconsistent with the retrieval described and should in fact improve its effectiveness. Furthermore, the method provides estimates of each retrieval's accuracy.

5.2 Discussion of Future Work

The work accomplished during the tenure of this contract has provided a number of useful tools and opened a few new avenues of investigation. The testing of the unified retrieval algorithm has not been comprehensive in the sense that only a few climatological scenarios were investigated. This should be improved by undertaking more representative tests. An important consideration along these lines is the development and testing of the image processing based cloud analysis proposed to be applied to OLS data to provide cloud information in the unified retrieval. All of the testing reported here was done essentially for clear fields-of-view. Therefore this remains an important area for future research. This work should be coordinated with ongoing studies related to the operational nephanalysis in order to coordinate the type of cloud information desired and the techniques applied to obtain them. Ultimately, the nephanalysis should be a by-product of the unified retrieval scheme. The use of supporting data sets from the non-OLS sensors should improve the product currently available.

Many of the models developed during the course of this research such as the surface models, the precipitation optical properties models and the retrieval code could be usefully combined into an overall microwave simulation/retrieval code. We have not accomplished this during the course of this work, relying instead on segmenting the calculation and providing necessary input data to subsequent code elements. It would be useful to other users in the DoD modeling community to perform this code consolidation at some time in the future.

Finally, there are a number of subtleties related to the formulation of the retrieval code which could be improved. The unified approach would be enhanced if these were pursued in the future in a systematic way.

6. ACKNOWLEDGEMENTS

The principal investigator (R.G.I.) gratefully acknowledges the support and encouragement of V. J. Falcone of the Air Force Geophysics Laboratory (AFGL/LYS) throughout the tenure of this contract. Numerous others were helpful in fulfilling the objectives of this study and their help is appreciated: Dr. K. R. Hardy, AFGL; Dr. D. Pick, UKMO; Dr. R. N. Hoffman, AER; Dr. J. Eyre, UKMO; A. Stogryn, Aerojet; Dr. L. D. Kaplan, AER; Dr. R. Savage, Hughes; Dr. H. Schultz, AER; and Dr. A. Rosenberg, GE Astro.

7. REFERENCES

- Anthes, R. A., Y-H. Kuo, and J. R. Gyakum, 1983: Numerical simulations of a case of explosive marine cyclogenesis. Mon. Weather Rev., 111, 1174-1188.
- Barnes Engineering Company, 1978: Special sensor H-2 (SSH-2) total system spectral response. Air Force Contract F0470176-C-0058.
- Barrett, E. C., and D. W. Martin, 1981: The Use of Satellite Data in Rainfall Monitoring. Academic Press, New York, 340 pp.
- Chang, A., personal communication.
- Chahine, M. T., 1974: Remote sounding of cloudy atmospheres. I. The single cloud layer. J. Atmos. Sci., 31, 233-243.
- Chahine, M. T., 1982: Remote sensing of cloud parameters. J. Atmos. Sci., 39, 159-170.
- Choudhury, B. J., T. J. Schmugge, A. Chang, and R. W. Newton, 1979: Effect of surface roughness on the microwave emission from soils. J. Geophys. Res., 84(C9), 5699-5706.
- Clough, S. A., F. X. Kneizys, E. P. Shettle, and G. P. Anderson, 1986: Atmospheric radiance and transmittance: FASCOD2. Proceedings, Sixth Conference on Atmospheric Radiation, 141-144.
- Coakley, J. A., 1983: Properties of multilayered cloud systems from satellite imagery. J. Geophys. Res., 88(C15), 10818-10828.
- Coakley, J. A., and F. P. Bretherton, 1982: Cloud cover from high-resolution scanner data: Detecting and allowing for partially-filled fields of view. J. Geophys. Res., 87(C7), 4917-4932.
- Comiso, J. C., 1983: Sea ice effective microwave emissivities from satellite passive microwave and infrared observations. J. Geophys. Res., 88(C12), 7686-7704.

- Dave, J. V., 1972: Development of Programs for Computing the Characteristics of Ultraviolet Radiation. Technical Report Contract NAS 5-21680, NASA Goddard Spaceflight Center, Greenbelt, MD, 20771.
- Droppleman, J. D. 1970: Apparent microwave emissivity of sea foam. J. Geophys. Res., 75, 3, 696-698.
- Falcone, V. J., L. W. Abreu, and E. P. Shettle, 1979: Atmospheric Attenuation of Millimeter and Submillimeter Waves: Models and Computer Code. AFGL-TR-79-0253. ADA084485
- Falcone, V. J., L. W. Abreu, and E. P. Shettle, 1982: Atmospheric Attenuation in the 30 to 300 Ghz region using RADTRAN and MWTRAN. Proc. Soc. Phot. Opt. Instrum. Eng., 337, 62-66.
- Falcone, V. J. and R. G. Isaacs, 1987: The DMSP Microwave Suite. Proceedings, NOAA Conference on Passive Microwave Observing from Environmental Satellites. Williamsburg, VA.
- Fye, F. K., 1978: AFGWC automated cloud analysis model. AFGWC-TM-78-002, Air Force Global Weather Central, 97 pp.
- Gaut, N. E., E. C. Reifenshtein, and D. T. Chang, 1973: ERT Report.
- Gaut, N. E., M. G. Fowler, R. G. Isaacs, D. T. Chang and E. C. Reifenshtein, 1975: Study of microwave remote sensing of atmospheric parameters. Air Force Cambridge Research Laboratories. AFGL-TR-75-0007. ADA008042
- Halem, M. and J. Susskind, 1985: Findings of a Joint NOAA/NASA Sounder Comparisan: 1) AMTS vs. HIRS2, 2) Physical vs. Statistical Retrieval. Advances in Remote Sensing Retrieval Methods. A. Deepak Publishing, pp. 625-639.
- Huang, R., and K. N. Liou, 1983: J. Geophys. Res., 88.
- International Mathematical and Statistical Libraries, Inc. (IMSL), 1975: Library 3, Edition 5, Reference Manual (IMSL LIB3-005).
- Isaacs, R. G., G. Deblonde, R. D. Worsham, and M. Livshits, 1985a: Millimeter Wave Moisture Sounder Feasibility Study: The Effect of Cloud and Precipitation on Moisture Retrievals. AFGL-TR-85-0040. ADA162231
- Isaacs, R. G. and G. Deblonde, 1985b: Water Vapor Retrievals at 183 GHz: Land vs. Ocean and Clear vs. Cloudy. AFGL-TR-85-0095. ADA170033
- Isaacs, R. G., J. C. Barnes, L. D. Petro, and R. D. Worsham, 1986a: Inter-comparison of DMSP OLS, NOAA AVHRR, GOES VISSR, and Landsat MSS Imagery for Cloud Property Determination: Recommendations for Digital Data Analysis. AFGL-TR-86-0012. ADA169285

- Isaacs, R. G., R. N. Hoffman, and L. D. Kaplan, 1986b: "Satellite remote sensing of meteorological parameters for numerical weather prediction." Rev. of Geophys., 24, 4, 701-743.
- Isaacs, R. G., 1987: Review of 183 GHz Moisture Profile Retrieval Studies. AFGL-TR-87-0127. ADA182417
- Isaacs, R. G. and G. Deblonde, 1987a: Millimeter wave moisture sounding: The effect of cloud, Radio Science, 22, 3, 367-377.
- Isaacs, R. G., W. C. Wang, R. D. Worsham and S. Goldenberg, 1987b: Multiple scattering treatment for use in the LOWTRAN and FASCODE models. Appl. Opt., 26, 7, 1272-1281.
- Isaacs, R. G., 1988: A unified retrieval methodology for the DMSP meteorological sensors. Remote Sensing Retrieval Methods, Deepak Publishing (in press).
- Isaacs, R. G., R. D. Worsham, and M. Livshits, 1988a: Scattering properties of precipitation for the AFGL RADTRAN model. Appl. Opt. 27, 1, 14-16.
- Isaacs, R. G., Y. Q. Jin, R. D. Worsham, G. Deblonde, and V. J. Falcone, 1988b: The RADTRAN microwave surface emission models. (Submitted to IEEE Transactions on Geoscience and Remote Sensing.)
- Isaacs, R. G., A. M. Vogelmann, R. D. Worsham, J. C. Barnes, and Y. Q. Jin, 1988c: Application of High Spatial Resolution, Digital Visible/Infrared Imagery Data to the Characterization of Microwave Fields-of-View. Interim Report, AER Number P174TR. AFGL-TR-88-0029
- Ishimaru, A, and R. Cheung, 1980: Radio Science
- Jin, Y.-Q., and J. A. Kong, 1983: Appl. Opt., 22.
- Jin, Y.-Q., 1984: Electromagnetics, 2.
- Jin, Y. Q., and J. A. Kong, 1984: Strong fluctuation theory for electromagnetic wave scattering by a layer of random discrete scatterers. J. Appl. Phys., 1364-1369.
- Jin, Y. Q. and R. G. Isaacs, 1985: Thermal radiative transfer for inhomogeneous nonisothermal atmospheric precipitation and statistical retrieval of related parameters. Proceedings of the International Geoscience and Remote Sensing Symposium, 351-356.
- Jin, Y. Q. and Isaacs, R. G., 1987: Simulation and statistical retrieval for inhomogeneous, no isothermal atmospheric precipitation. J. Quart. Spectrosc. and Radiat. Transfer, 37, 5, 461-469.
- Kakar, R. K., 1983: Retrieval of clear sky moisture profiles using the 183 GHz water vapor line. J. Clim. and Appl. Meteorol., 22, 7, 1282-1289.

- Kakar, R. and B. H. Lambrigtsen, 1984: A statistical correlation method for the retrieval of atmospheric water vapor by microwave radiometry. J. Climate and Appl. Meteor., 23, 7, 1110-1114.
- Kaplan, L., R. Hoffman, R. Isaacs, R. Rosen, D. Salstein, and W.-C. Wang, 1983: Outlook for improved numerical weather prediction using satellite data with a special emphasis on the hydrological cycle. AFGL-TR-83-0305, 195 pp. ADA141233
- Liou, K. N., 1973: A numerical Experiment on Chandrasekhar's Discrete Ordinate Method for Radiative Transfer: Application to Cloudy and Hazy Atmospheres. J. Atmos. Sci., 31, 30, 1303-1326.
- Liou, K. N., P. Nipko, G. Aufderhaar, and H. Y. Yeh, 1980: Development of the Microwave Radiative Transfer Program for Cloudy Atmospheres: Application to DMSP SSM/T Channels. AFGL-TR-80-0051. ADA087434
- Lo, R. C., 1983: A comprehensive description of the mission sensor microwave imager (SSM/I) environmental parameter extraction algorithm. NRL Memorandum report 5199, Naval Research Laboratory, 52 pp. (NTIS # ADA1304052).
- Maddox, R. A., D. J. Perkey, and J. M. Fritsch, 1981: Evolution of upper tropospheric features during the development of a mesoscale convective complex. J. Atmos. Sci., 38, 1664-1674.
- NOAA, 1981: Polar Orbiter Data (TIROS-N and NOAA-6) Users Guide. NOAA-EDIS-NCC-SDSD, Washington, DC.
- Perkey, D. J., 1980: Impact of moisture on regional scale numerical model simulations. In Atmospheric Water Vapor, edited by A. Deepak, T. D. Wilkenson, and L. H. Ruhnke, Academic Press, New York, pp. 513-526.
- Phillips, N., J. Susskind, and L. McMillan, 1988: Results of a Joint NOAA/NASA Sounder Simulation Study. J. Atmos. Ocean. Tech., 5, 1, 44-83.
- Ray, P. S., 1972: Broadband complex refractive indices of ice and water. Appl. Opt., 11, 1836-1844.
- Reuter, D., and J. Susskind, 1986: Determination of Water Vapor Profiles and Total Ozone Burden from HIRS/MSU Sounding Data. Proceedings, Second Conference on Satellite Meteorology/Remote Sensing and Applications, 13-16 May 1986, Williamsburg, VA, pp 30-35.
- Rigone, J. L., and A. P. Stogryn, 1977: Data processing for the DMSP microwave radiometer system. In Proc. Eleventh International Symp. Remote Sensing of the Environment. Univ. of Michigan, Ann Arbor, MI, pp. 1599-1608.
- Rodgers, C. D., 1976: Retrieval of atmospheric temperature and composition from remote measurements of thermal radiation. Rev. Geophys. Space Phys., 14, 609-624.

- Rosenkranz, P. W., and D. M. Staelin, 1972: Microwave emissivity of ocean foam and its effect on nadiral radiometric measurements. J. Geophys. Res., 77, 33, 6528-6538.
- Rosenkranz, P. W., M. J. Komichak, and D. H. Staelin, 1982: A method for estimation of atmospheric water vapor profiles by microwave radiometry. J. Appl. Meteorol., 21, 1364-1370.
- Sadiku, M. N. O., 1985: Refractive index of snow at microwave frequencies. Appl. Opt., 24, 572-575.
- Savage, R. C., 1978: Radiative Properties of Hydrometeors at Microwave Frequencies. J. Appl. Meteorol., 21, 1364-1370.
- Schaerer, G. and T. T. Wilheit, 1979: A passive microwave technique for profiling of atmospheric water vapor. Radio Sci., 14, 371-375.
- Schmugge, T. J., J. H. Meneely, A. Rango, and R. Neff: Satellite microwave observations of soil moisture variations. Water Resources Bulletin, 13, 2, 265-281, 1977.
- Schmugge, T. J.: Remote sensing of soil moisture: Recent advances. IEEE Trans. Geoscience and Remote Sensing, GE-21, No. 3, p. 336-344, 1983.
- Schultz, F. L., 1982: Advanced microwave sounder unit implementation study. Final report. NASA JPL D-147, Jet Propulsion Laboratory, California Institute of Technology, Pasadena, CA.
- Simonett, D. S. (ed), 1983: Manual of remote sensing, Vol. 1. American Society of Photogrammetry, p. 158.
- Smith, B. T., J. M. Boyle, J. J. Dongarra, B. S. Garbow, Y. Ikebe, V. C. Klema, C. B. Moler, 1976: Matrix Eigensystem Routines - EISPACK Guide. Lecture Notes in Computer Science, Vol. 6, Springer-Verlag, Berlin.
- Smith, W. L., H. M. Woolf, C. M. Hayden, D. Q. Wark, and L. M. McMillan, 1979: The TIROS-N Operational Vertical Sounder. Bull. Am. Meteorol. Soc., 60, 1177-1187.
- Smith, W. L., H. M. Woolf, and A. J. Schreiner, 1985: Simultaneous Retrieval of Surface and Atmospheric Parameters, a physical and analytically direct approach. Advances in Remote Sensing Retrieval Methods, A. Deepak, H. E. Fleming, and M. T. Chahine (eds.) Deepak Publishing, pp. 221-232.
- Staelin, D. H., 1966: Measurements and interpretation of the microwave spectrum of the terrestrial atmosphere near 1-centimeter wavelength. J. Geophys. Res., 71, 2875-2881.
- Stamnes, K. and R. A. Swanson, 1981: A New Look at the Discrete Ordinate Method for Radiative Transfer Calculations in Anisotropically Scattering Atmospheres. J. Atmos. Sci., 38, 387-399.
- Stamnes, K. and P. Conklin, 1984: A New Multilayer Discrete Ordinate Approach to Radiative Transfer in Vertically Inhomogeneous Atmospheres. J. Quant. Spectrosc. Radiat. Transfer, 31, 3, 273-282.

Stogryn, A., personal communication

Susskind, J., J. Rosenfield, D. Reuter, and M. T. Chahine, 1984: Remote Sensing of Weather and Climate Parameters from HIRS/MSU on TIROS-N. J. Geophys. Res., 89, D3, 4677-4697.

Susskind, J., and D. Reuter, 1985: Intercomparison of Physical and Statistical Retrievals from Simulated HIRS2 and AMTS Data. Advances in Remote Sensing Retrieval Methods. A. Deepak Publishing, PP. 641-660.

Susskind, J., D. Reuter, and M. T. Chahine, 1985: Multispectral Remote Sensing Climate Parameters from HIRS/MSU Data. In Advances in Remote Sensing Retrieval Methods. A. Deepak Publishing. pp. 205-220.

Tsang, L., and J. A. Kong, 1976: Thermal microwave emission from half space random media, Radio Science, 11(7), 599-609.

Tsang, L., and J. A. Kong, 1977: J. Appl. Phys., 48.

Tsang, L., and R. W. Newton, 1982: Microwave emissions for soils with rough surfaces. J. Geophys. Res., 87(11), 9017-9024.

Ulaby, F. T., M. Razain, M. D. Dobson, 1983: Effects of vegetation cover on the microwave radiometric sensitivity to soil moisture. IEEE Trans. Geoscience and Remote Sensing, GE-21, 1, p. 51-61.

Ulaby, F. T., and R. P. Jedlicka, 1984: Microwave dielectric properties of plant materials, IEEE Transactions on Geoscience and Remote Sensing, GE-22(4), 406-414.

Vallese, F., and J. A. Kong, 1981: Correlation function studies for snow and ice. J. Appl. Physics, 52(8), 4921-4925, 1981.

Wang, J. R., and T. J. Schmugge, 1980: An empirical model for the complex dielectric permittivity of soils as a function of water content, IEEE Transactions on Geoscience and Remote Sensing, GE-18(4), 289-295.

Wang, J. R., J. L. King, T. T. Wilheit, G. Szejwack, L. H. Gesell, R. A. Nieman, D. S. Niver, B. M. Krupp, and J. A. Gagliano, 1983: Profiling atmospheric water vapor by microwave radiometry. J. Clim. and Appl. Meteorol., 22, 781-788.

Wang, J. R., J. C. Shine, S. L. Chuang, R. T. Shin, and M. Domrowski, 1984: Thermal microwave emission from vegetated fields: A comparison between theory and experiment. IEEE Trans. Geoscience and Remote Sensing, GE-22, 2, p. 143-149.

Warren, S. G., personal communication.

Waters, J. W., 1976: Absorption and emission by atmospheric gases. In Methods of Experimental Physics, 12, Part B, Academic Press, pp. 142-176.

Wilheit, T. T., A. T. C. Chang, M. S. V. Rao, 1977: J. Appl. Meteo., 16.

Wilheit, T. T., et al., 1982: J. Appli. Meteo.

WMO, 1978: Report of the JOC study conference on parameterization of extended cloudiness and radiation for climate models (Oxford, 27 September-4 October 1978). ICSU WMO GARP Climate Dynamics Sub-programme, 148 pp.

Appendix A - Papers Presented During the Course of This Work

- Isaacs, R. G. and G. Deblonde, 1985: Remote Sensing of Vertical Moisture Profiles and Cloud Properties from Simulated Millimeterwave Sounder and Microwave Imager Data. Digest Volume 1, International Geoscience and Remote Sensing Symposium. 7-9 October 1985, Amherst, MA, pp. 345-350.
- Jin, Y.-Q. and R. G. Isaacs, 1985: Thermal Radiative Transfer Theory for Inhomogeneous Nonisothermal Atmospheric Precipitation and Statistical Retrieval of Related Parameters. Digest Volume 1, International Geoscience and Remote Sensing Symposium. 7-9 October 1985, Amherst, MA, pp. 351-356.
- Isaacs, R. G. and G. Delonde, R. D. Worsham, and L. D. Kaplan, 1986: Remote Sensing of Hydrological Variables from the DMSP Microwave Mission Sensors. Proceedings, Second Conference on Satellite Meteorology/Remote Sensing and Applications, 13-16 May 1986, Williamsburg, VA, pp. 243-248.
- Isaacs, R. G., G. Deblonde, R. Worsham, and L. D. Kaplan, 1986: Remote Sensing of Atmospheric Water Vapor Profiles from Simulated Millimeter Wave Moisture Sounder Data. Digest, International Conference on Optical and Millimeter Wave Propagation and Scattering in the Atmosphere. 27-30 May, Florence, Italy, pp. 349-352.
- Isaacs, R. G., Y.-Q. Jin, G. Deblonde, R. D. Worsham, and L. D. Kaplan, 1986: Remote Sensing of Hydrological Variables from the DMSP Microwave Mission Sensors. Paper presented at the Beijing International Radiation Symposium, 26-30 August, Beijing, China.
- Isaacs, R. G. 1987: The DMSP microwave suite: Proceedings, NOAA Conference on Passive Microwave Observing from Environmental Satellites. Williamsburg, VA,, 1-4 June. NOAA TR-NESDIS-35 pp. 174-185.
- A Study of the Impact of 183 GHz Water Vapor Retrievals. Preprints, Eighth Conference on Numerical Weather Prediction, 22-26 February 1988, Baltimore, MD. American Meteorological Society, Boston, MA.

Appendix B - Publications Resulting From Work Completed During this effort.

Retrieval of Humidity Profiles from Satellite Radiance Measurements (1984)
Advances in Remote Sensing Retrieval Methods, Deepak Publishing, pp. 269-284 .

Satellite remote sensing of meteorological parameters for global numerical weather prediction (1986) Rev. of Geophys., 24, 4, 701-743.

Millimeter wave moisture sounding: The effect of cloud (1987) Radio Science, 22, 3, 367-377.

Simulation and statistical retrieval for inhomogeneous, nonisothermal atmospheric precipitation (1987) J. Quant. Spectrosc. and Radiat. Transfer, 37, 5, 461-469.

The RADTRAN microwave surface emission models (1987) submitted to IEEE Transactions on Geoscience and Remote Sensing.

Scattering properties of precipitation for the AFGL RADTRAN Model (1987) Applied Optics, 27, 1, 14-16.

A Unified Retrieval Methodology for the DMSP Meteorological Sensors (1988)
Remote Sensing Retrieval Methods, Deepak Publishing (in press).